2010

Ceramic dielectrics for high energy density capacity application

Sheng Chao

Department: Materials Science and Engineering

Recommended Citation

Chao, Sheng, "Ceramic dielectrics for high energy density capacity application" (2010). *Doctoral Dissertations*. 2066.
https://scholarsmine.mst.edu/doctoral_dissertations/2066

CERAMIC DIELECTRICS FOR HIGH ENERGY DENSITY CAPACITOR APPLICATION

by

SHENG CHAO

A DISSERTATION

Presented to the Faculty of the Graduate School of the

MISSOURI UNIVERSITY OF SCIENCE AND TECHNOLOGY

In Partial Fulfillment of the Requirements for the Degree

DOCTOR OF PHILOSOPHY

in

CERAMIC ENGINEERING

2010

Approved by

Fatih Dogan, Advisor

Wayne Huebner

Robert Schwartz

Matthew J. O'Keefe

James Drewniak

PUBLICATION DISSERTATION OPTION

The Introduction and Background sections of this dissertation provide information about the research background and a review of the literature. The body of this dissertation has been compiled in the format for publication in peer-reviewed journals. Five papers have been included in the following order. The first paper, "Effects of Sintering Temperature on the Microstructure and Dielectric Properties of Titanium Dioxide Ceramics," was submitted to *Journal of Materials Science*. The second paper, "Complex Impedance Study of Fine and Coarse Grain TiO_2 Ceramics," was submitted to *Journal of the American Ceramic Society*. The third paper, "Effects of Manganese Doping on the Dielectric Properties of Titanium Dioxide Ceramics," was submitted to *Journal of the American Ceramic Society*. The fourth paper, "Processing and Dielectric Properties of TiO_2 Thick Films for High Energy Density Capacitor Applications," was submitted to. *Inter. J. Appl. Ceram. Tech*. The fifth paper, "$BaTiO_3$-$SrTiO_3$ Layered Dielectrics for Energy Storage," was submitted to *Materials Letters*.

Another three parts related to the present research, but not included in the main body of this dissertation, are given in the appendix. The first part is about the investigation of donor doping on the dielectric properties of titanium dioxide ceramics. The second part is a portion of the paper entitled "Processing and Characterization of Hydrothermal $BaTiO_3$ Films on Stainless Steel," which was published in the *Proceeding of the Materials Science and Technology (MS&T) 2007* pp. 239-251. The third part is portion of the paper entitled "Synthesis and Sintering of Nano Structured High Purity Titanium Dioxide," which was published in *Ceramic Transactions, 2009 205 (Advances in Energy Materials)*, pp, 23-30.

ABSTRACT

The objective of this dissertation is to investigate the relationship between the processing parameters, microstructural development, defect chemistry and electrical properties of titanium oxide (TiO_2) dielectrics for high energy density capacitor applications. The effects of aliovalent dopants on the dielectric properties of TiO_2 ceramics were investigated, aiming to further improve the desired dielectric properties especially at elevated temperatures (up to 200^oC). Due to the segregation of acceptor type impurities in the starting powders, space charge polarization took place in TiO_2 ceramics with relative large grain size (≥500nm), leading to high dielectric loss and low energy storage efficiency. Increased ratio of grain boundary resistivity to bulk grain resistivity resulted in lower breakdown strength, as larger electric field was applied on the grain boundaries as they became the most resistive part. Donor doping (e.g., phosphorus or vanadium) can effectively remove the space charge layer due to charge neutralization of positively charged defects created by donors and negatively charged defects created by acceptors. Large area, crack free tapes were fabricated by tape-casting method using nano-sized (~40nm) TiO_2 powders. An energy density of ~14 J/cm^3 was demonstrated by testing of TiO_2 thick films (~100μm).

Studies on dielectric materials were extended to $BaTiO_3/SrTiO_3$ (BST) ceramics which were processed by lamination of $BaTiO_3$ and $SrTiO_3$ green tapes with a 2-2 spatial configuration. Preliminary results showed that BST ceramics are promising dielectrics for energy storage applications and offer compositional flexibility to achieve maximum energy density under specified electric fields.

ACKNOWLEDGMNTS

I am grateful to my advisor, Dr. Fatih Dogan, for his advice, guidance, inspiration and consistent encouragement through the course of my Ph. D. studies. I am fortunate to work in his research group, not only to learn academically, but also to grow professionally and get ready for developing a successful career in the future.

I would also like to thank my committee members: Dr. Wayne Huebner, Dr. Robert Schwartz, Dr. Matthew J. O'Keefe and Dr. James Drewniak. Thank you all for your valuable input and stimulation in spite of your busy schedule. Special thanks owned to Dr. Vladimir Petrovsky and Dr. Shi-Chang Zhang and Dr. Piotr Jasinski for their instruction of experimental techniques and valuable discussions.

There are many good friends to whom I am very grateful. I am honored to encounter so many wonderful persons here: Dr. Sumin Zhu, Dr. Qiang Fu, Xuhui Lu, Liying Zhang, Jiawanjun Shi, Navarre Bartz, Aligul Buyukaksoy, Ayhan Sarikaya, Anthony Seibert. There are so many names that I cannot list them all. Thanks to all my friends who enriched my life in Rolla.

I am deeply gratitude to my family: my wife, Chun, my parents, Yilin Chao and Zhenyi Zhang, and my grandpa, Gongde Zhang. Your unending support and love has been an inspiration when things have not gone well and you are always there for me.

Financial support through a MURI program sponsored by Office of Naval Research (Grant No. N000-14-05-1-0541) is also greatly appreciated.

TABLE OF CONTENTS

PAPER

APPENDICES

SECTION

LIST OF ILLUSTRATIONS

PAPER 1

PAPER 2

PAPER 3

PAPER 4

PAPER 5

LIST OF TABLES

PAPER 1

PAPER 3

PAPER 4

PAPER 5

SECTION

1. PURPOSE OF THIS DISSERTATION

The main objective of this Ph.D. research was to develop ceramic dielectrics for high energy density capacitor applications.

Titanium dioxide (TiO_2) was chosen as candidate dielectric material, due to its relatively high relative permittivity (>100) and high dielectric breakdown strength (BDS, BDS>500kV/cm for flat sample; BDS>1500kV/cm for dimpled sample). In addition, (Ba,Sr)TiO_3 (BST) ceramics were also investigated to explore their potential applications as energy storage capacitors.

The relationship between the processing parameters, microstructures and dielectric properties of TiO_2 ceramics was investigated. Samples prepared under certain processing conditions showed space charge polarization that greatly affected the dielectric properties and energy storage capability of TiO_2 ceramics. Characterization of the samples by various methods including impedance spectroscopy techniques was conducted to understand the origin of space charge polarization. TiO_2 thick films were fabricated by tape-casting method to study single layer capacitors. The effects of acceptor and donor doping were studied to optimize dielectric properties at elevated temperatures.

2. BACKGROUND

2.1 HIGH ENERGY DENSITY CAPACITOR

2.1.1 Energy Storage in Capacitors. A capacitor is a passive electronic component consisting of a pair of conductors separated by a dielectric. When a potential difference (voltage) exists between the conductors, an electric field is present in the dielectric. Energy is stored in the dielectric medium due to electric field. [1]. High energy density capacitor (HED capacitor) by its name is a class of capacitor that is capable of storing more energy in less volume and/or weight (normally > 1 J/cm^3). In this dissertation, energy density is specified as volumetric energy density in units of Joules per cubic centimeter (J/cm^3). Capacitance is a measure of the amount of electrical energy stored for a given electric potential.

$$C(V) = \frac{dQ}{dV} \qquad (1)$$

where:

C is the capacitance (F)

Q is the charge (C)

V is the voltage (V)

The capacitance of a parallel-plate capacitor constructed of two parallel plates with an area, A (m^2), separated by a distance, d (m), is equal to the following:

$$C = \varepsilon_r(E)\varepsilon_0 \frac{A}{d} \qquad (2)$$

where:

ε_r (E) is the field-dependent relative permittivity (dielectric constant) of the dielectric material (dimensionless)

ε_0 is the permittivity of free space (8.85×10^{-12} F/m)

The general form of the energy (W) stored in a capacitor can be expressed as:

$$W = \int V dQ \tag{3}$$

Substitute Eq. (1) into Eq. (3)

$$W = \int C(V) V dV \tag{4}$$

Substitute Eq. (2) into and Eq. (4)

$$W = \int A d \varepsilon_0 \varepsilon_r (E) E dE = A d \varepsilon_0 \int \varepsilon_r (E) E dE \tag{5}$$

where:

E is the electric field, E=V/d (V/m)

Thus, the volumetric energy density $J_{vol.}$, $J_{vol.}$=W/volume, (volume=A·d) is given by:

$$J_{vol.} = \varepsilon_0 \int \varepsilon_r (E) E dE \tag{6}$$

For linear dielectrics, with a field-independent dielectric constant then Eq. (6) can be simplified as:

$$J_{vol.} = \frac{1}{2} \varepsilon_0 \varepsilon_r E^2 \tag{7}$$

According to Eq. (6) and Eq. (7), it is evident that the ultimate energy density of dielectrics is predominantly determined by the permittivity of the material and the highest possible electric field that can be applied before dielectric breakdown occurs.

2.1.2 Dielectric Materials Used in HED Capacitors. HED capacitors are supposed to be suitable energy sources in pulse power systems for military applications such as electromagnetic launch system, higher power microwaves, electric armor, directed energy laser, etc. In addition, pulse power capacitors are also needed for other applications, such as defibrillators, X-Ray equipment, pulsed lighting, and power storage modules [2]. Since capacitors occupy more than 30% of the overall volume in conventional power converters and pulse power systems, development of capacitors with decreased volume, weight and cost is highly desired [3]. Reducing the volume of the capacitor becomes even more important when these devices are required to be on board of mobile platforms, such as aircraft, ships or vehicles.

In response to the ever increasing demand for fast response (discharge time in the range of sub-microsecond to millisecond) capacitor with decreased volume, significant progress has been made over the past decade through the development of dielectric materials. However, the development of HED capacitor so far is still evolutionary instead of revolutionary. The specific requirements for HED capacitor are diversified by its particular applications. Generally, HED capacitors should have the capability to discharge in a sub-microsecond to millisecond time frame, with operating voltage from several to hundreds of kilovolts, and with an energy density higher than 1 J/cm^3. For some special applications, an operating temperature up to 250^{o}C is also required. These requirements place stringent demands on the dielectric materials. A brief overview of various types of materials commonly used or promising for HED capacitor application is presented in this section.

2.1.2.1. Paper dielectrics. These types of HED capacitors are generally made of special high density “Kraft paper” which is impregnated in castor oil. Energy density up to 0.66 J/cm^3 is available for lifetimes of a few thousand charge/discharge cycles. These capacitors are suitable for “single-shot” and low repetition rate applications requiring high voltages (up to 100 kV), high peak current (up to 1 MA), high voltage reversal

(>20%), or some combinations of these factors [2]. The disadvantage of this type of capacitor is its low energy density and catastrophic failure mode.

2.1.2.2. Polymer dielectrics. For this type of HED capacitors, thin layer of metallic films are normally evaporated on the polymer (Polypropylene, Polyester, Polycarbonate, etc.) film as electrodes [4]. High breakdown strength up to 8 MV/cm and self-healing capability (due to evaporation of surrounding electrode materials (normally Aluminum) around the breakdown point, the capacitor can maintain its insulting properties can still be functional) are the two major advantages of this type HED capacitor. However, the application of polymer based HDE capacitor is limited by low operating (normally bellow 100^{o}C) temperature, low peak current and low tolerance to voltage reversal as well as high equivalent series resistance (ERS) [2]. Recently, one type of copolymer system consists of poly(vinylidene fluoride) P(VDF) and trifluoroethylene (TrFE) with high dielectric constant showed promising dielectric properties for HED capacitor application with high energy density of 17 J/cm^3 and discharging time below 1 μs [5].

2.1.2.3. Ceramic dielectrics. Ceramic capacitors especially $BaTiO_3$ based multi-layer ceramic capacitors (MLCCs) are widely used in various electronic devices due to their high capacitance density (high capacitance to volume ratio). However, ceramic dielectrics traditionally are not deemed as good choice for HED capacitors because of their low breakdown strength (generally on the level of several hundred kilovolts per centimeter or lower) and catastrophic failure mode. Since the commonly observed breakdown events in ceramic dielectrics are often triggered by microstructural defects, significantly improved breakdown strength (more then 1MV/cm) in ceramics has been demonstrated due to progress made in powder synthesis and MLCCs fabrication processes. Consequently, greatly enhanced energy density becomes achievable when higher electric fields can be safely applied. Energy density as high as 4 J/cm^3 was demonstrated using commercially available MLCCs with one X7R type material [6]. Further improvements in the the breakdown strength and reliability of ceramic dielectrics will make them promising candidates for high energy density capacitors in that the permittivity of ceramic dielectrics is generally high (K>1000 for ferroelectric ceramics) and variable in a wide range.

2.1.2.4. Polymer-ceramic composites. Due to the absence of readily available single phase material that can satisfy demanding requirements for HED capacitor applications, composite dielectrics are attracting more attention by taking the advantage of the best properties of each individual component. One promising approach is to combine the merit of high breakdown strength of polymers and high permittivity of ceramics into polymer-ceramic composites. Based on this approach, various polymer-ceramic composites have been investigated [7].

Among polymer-ceramic composites, the most widely adopted system consists of a polymer matrix and ceramic particle fillers (0-3 configuration, “0” means isolated ceramic filler particles, and “3” means a three dimensional connectivity of the polymer matrix). Ideally, the ceramic fillers help to increase the effective dielectric constant of the composite system without compromising the high breakdown strength and low loss of the polymers. However, the goal of high dielectric constant and high breakdown strength and low dielectric loss is not likely to be achieved all together [8]. In order to enhance the dielectric constant of the composite, high dielectric constant ceramic fillers such as barium titanate (BT), lead zirconate titanate (PZT), lead magnesium niobate-lead titanate (PMN-PT) are popular choices [9]. A large contrast (on the level of several hundred or higher) of dielectric constant between polymer matrix and ceramic filler gives rise to an inhomogeneous distribution of the electric field in the composites, which is believed to be the cause of the significantly reduced breakdown strength of such composite systems [10]. Moreover, with the increase of the particle size of the filler, the probability of electric field enhancement at the interface increases [8] lead to lower breakdown strength in such composites that has been often observed [11].

Another factor that limits the potential improvement in energy storage of polymer-ceramic composite is due to the fact that most of the increase in effective dielectric constant originates from an increase of the average field in polymer matrix with very little energy being stored in ceramic filler phase [12], as the electric field concentrates on the material with low dielectric constant. To address this problem, TiO_2 nanopowders with relatively low dielectric constant (K: ~100) was utilized instead of other commonly used fillers with very high dielectric constant. An improved energy density was observed in this nanocomposite in comparison with pure polymer, that was attributed to a homogeneous particle dispersion and comparable dielectric constant between polymer (PVDF based copolymer with K:~42) and filler (TiO_2 powder, K: ~47) [9]. Polymer-ceramic composites are attractive candidate materials for energy storage application, maximum energy density close to 10 J/cm^3 has been demonstrated in several systems so far [9, 13, 14].

2.1.2.5. Glass-ceramics. Glass-ceramics were investigated for their potential application in energy storage capacitors [15]. Since these materials are prepared by a melt-casting process followed by heat treatment to precipitate the ceramic crystalline phase from the glass matrix, they offer unique advantages for fabrication of pore-free materials with controlled crystalline size, towards achieving of improved breakdown strength. In addition, the crystalline phase may lead to higher dielectric constant in glass-ceramics exceeding the permittivity of the glass matrix.

In the study of Na_2O-PbO-Nb_2O_5-SiO_2 system [15], dielectric constant as high as 650-850 (1 kHz) with dielectric loss ~2% in the temperature range of 25^oC to 150^oC was obtained on samples treated in optimized processing conditions. One obstacle encountered in the study of glass-ceramic system is that due to interfacial polarization caused by vastly different dielectric constant (on the order of thousands) and conductivity (on the order of thousands) of glass phase and ceramic phase large hysteresis loss was observed especially under high fields (on the order of several kV/cm), resulting in fairly low energy density (Max. 0.9 J/cm^3) even though the dielectric constant (Max. 1000) and breakdown strength (Max. 800kV/cm) of the materials predicted much higher energy density (~3.5J.cm^3 if assuming ideal linear dielectric behavior) [16].

2.1.2.6. Glass dielectrics. Breakdown strength as high as ~12MV/cm was reported recently on a commercially available alkali-free glass, indicating a potential energy density as high as 35 J/cm^3 is possible [17]. Dielectric loss of this glass was low (~0.5%, 100 kHz, 25^oC-190^oC) with reasonably high dielectric constant (~ 6), which were attributed to alkali-free composition and highly polarizable barium ions, respectively [17]. Alkali-free composition and almost defect-free quality glass was believed to be the cause of the high breakdown strength [17].

2.2. DIELECTRIC PROPERTIES IMPORTANT FOR ENERGY STORAGE

2.2.1 Dielectric Breakdown Strength. Dielectric materials used for capacitor applications are exposed to a voltage gradient. Failure occurs when an electrical short circuit develops across the material. Such a failure is called dielectric breakdown, and the voltage gradient (V/m) sufficient to cause the short is termed the breakdown strength (BDS) of the material [18].

Unlike dielectric constant, which generally locates in a relatively narrow range for a specific material, the breakdown strength of the same material reported in different sources could vary dramatically. This is because that experimentally determined breakdown strength strongly depends on the microstructural features such as: porosity, pore size, grain size, grain boundary conditions (space charge, etc.), as well as external test conditions, such as: voltage ramp rate, frequency, sample geometric size (especially thickness), electrode materials, electrode shape, heat dissipation conditions etc. [19].

Dielectric breakdown is a complex process. For solid materials the following breakdown mechanisms are generally categorized: *Intrinsic Breakdown, Thermal Breakdown and Ionization Breakdown*. The so-called intrinsic breakdown means that the breakdown strength is an intrinsic property of dielectric materials, depending only on temperature while independent of specimen size and electrode material [20]. At high electric fields, electrons may be ejected from the electrode cathode) material or may even be generated from the valence band. The electrons are then accelerated under the influence of high field, knocking out other electrons and elevating them to the conduction band. These newly generated electrons are, in turn, accelerated by the field generating other electrons, finally resulting in an “avalanche” of electrons concentrated over a narrow area, causing a breakdown through a channel. Intrinsic breakdown takes place in a very short time (10^{-8}-10^{-7} second) and under very high fields (~1-10 MV/cm). Temperature has a pronounced effect on intrinsic breakdown as it influences the electron-phonon interactions. Intrinsic breakdown strength peaks around room temperature, when electron-phonon interaction becomes intense [21].

Thermal breakdown is more commonly observed than intrinsic breakdown, which refers to the breakdown caused by joule heating continuously generated within the dielectric specimen, due mainly to electrical conduction and polarization, which cannot be extracted fast enough by thermal conduction or convection [20]. The general equation governing the balance of heat generation rate and the heat loss rate is given by:

$$C_v \frac{dT}{dt} - div(K_t gradT) = \sigma F^2 \qquad (8)$$

where:

C_v is the specific heat per unit volume ($J/m^3 \cdot K$)

K_t is the thermal conductivity ($W/m \cdot K$)

σ is the electrical conductivity (S/m, in D.C. field, σ is the D.C. conductivity; in A.C. field, σ should include the conductivity due to dielectric polarization loss)

F is the electric field (V/m).

Obviously, conductivity and dielectric loss are two important factors that determine the heat generation and consequently thermal breakdown strength. Particularly in A.C. fields, keeping dielectric loss as low as possible is essential to increase thermal breakdown voltage.

Ionization breakdown in homogeneous dielectric solids occurs mainly through the mechanism of partial gas discharges, resulting from the presence of pores or cracks in ceramics. Ionization of gases within the pores takes place due to high local electric field concentrated around the pores [22]. This leads to local heating and generation of a cascade of ionized charges, which transmit the heat to the surrounding material. The resulting temperature gradients and development of thermal stresses can generate cracks, leading to further ionization and breakdown via a thermal process, similar to the above described thermal breakdown. Therefore, the presence of pores in dielectrics degrades the breakdown strength, particularly in humid environments and at elevated temperatures [21].

2.2.2. Dielectric Constant and Breakdown Strength. As briefly mentioned in the previous section, dielectric constant and breakdown strength are two key factors that determine the energy density of dielectrics. Ideally, dielectrics with both high dielectric constant and high breakdown strength would be the obvious choice for energy storage. Unfortunately, dielectrics which possess both high dielectric constant and high breakdown strength are not readily available. Although a fundamental relationship between dielectric constant and breakdown strength is still open to debate, many experimental results indicate that BDS decreases sharply with increasing dielectric constant [23]. Recently, a thermochemical model was proposed by McPherson et al. [23], suggesting that the breakdown strength (E_{bd}) decreases proportional to dielectric constant $(K)^{-1/2}$ over a wide range of dielectric materials [23]. The foundation of this model is that the local electric field (E_{loc}) is greatly enhanced in high k dielectrics according to Lorentz relation ($E_{loc}=[(2+K)/3]E$; E: externally applied electric field), tends to distort and weaken the bond strength of polar molecules in dielectrics such that the bond becomes very susceptible to breakage by standard Boltzmann process and/or hole capture [23]. As the bond breaks, a neutral trap is thought to be generated with a conductive percolation path being eventually developed leading to electrical and/or thermal breakdown of the dielectric. Figure 2.1 shows the predicted breakdown strength and best fitting for various dielectrics with dielectric constant ranging from 3.9 to 200.

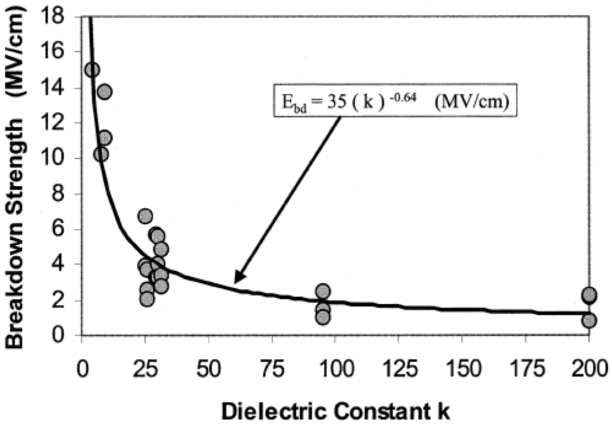

Figure 2.1. Thermochemical model prediction of the breakdown strength as a function of dielectric constant [25].

2.2.3. Conductivity and Dielectric Loss. Besides the dielectric constant and breakdown strength, another important material's property that deserves considerable attention is the electrical conductivity. Low conductivity ($<10^{-13}$ S/cm) can not guarantee high breakdown strength (>1 MV/cm) because microstructural defects may control the breakdown strength in some cases. However, dielectrics that have high breakdown strength are found to have relatively low conductivity. If leakage current reaches a critical level under high field stress thermal breakdown would be triggered due to the joule heating effects. Meanwhile, reducing the conductivity can also suppress the dielectric loss especially in low frequency ranges where the loss due to the d.c. conductivity is dominant.

Dielectric loss (loss tangent, tanδ) or so-called dissipation factor (DF) is also a crucial parameter for capacitor performance. Power dissipated as heat is defined by the following equation:

$$P = V^2 \omega C(DF) \qquad (9)$$

Where:

V is the voltage applied (V)

ω is the angular frequency (rad/s)

C is the capacitance (F)

DF is the dissipation factor (dimensionless).

Obviously, for HED capacitors which are expected to be used under high operating voltage, heat generation needs to be well controlled, especially when the capacitor operates at high frequencies (megahertz range). Temperature rise is detrimental to ceramic capacitors since the conductivity increases exponentially with the temperature, and increased conductivity, in turn, leads to even more heat generation. Therefore, thermal management is identified as one of the most important areas that are critical to the compact pulse power system [26]. Although the thermal management can be improved by design of more efficient heat sinks, reducing of the dielectric loss is certainly a more fundamental approach to address this issue.

2.2.4 Other Factors. Pulse power capacitors may be required to operate at elevated temperatures (up to 300°C) and over a broad range of frequencies. Linear dielectrics are less sensitive to temperature, electric field and frequency variations. For ferroelectrics, relaxors and antiferroelectrics, the temperature, electric field and frequency dependence of their dielectric properties have to be taken into consideration. A more detailed discussion of these issues is addressed in the following sections.

2.3. ADVANTAGES AND DISADVANTAGES OF VARIOUS CERAMIC DIELECTRICS FOR ENERGY STORAGE

One of the most intriguing advantages of ceramic dielectrics for HED capacitor applications lies in the fact that the dielectric constant of ceramics vary in a broad range (typically from ~4 for SiO_2 to over 10,000 for relaxor type ferroelectrics). In addition, high temperature stability is another unique attribute of ceramic dielectrics. Therefore, in terms of applications in elevated temperatures, ceramic dielectric is almost the only possible choice.

Dielectric properties of polycrystalline ceramics can be tailored and optimized by composition, impurities and/or dopants, processing parameters (e.g., sintering temperature, time, atmosphere, heating/cooling rate and resultant microstructural features (e.g., porosity, grain size, grain boundary conditions). Graphic representations of the retractable energy density upon discharge are depicted in Figure 2.2 for linear, ferroelectric and antiferroelectric materials.

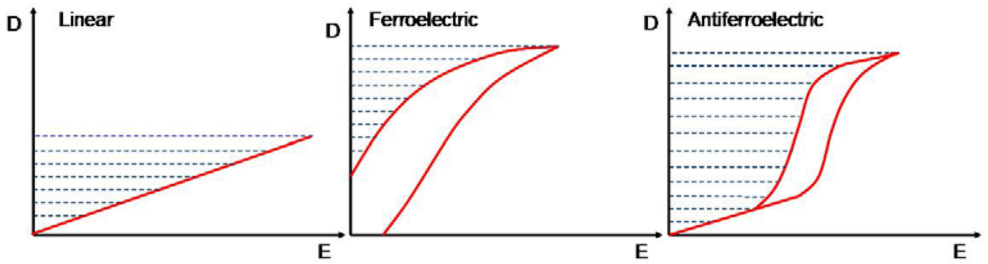

Figure 2.2. Schematic drawing of dielectric displacement (D) and electric field (E) relationship of linear dielectrics, ferroelectrics and antiferroelectrics (energy density upon discharge is represented by the shaded area).

2.3.1. Linear Dielectrics. For linear dielectrics, the dielectric displacement (D), polarization (P) and dielectric constant (K) have a linear relation with the electric field (E). When k >>1, the difference between dielectric displacement and polarization will be very small, hence, polarization is used hereafter instead of dielectric displacement.

Dielectric constant of linear dielectrics is relatively low (generally <100) since the polarization mechanisms are limited to electronic and ionic polarization. Both electronic polarization and ionic polarization are effective up to very high frequencies, ~10^{15} Hz and 10^{12}-10^{13} Hz, respectively [18]. Hence, the dielectric constant of linear dielectrics is stable in a wide frequency range if possible contributions of dipolar and space charge polarization are not in effect.

As discussed in the previous section, an inverse relationship between breakdown strength and dielectric constant exists in general. In fact, linear dielectrics with relatively low dielectric constant exhibit a breakdown strength that is in the high end for ceramics. Breakdown strength of common linear dielectrics is listed in Table 2.1. It shows that breakdown strengths on the magnitude of several megavolts per centimeter can be reached even for bulk ceramics. Estimating of potential energy density of ideal linear dielectrics (no dielectric loss) is straightforward, as long as data on dielectric constant and breakdown strength are known. Figure 2.3 illustrates the achievable energy density of ideal linear dielectrics as a function of dielectric constant and breakdown strength, which demonstrates that for linear dielectrics, breakdown strength is the dominant factor that determines the energy density.

Table 2.1. Breakdown strength of some common linear ceramic dielectrics.

Materials	Form	Thickness (μm)	BDS (MV/cm)	Reference
SiO_2	Film (Reactive pulse magnetron sputtering)	≈1	9 (d.c.)	[27]
Al_2O_3	Film (Reactive pulse magnetron sputtering)	≈1	4 (d.c.)	[27]
Al_2O_3	Single crystal (dimpled geometry)	≈30	6 (d.c.)	[28]
MgO	Ceramic (1-3μm grain size, dimpled geometry)	≈1250	2.4 (pulse d.c.)	[29]
ZrO_2	Doped with 10% Yttria	---	2 (d.c.)	[30]
TiO_2	Ceramic (0.27μm grain size, dimpled geometry)	≈40	1.8	[31]
Mica	---	≈1.3	9 (a.c.)	[32]

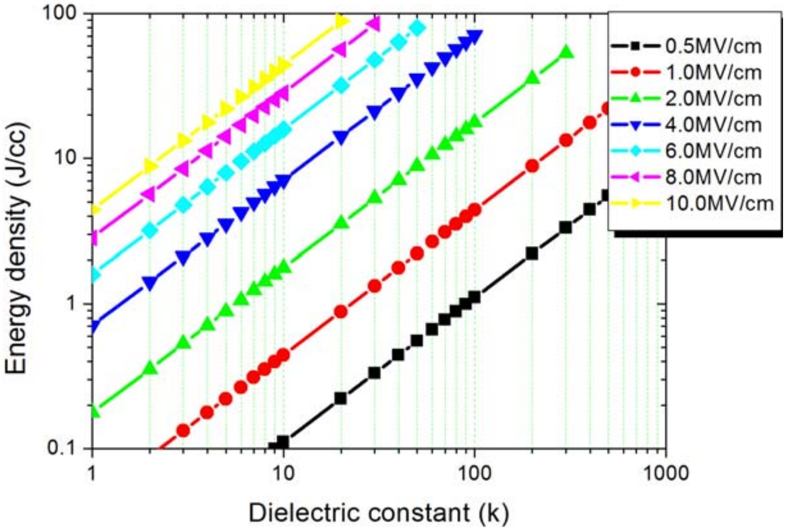

Figure 2.3. Energy density as a function of dielectric constant and breakdown strength for ideal linear dielectrics.

Conductivity ($\sigma<10^{-13}$ S/cm) and dielectric loss ($\tan\delta< 1\%$) are generally low for linear dielectrics. Since conduction loss is normally the predominant loss mechanism for linear dielectrics, good insulation property often guarantees a low dielectric loss. In addition, linear dielectrics are more stable to changes in voltage, temperature and frequency as compared to non-linear dielectrics, that is critical if the capacitor is required to operate under variable conditions. Table 2.2 gives a general specification of NPO/COG (linear), X7R (ferroelectric) and Y5V (relaxor) type capacitors according to the Electronic Industries Alliance (EIA) standards. It can be seen that the temperature coefficient and dissipation factor of COG/NOP class capacitor are much lower than X7R and Y5V type of capacitors in the designated operating temperature range. Recently, H. Ogihara et al., [33] reported the performance of one type of commercially available COG/NOP class capacitor in the temperature range from 20°C to 320°C. Despite of its relative low dielectric constant (34 @10 kHz), the ultimate energy density of this type of capacitor is reasonably good (>3 J/cm^3). More importantly this type of capacitor demonstrated excellent high temperature performance as shown in Figure 2.4.

Table 2.2. General specifications for COG/NOP, X7R and Y5V types of capacitors.

	COG/NPO	X7R	Y5V
Operating temp. Range	-55^{o}C – +125^{o}C	-55^{o}C – +125^{o}C	-30^{o}C – +85^{o}C
Temperature coefficient (ΔC Max.)	0±30 ppm/^{o}C	±15%	+22% – -82%
Dissipation factor @ 1k Hz	0.1% Max. 0.04% Typical	2.5% Max. 1.6% Typical	7% Max.

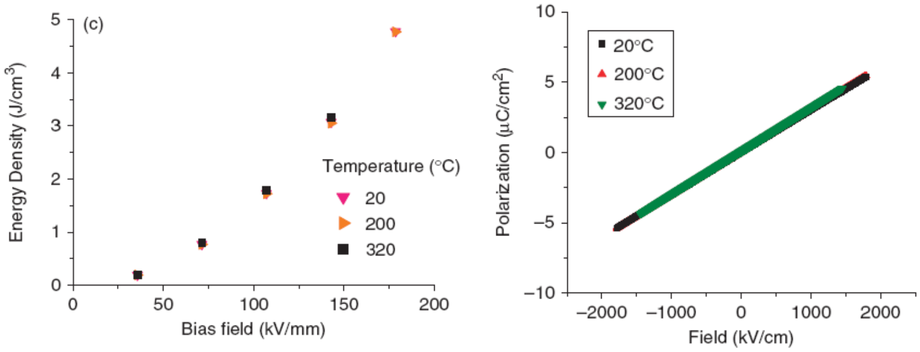

Figure 2.4. Energy density versus bias field (left) and polarization versus electric field (right) of COG/NPO commercial capacitor measured at various temperatures [33].

2.3.2. Ferroelectrics. Ferroelectrics represent a class of materials that possess a spontaneous electric polarization and the direction of the polarization can be reversed by an external electric field. Since the discovery of ferroelectricity in barium titanate ($BaTiO_3$) in the 1940's, this class of materials have dominated capacitor technology, as up to two orders of magnitude higher dielectric constant than previously known could be achieved [21]. Obviously, the most interesting characteristic of ferroelectrics for HED capacitor application lies in the high dielectric constant. A survey of the recently reported $BaTiO_3$ ceramics and $BaTiO_3$ based ceramics showed that dielectric constant generally ranges from 2000 to 6000 (at 1kHz and room temperature), depending on the powder characteristics, dopants and sintering conditions of the material [34-39]. However, high dielectric constant measured under low electric field could be misleading for a fair estimation of energy density, because under high electric field the dielectric constant could drop to only a small fraction of the value obtained under low field, due to polarization saturation. Figure 2.5 illustrates the relationship between the dielectric constant and bias field of a X7R type ferroelectric. It can be seen that under the field of 300 kV/cm, the dielectric constant drops to about one fourth of the original value. As shown in Figure 2.2, the slope of D-E relation decreases as the electric field increases, since available dipoles that can align with the electric field become less and less when most of the dipoles become oriented along the direction of the electric field. Consequently, characteristics of field dependence of dielectric constant are critical for ferroelectrics, and it would be desired to shift the occurrence of saturation polarization to higher electrical fields (on the level of hundreds of or even thousands of kV/cm).

Traditionally, due to low breakdown strength (<500 kV/cm), $BaTiO_3$ based ferroelectrics are not considered as suitable candidate dielectrics for HED capacitor applications [33]. However, attributed to the progresses made in the powder synthesis and ceramic processing technology, MLCCs with thin dielectric layers (state of the art technology now can produce MLCCs with dielectric layer less than 1μm [40]) demonstrate significantly enhanced breakdown strength (Table 2.3). As a result, it is necessary to revisit the energy storage capability of ferroelectric based MLCCs fabricated by advanced recent technologies.

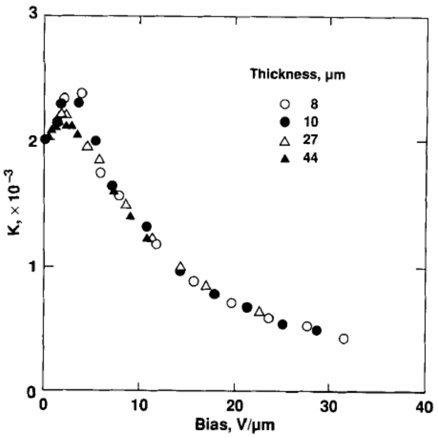

Figure 2.5. Dielectric constant (k) as a function of bias field for a X7R type capacitor with various dielectric layer thicknesses [5].

Table 2.3. Breakdown strength of $BaTiO_3$ based X7R type dielectrics.

Base materials	Powder synthesis route	Grain size (μm)	Dielectric layer thickness (μm)	Breakdown strength (MV/cm)	References
$BaTiO_3$	Oxalate process	0.1-0.25	4.8	1.1	[40]
$BaTiO_3$	---	---	6.0	1.4	[41]
$BaTiO_3$	---	<1	20	0.9	[6]

The breakdown strength of MLCCs decreases substantially with the increase of the dielectric layer thickness as shown in Figure 2.6. This phenomenon could be explained by the well-known "weak link" theory, because the thicker the dielectric layer, the higher the possibility of the presence of defects that can intrigue the breakdown phenomenon. Therefore, if high breakdown strength can only be achieved in capacitors with very thin dielectric layer, the operating voltage of the capacitor would be limited.

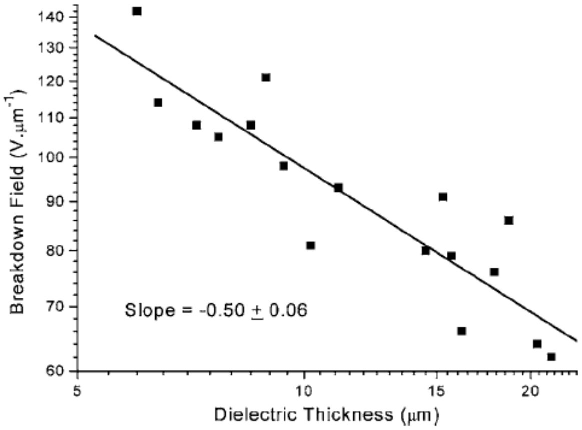

Figure 2.6. Breakdown field vs. dielectric layer thickness for $BaTiO_3$-Ni MLCCs (each data point represents ≥ 25 individual chips) [41].

The dielectric loss of ferroelectrics is higher than that of linear dielectrics (Table 2.2). Besides the conduction loss, hysteresis loss is critical for ferroelectrics. Thus, controlling the shape of the hysteresis loops becomes important for ferroelectrics in order to achieve high energy densities. In general, a "narrow" hysteresis loop is preferred to a "broad" one; as a "broad" hysteresis loops means that much of the stored energy would dissipate as heat that is not retractable upon discharge. The shape of the hysteresis loop can be modified by compositional design, for instance changing the barium to strontium ratio in $Ba_xSr_{1-x}TiO_3$ system as demonstrated in Figure 2.7.

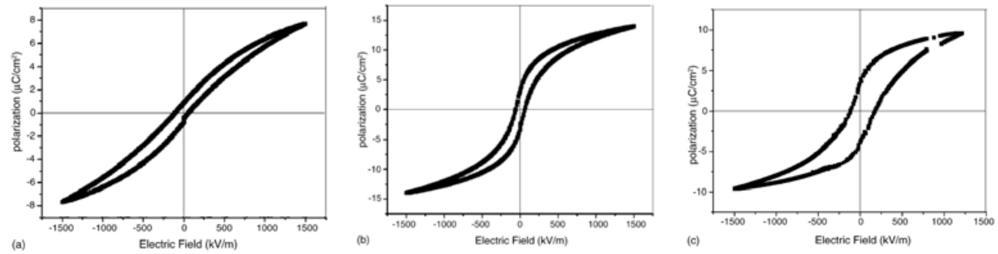

Figure 2.7. Hysteresis loop of $Ba_xSr_{1-x}TiO_3$ ceramics measured at room temperature and 1 kHz: (a) x=0.65, (b) x=0.8, (c) x=0.9 [42].

Pure $BaTiO_3$ goes through a series of phase transitions as temperature changes, in particular accompanied with the phase transition from ferroelectric tetragonal phase to cubic paraelectric phase around 120^oC (T_c, Curie temperature), there is a sharp peak of dielectric constant. Thus, for practical applications $BaTiO_3$ is modified by various dopants of so called “depressor” and “shifter”, in order to broaden and shift the Curie peak close to designated operating temperature range.

Not only is the dielectric constant of ferroelectrics greatly affected by temperature, but also the dielectric loss and conductivity. At elevated temperatures due to increased loss and conductivity, degradation of the energy storage capability is expected. In H.Ogihara and coworkers’ research [33], this phenomenon was exemplified by a commercial X7R type capacitor as shown in Figure 2.8.

2.3.3. Relaxor Ferroelectrics. Relaxors are a class of ferroelectrics that have a diffuse, frequency dependent permittivity maximum, with a relaxation spectrum much broader than Debye-type [43]. Relaxors generally have higher dielectric constant (>10,000) than normal ferroelectrics, and its dielectric constant maximum at T_C is also broader than normal ferroelectrics. Another interesting characteristic of this class of dielectrics is that densification of material can be achieved at lower temperatures [21]. Consequently, relaxors have the advantage to be used in MLCCs with base metal electrodes [44].

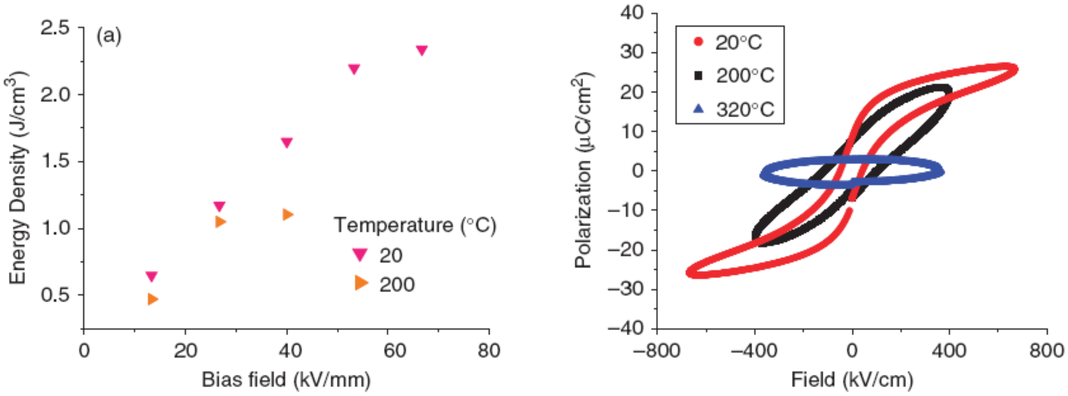

Figure 2.8. Energy density vs. bias field (left) and polarization vs. electric field (right) of a commercial capacitor X7R with base metal electrode [33].

The dielectric properties of relaxors are quite sensitive to temperature, electric field and frequency variations. For example, the dielectric response of $0.925Pb(Mg_{1/3}Nb_{2/3})O_3$-$0.03Pb(Zn_{1/3}Nb_{2/3})O_3$-$0.045PbTiO_3$ (PMN-PZN-PT) ceramics was investigated under various external electric field [45]. Under high d.c. bias both the dielectric constant and dielectric loss were suppressed and frequency dispersion reduced as shown in Figure 2.9. Fine grained relaxor type $[(Pb_{0.63}Ba_{0.37})(Zr_{0.7}Ti_{0.3})O_3]$ $+10mol\%Pb(Mg_{1/3}Nb_{2/3})O_3$ (PBZT) ceramics showed less capacitance variation and lower dissipation factor under d.c. bias voltage and oscillation voltage in comparison with $BaTiO_3$-based ferroelectrics as shown in Figure 2.10. [46]. The breakdown strength reported in this study is 590 kV/cm for a capacitor with a dielectric layer thickness of 3.2μm. Unfortunately, the energy density was not reported in this paper for PBZT-based ceramics. Since there is a lack of the breakdown strength data for many of the relaxor type dielectrics, further investigations would be needed to explore the energy storage capability of relaxor type dielectrics.

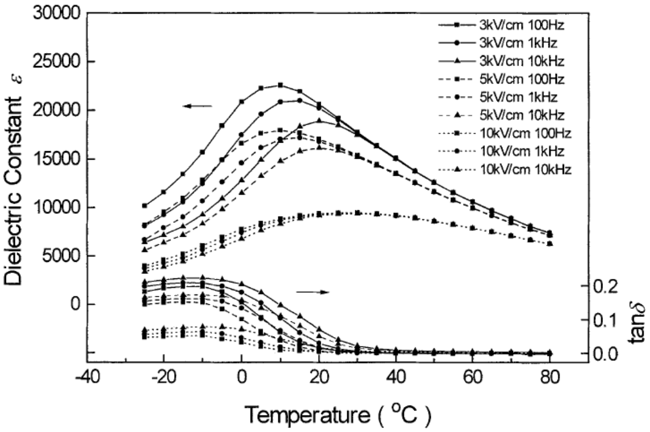

Figure 2.9. Dielectric constant and loss factor of PMN-PZN-PT ceramics as a function of temperature for various d.c. bias conditions [45].

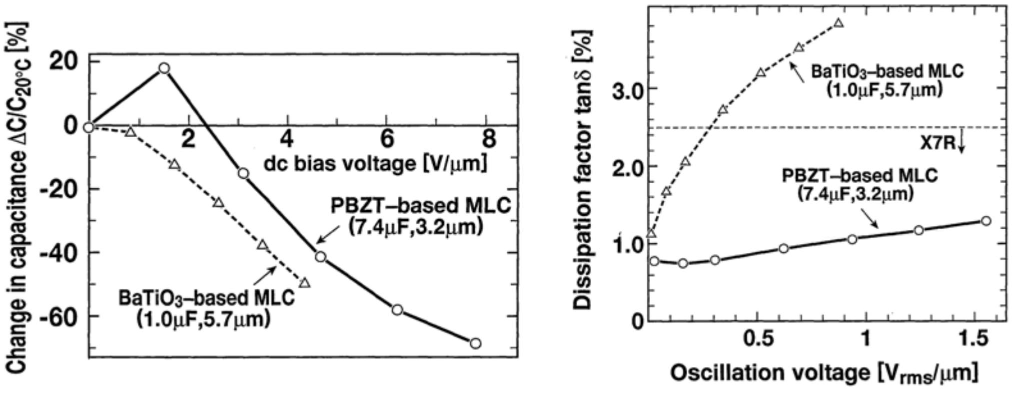

(a) (b)

Figure 2.10. (a) D.C. bias voltage dependence of capacitance of PBZT-based and $BaTiO_3$ based capacitor. (b) Oscillation voltage dependence of dissipation factor of PBZT and $BaTiO_3$ capacitors [46].

2.3.4. Antiferroelectrics. Antiferroelectrics attracted increasing attention for their potential application in energy storage because of their unique capability of undergoing a field induced transition from antiferroelectric (AF) to ferroelectric (FE) state. The potential energy gain of antiferroelectrics in comparison with ferroelectrics could be substantial due to the absence of remanent polarization and if the onset of the AF to FE transition can be probably delayed (move to the field on the level of hundreds of kV/cm or higher) [47].

Recently, it was demonstrated that Sr-doped $PbZrO_3$ [48] and La-doped $PbZrO_3$ [49] have improved energy storage capability close to 15 J/cm^3 at room temperature. However, it was also reported that energy density dropped to about half of the room temperature value at 210°C and the energy storage efficiency also reduced to about 70% at 210°C, indicating that the energy storage performance of antiferroelectrics at elevated temperature require further improvement [48].

Fatigue and degradation are two major problems associated with long-term application of ferroelectrics and antiferroelectrics for energy storage. Degradation of the ferroelectric properties was observed upon repeated reversals of polarization which appeared in the form of a decrease in remanent polarization or saturated polarization [50].

Many possible causes of fatigue were proposed such as gradual reorientation of domains to a more stable configuration [51], domain wall pinning due to injection of charge carriers [52], space charge buildup within the dielectric/electrode interface [53], and microcracking caused by a large change in strain during switching [54]. Degradation of resistance of ferroelectric ceramics was also observed and it was mainly attributed to the migration of oxygen vacancies under electric field [55].

Since ferroelectrics and antiferroelectrics also show piezoelectric properties, the possibility of crack formation subject to an alternating electric field is another challenge for their application in capacitor applications. In particular, for antiferroelectrics, there is a large longitudinal strain caused by field-induced phase transition [56].

2.4. DIELECTRIC PROPERTIES OF TITANIUM DIOXIDE (TiO_2)

Due to its balanced dielectric properties (medium dielectric constant and high breakdown strength), TiO_2 is considered as a potential candidate material for HED capacitor application. The dielectric constant of single crystal rutile TiO_2 at room temperature in the c-direction is 170 and 86 in the a-direction [57]. For randomly orientated polycrystalline rutile TiO_2, dielectric constant is ~100 [58]. Although the dielectric constant of TiO_2 is at the high end for linear dielectrics, it is significantly lower than that of ferroelectrics. Therefore, the improvement of energy density will mainly depend on the improvement of the breakdown strength along with lowering electrical conductivity and dielectric loss.

The breakdown strength of TiO_2 ceramics was found to have a strong dependence on grain size. Breakdown strength of TiO_2 ceramics with a grain size ranging from 0.27μm to 11μm were studied by Ye [59]. Between the breakdown strength and grain size, a relation $BDS \propto G^{-1/2}$ (G is grain size) was found. The highest breakdown strength reported in this study is ~1700 kV/cm, indicating a potential energy density ~15J/cm^3 (assuming the dielectric constant ~110 and no dielectric loss). Improved breakdown strength of TiO_2 with fine grain size was attributed to higher grain boundary density (thus possibly more electron blocking centers), however, no detailed discussion was provided [59].

The dielectric properties of TiO_2 are quite sensitive to processing conditions such as oxygen partial and temperature [58], as well as the presence of intrinsic impurities and/or dopants [60, 61]. Hence, optimization of ceramic processing conditions and introducing of appropriate type and amount of dopants are two important strategies to achieve the desired electrical properties of TiO_2 ceramics required for the HED capacitor applications. TiO_2 is prone to be reduced if sintered in low oxygen partial pressure or even in air atmosphere, leading to n-type properties with electrons as predominant charge carriers. This process can be expressed by the following defect reactions:

$$O_O = \frac{1}{2}O_2 + V_O^{\cdot\cdot} + 2e^{'} \qquad (10)$$

$$2O_O + Ti_{Ti} = Ti_i^{\bullet\bullet\bullet} + 3e^{'} + O_2 \qquad (11)$$

$$2O_O + Ti_{Ti} = Ti_i^{\bullet\bullet\bullet\bullet} + 4e^{'} + O_2 \qquad (12)$$

$$Ti_i^{\bullet\bullet\bullet} = Ti_i^{\bullet\bullet\bullet\bullet} + e^{'} \qquad (13)$$

Previous researches reported that the effect of aliovalent ions, (as impurities or as dopants), on the concentration of electronic charge carriers and related electrical properties depends on both temperature and oxygen activity. In acceptor doped TiO_2 the following defect reactions could take place (A refers to acceptor type dopant with valance state 3^{+}):

$$2A_2O_3 + TiO_2 = 4A_{Ti}^{'} + Ti_i^{\bullet\bullet\bullet\bullet} + 8O_O^X \qquad (14)$$

$$A_2O_3 = 2A_{Ti}^{'} + V_O^{\bullet\bullet} + 3O_O^X \quad \text{(low } PO_2\text{)} \qquad (15)$$

When donor type dopants are introduced, charge neutralization could be maintained by the following defect reactions (D refers to donor type dopant with valance state 5^{+}):

$$2D_2O_5 = 4D_{Ti}^{\bullet} + 10O_o^X + V_{Ti}^{''''} \qquad (16)$$

$$D_2O_5 = 2D_{Ti}^{\bullet} + 5O_O + 2e^{'} \qquad (17)$$

The observed effect of aliovalent ions increases with the decrease of temperature and the increase of oxygen activity [62]. According to trend shown in Figure 2.11, even very low concentration of impurity ions and/or dopants can have a substantial influence on the conductivity of TiO_2 at room temperature. Hence, controlling the effect of impurity ions by introducing of dopants is critical for reducing the electrical conductivity of TiO_2 dielectrics.

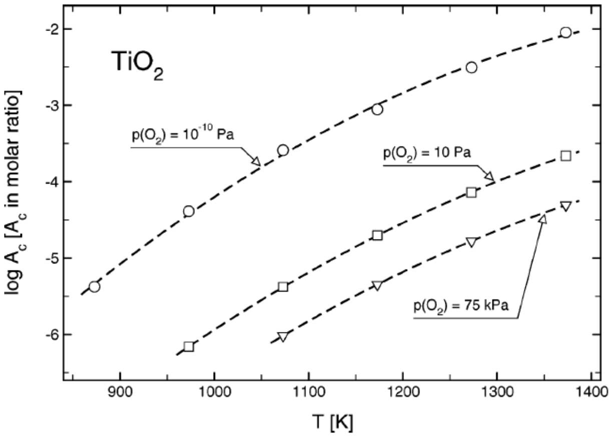

Figure 2.11. Isothermal plots of the critical value of the effective concentration of the acceptors as a function of temperature for TiO_2 (critical value means that above this concentration, the presence of acceptors would have a substantial influence on conductivity) [62].

Most of the recent investigations on dielectric properties of TiO_2 ceramics were focused on the microwave dielectric properties, especially dielectric loss [63, 64]. Both sintering atmosphere [63] and various dopants [64] were found to have a great influence on the dielectric loss of TiO_2 ceramics. Increased quality factor (Q, Q=1/tanδ) was obtained on TiO_2 ceramics annealed in oxygen atmosphere [63] or doped with divalent or trivalent cations with ionic radius between 0.5-0.95Å [64]. Although these results were obtained in the microwave range, the dielectric loss in lower frequencies (< MHz) may also be controlled by these factors, since dielectric loss is believed to be caused by the same origin: oxygen vacancies.

TiO_2 ceramics with nano-sized grains can be fabricated by a variety of techniques such as spark plasma sintering [65] and hot pressing [66]. With the readily available nano-grain sized samples, the effects of grain size on the electrical transportation phenomenon of TiO_2 ceramics have been investigated [67, 68]. Enhanced electrical conductivity (two orders of magnitude higher) was found in nano-grain sized (~50nm) samples in comparison with microcrystalline (~260nm) samples, which was attributed to lowered grain boundary resistivity due to lowered grain boundary solute density when grain size is small [67]. Enhanced conductivity was also observed in the study of TiO_2 ceramics with grain sizes of ~35nm when comparing with TiO_2 ceramics of ~1000nm grain size [68]. In addition, for nanocrystalline TiO_2 ceramics because of high grain boundary density, ionic conductivity became evident [68]. In considering of these results, it is important to find out an optimized grain size range in which TiO_2 ceramics could possess lowest conductivity and highest breakdown strength.

2.5 SUMMARY

There is an immediate demand for fast response capacitors with significantly reduced volume for pulse power applications. Permittivity and dielectric breakdown strength are two vitally important materials' properties that determine the energy density of capacitors. Electrical conductivity and dielectric loss also have a great impact on the energy storage capability of dielectrics.

Traditionally, polymers are commonly used as dielectrics in HED capacitors. However, their low permittivity limits their potential applications in high energy density capacitors particularly at high operating temperatures.

Ceramic dielectrics possess high permittivity and are capable of operating at elevated temperatures. The most important drawback of ceramics lies in their relatively low breakdown strength. Since the dielectric breakdown of ceramics shows a strong dependence on their microstructural features, such as residual porosity and grain size, improved performance can be achieved by optimizing of microstructural development through better ceramic processing techniques.

Various types of dielectrics (linear, ferroelectric, antiferroelectric) have their own advantages and limitations for energy storage. Selection of most appropriate type of dielectric depends on the specific operation conditions. In this dissertation, dielectric properties of TiO_2 ceramics were studied to explore their potential application in HED capacitors. Nano-sized staring powders were used in order to reduce the sintering temperature so as to minimize the loss of oxygen. Emphasis was placed on investigating of the dielectric properties of TiO_2 with respect to material processing conditions and microstructural development. In addition, doping studies with various aliovalent dopants were conducted to improve the dielectric properties at elevated temperatures. By using of nano-sized starting powders, tape-casting method for processing of TiO_2 thick films was explored in order to pave the road for fabrication of prototype MLCCs.

2.6. REFERENCES

1. C. J. Kaiser, *The Capacitor Handbook*, CJ Publishing, 1995.

2. "High Energy Capacitors Overview," General Atomics Energy Products Engineering Bulletin, August 2002.

3. C. A. Randall, H. Ogihara, J.-R. Kim, G.-Y. Yang, C. S. Stringer, S. T.-McKinstry and M. Lanagan, "High Temperature and High Energy Density Dielectric Materials," *Pulsed Power Conference, PPC '09. IEEE* 346-351 (2009).

4. R. Kerrigan, "New Polymer Film Type Cpacitor for Hgh Fequency Hgh Voltage Aplications," *Electronic Components and Technology Conference, 1994. Proceedings 44th*, **1-4** 248-254 (1994).

5. B. Chu, X. Zhou, K. Ren, B. Neese, M. Lin, Q. Wang, F. Bauer, Q. M. Zhang, "A Dielectric Polymer with High Electric Energy Density and Fast Discharge Speed," *Science*, **313** 334-336 (2006).

6. G. R. Love, "Energy Storage in Ceramic Dielectrics," *J. Am. Ceram. Soc.*, **73** 323-328 (2005).

7. T. Hu, J. Juuti, H. Jantunen and T. Vilkman, "Dielectric properties of BST/polymer composite," *J. Eur.Ceram. Soc.*, **27** 3997-4001 (2007).

8. P. Barber, S. Balasubramanian, Y. Anguchamy, S. Gong, A. Wibowo, H. Gao, H. J. Ploehn and Hans-Conrad zur Loye, "Polymer Composite and Nanocomposite Dielectric Materials for Pulse Power Energy Storage," *Materials* **2** 1697-1733 (2009).

9. J. Li, S. L. Seok, B. Chu, F. Dogan, Q. Zhang and Q. Wang, "Nanocomposites of Ferroelectric Polymers with TiO_2 Nanoparticles Exhibiting Significantly Enhanced Electrical Energy Density," *Adv. Mater.* **21** 217-221 (2009).

10. J. Y. Li, L. Zhang and S. Ducharme, "Electric Energy Density of Dielectric Nanocomposites," *Appl. Phys. Lett.* **90** 132901 (2007).

11. Y. Shen, Y. Lin, M. Li, and C. W. Nan, "High Dielectric Performance of Polymer Composite Films Induced by a Percolating Interparticle Barrier Layer," *Adv. Mater.* **19** 1418-1422 (2007).

12. L. An, S. A. Boggs and J. P. Calame, "Energy Storage in Polymer Films with High Dielectric Constant," *IEEE Electr. Insul. M.* **24** 5-10 (2008).

13. P. Kim, N. M. Doss, J. P. Tillotson, P. J. Hotchkiss, M.-J. Pan, S. R. Marder, J. Li, J. P. Calame and J. W. Perry, "High Energy Density Nanocomposites Based on Surface-Modified $BaTiO_3$ and a Ferroelectric Polymer," *AcsNano.* **3** 2581-2592 (2009).

14. S. L. Jiang, Y. Yu and Y. K. Zeng, "Novel Ag–$BaTiO_3$/PVDF three-component nanocomposites with high energy density and the influence of nano-Ag on the dielectric properties," *Curr. Appl. Phys.* **9** 956-959 (2009).

15. J. Du, B. Jones and M. Lanagan, "Preparation and Characterization of Dielectric Glass-Ceramics in Na_2O–PbO–Nb_2O_5–SiO_2 system," *Mater. Lett.* **59** 2821-2826 (2005).

16. E. P. Gorzkowski, M.-J. Pan, B. Bender and C. C. M. Wu, "Glass-Ceramics of Barium Strontium Titanate for High Energy Density Capacitors," *J. Electroceram.,* **18** 269-276 (2007).

17. N. J. Smith, B. Rangarajan, M. T. Lanagan and C. G. Pantano, "Alkali-free glass as a high energy density dielectric material," *Mater. Lett.* **63** 1245-1248 (2009).

18. L. L. Hench and J. K. West, *Principles of Electronic Ceramics*, John Wiley & Sons, 1990.

19. A. J. Moulson and J. M. Herbert, *Electroceramics:Materials, Properties, Applications. 2nd Edition,* John Wiley & Sons, 2003.

20. Kwan Chi Kao, *Dielectric Phenomena in Solids*, Elsevier Academic Press, 2004.

21. Relva C. Buchanan, *Ceramic Materials for Electronics*, Marcel Derker, Inc., 2004.

22. X. Xu, *Characterization of Hexabarium 17-Titanate and its Effects on the Dielectric Properties of Barium Titanate Ceramics*, Ph.D. Dissertation, University of Missouri-Rolla, 2004.

23. J. McPherson, J.-Y. Kim, A. Shanware and H. Mogul, "Thermochemical Description of Dielectric Breakdown in High Dielectric Constant Materials," *Appl. Phys. Lett.,* **82** 2121-2123 (2003).

24. J. McPherson, R. Khamankar and A. Shanware, "Complementary Model for Intrinsic Time-dependent Dielectric Breakdown in SiO_2 dielectrics," *J. Appl. Phys.,* **88** 5351-5359 (2000).

25. J. W. McPherson, J. Kim, A. Shanware, H. Mogul and J. Rodriguez, "Trends in the Ultimate Breakdown Strength of High Dielectric-Constant Materials," *IEEE Transactions On Electron Devices,* **50**(8) 1771-1778 (2003).

26. J. A. Gaudet, R. J. Barker, C. J. Buchenauer, C. Christodoulou, J. Dickens, M. Gundersen, R. P. Joshi, H. G. Krompholz, F. F. Kolb, A. Kuthi, M. Laroussi, A. Neuber, W. Nunnaly, E. Schamiloglu, K. H. Schoenbach, J. S. Tyo, and R. Vidmar, "Research Issues in Developing Compact Pulsed Power for High Peak Power Applications on Mobile Platforms," *Proceedings of the IEEE*, **92**(7) 1144-1165 (2004).

27. H. Bartzsch, D. Glöß, B. Böcher, P. Frach and K. Goedicke, "Properties of SiO_2 and Al_2O_3 Films for Electrical Insulation Applications Deposited by Reactive Pulse Magnetron Sputtering," *Surf. Coating Tech.,* **174-175** 774-778 2003.

28. S. Chao, V. Petrovsky and F. Dogan, "Electrical Breakdown Strength of Alumina Single Crystal and Ceramics," 2006 *Proc. of Advanced Dielectric Materials and Electronic Devices, Materials Science and Technology (MS&T) 2006: Materials and Systems* **1** 707-714 2006.

29. E. K. Beauchamp, "Effect of Microstructure on Pulse Electrical Strength of MgO," *J. Am. Ceram. Soc.*, **54** 484-487 1971.

30. O.Jongprateep, V. Petrovsky and F. Dogan, "Effects of Yttria Concentration and Microstructure on Electric Breakdown of Yttria Stabilized Zirconia," *J. Miner. Met. Mater.*, **18** 9-14 2008.

31. Y. Ye, *Grain Size Dependence of the Dielectric Breakdown Strength of Titanium Dioxide Dielectrics*, Master Thesis, University of Missouri-Rolla, 2003.

32. I. Ryu and H. Kawamura, "On the Thickness Effect of Dielectric Breakdown of Mica and KCl," *J. Phys. Soc. Jpn.,* **9** 438-439 1954.

33. H. Ogihara, C. A. Randall and S. T.-McKinstry, "High-Energy Density Capacitors Utilizing 0.7 $BaTiO_3$-0.3 $BiScO_3$ Ceramics," *J. Am. Ceram. Soc.* **92**(8) 1719-1724 (2009).

34. I-N. Lin, W.-C. Yang and C.-T. Hu, "Base-Metal-Electroded $BaTiO_3$ Capacitor Materials with Duplex Microstructures,"*J. Am. Ceram. Soc.* **87**(5) 851-858 (2004).

35. L. Wu, M.-C. Chure, K.-K. Wu, W.-C. Chang, M.-J. Yang, W.-K. Liu, M.-J. Wu, "Dielectric Properties of Barium Titanate Ceramics with Different Materials Powder Size," *Ceram. Int.* **35**(3) 957-960 (2009).

36. T. Wang, X.-H. Wang, H. Wen, and L.-T Li, "Effect of Milling Process on the Core-Shell Structures and Dielectric Properties of Fine-grained $BaTiO_3$-based X7R Ceramic Materials," *Inter.J. of Miner., Metall. and Mater.* **16**(3) 345-348 (2009).

37. Q. Feng, C. J. McConville and D. D. Edwards “Effect of Oxygen Partial Pressure on the Dielectric Properties and Microstructures of Cofired Base-Metal-Electrode Multilayer Ceramic Capacitors,” *J. Am. Ceram. Soc.* **89**(3) 894-901 (2006).

38. Q. Li, J. Qi , Y. Wang, Z. Gui and L. Li, “Improvement of Temperature-stable $BaTiO_3$-based Dielectrics by Addition of Li_2CO_3 and Co_2O_3,” *J. Eur.Ceram. Soc.* **21**(12) 2217-2220 (2001).

39. Y. Yuan, S. Zhang and W. You, “Preparation of $BaTiO_3$-based X7R Ceramics with High Dielectric Constant by Nanometer Oxides Doping Method,” *Mater. Lett.* **58**(12-13) 1959-1963 (2004).

40. D. E. McCauley, M. S. H. Chu and M. H. Megherhi, “PO_2 Dependence of the Diffuse-Phase Transition in Base Metal Capacitor Dielectrics,” *J. Am. Ceram. Soc.* **89**(1) 193-201 (2006).

41. A. D. Milliken, A. J. Bell and J. F. Scott, “Dependence of Breakdown Field on Dielectric (interelectrode) Thickness in Base-metal Electroded Multilayer Capacitors,” *Appl. Phys. Lett.* **90** 112910 (2007).

42. C. Fu, C. Yang, H. Chen, Y. Wang and L. Hu, “Microstructure and dielectric properties of $BaxSr_{1-x}TiO_3$ ceramics,” *Mater. Sci. Eng. B* **119**(2) 185-188 (2005).

43. I.W. Chen, “Structural Origin of Relaxor Ferroelectrics-Revisited,” *J. Phys. Chem. Solids* **61**(2) 197-208 (2000).

44. L. B. Kong, J. Ma, W. Zhu, O. K. Tan, “Preparation of PMN powders and ceramics via a high-energy ball milling process,” *J. Mater. Sci. Lett.* **20** 1241- 1243 (2001).

45. Y. Zhang, J. Tian, L. Li, Z. Gui, “Influences of d.c. and a.c. Fields on the Dielectric Properties of Relaxor Ferroelectric Ceramics,” *J. Mater. Sci: Materials in Electronics* **11** 347-350 (2000).

46. H. Kanai, K. Harada, Y. Yamashita, K. Hasegawa, S. Mukaeda and K.Handa, “Fine Grained Relaxor Dielectric Ceramics Prepared by Hydrothermally Synthesized Powder,” *Jpn. J. Appl. Phys.* **35** 5122-5125 (1996).

47. Jaffe B, “Antiferroelectric Ceramics with Field-Enforced Transitions: A New Nonlinear Circuit Element,” *Proc. IRE* **49** 1264–1267 (1961).

48. X. Hao, J. Zhai and X. Yao, “Improved Energy Storage Performance and Fatigue Endurance of Sr-Doped $PbZrO_3$ Antiferroelectric Thin Films,” *J. Am. Ceram. Soc.,* **92**(5) 1133-1135 (2009).

49. J. Parui and S. B. Krupanidhi, “Enhancement of Charge and Energy Storage in Sol-Gel Derived Pure and La-modified $PbZrO_3$ Thin Films,” *Appl. Phys. Lett.,* **92** 192901 (2008).

50. J. H. Jang and K. H. Yoon, “Effect of Antiferroelectric Buffer on Electric Fatigue and Leakage in Ferroelectric $Pb(Zr,Sn,Ti)NbO_3$ Thin Films,” *Thin Solid Films*, **401**(1-2) 67-72 (2001).

51. M. Mcquarrie, “Erratum: The Potential of Two Current Point Sources in a Homogeneous Conducting Prolate Spheroid,” *J. Appl Phys.,* **24** 1334-1334 (1953).

52. W. L. Warren, D. Dimos, B.A. Tuttle, R.D. Nasby and G.E. Pike, “Electronic Domain Pinning in $Pb(Zr,Ti)O_3$ Thin Films and its Role in Fatigue,” *Appl. Phys. Lett.,* **65** 1018-1020 (1994).

53. H. M. Duiker, P. D. Beale, J. F. Scott, C. A. Paz de Araujo, B. M. Melnick, J. D. Cuchiaro and L.D. McMillan, “Fatigue and Switching in Ferroelectric Memories: Theory and Experiment,” *J. Appl. Phys.,* **68** 5783-5791 (1990).

54. Q. Jiang, W. Cao and L.E. Cross, “Electric Fatigue in Lead Zirconate Titanate Ceramics,” *J. Am. Ceram. Soc*., **77**(1) 211-215 (1994).

55. W. L. Warren, K. Vanheusden, D. Dimos, G. E. Pike and B. A. Tuttle, "Oxygen Vacancy Motion in Perovskite Oxides,” *J. Am. Ceram. Soc*., **79**(2) 536-538 (1996).

56. L. Zhou, A. Zimmermann, Y.-P. Zeng and F. Aldinger, “Fatigue of Field-Induced Strain in Antiferroelectric $Pb_{0.97}La_{0.02}(Zr_{0.77}Sn_{0.14}Ti_{0.09})O_3$ Ceramics,” *J. Am. Ceram. Soc.,* **87**(8) 1591-1593 (2004).

57. R. A. Parker , “Static Dielectric Constant of Rutile (TiO_2), 1.6-1060°K,” *Phys. Rev.*, **124**(6) 1719-1722 (1961).

58. A. J. Moulson and J. M. Herber, *Electroceramics: Materials, Properties, Applications*, Chapman & Hall, 1990.

59. Y. Ye, *Grain Size Dependence of the Dielectric Breakdown Strength of Titanium Dioxide Dielectrics*, Master Thesis, University of Missouri-Rolla, 2003.

60. J. F. Baumard, D. Panis, A. M. Anthony, “A Study of Ti-O System Between Ti_3O_5 and TiO_2 at High Temperature by Means of Electrical Resistivity,”*J. Solid State Chem*., **20**(1) 43-51 (1977).

61. J. F. Baumard, E. Tani, “Electrical Conductivity and Charge Compensation in Nb doped TiO_2 Rutile,” *J. Chem. Phys*., **67**(3) 857-860 (1977).

62. T. Bak, J. Nowotny, M. Rekas, C.C. Sorrell, "Defect Chemistry and Semiconducting Properties of Titanium Dioxide: I. Intrinsic Electronic Equilibrium," *J. Phys. Chem. of Solids*, **64** 1043-1056 (2003).

63. J. H. Noh, H. S. Jung, J.-K. Lee, J.-R. Kim and K. S. Hong, "Microwave Dielectric Properties of Nanocrystalline TiO_2 Prepared Using Spark Plasma Sintering," *J. Euro. Ceram. Soc.*, **27**(8-9) 2937-2940 (2007).

64. R. C. Pullar, S. J. Penn, X. Wang, I. M. Reaney and N. McN. Alford, "Dielectric Loss Caused by Oxygen Vacancies in Titania Ceramics," *J. Euro. Ceram. Soc.*, **29** 419-424 (2009).

65. N. Masahashi, "Fabrication of Bulk Anatase TiO_2 by the Spark Plasma Sintering Method," *Mater. Sci. Eng. A,* **452-453** 721-726 (2007).

66. A. Weibel, R. Bouchet, R. Denoyel and P. Knauth, "Hot Pressing of Nanocrystalline TiO_2 (anatase) Ceramics with Controlled Microstructure," *J. Euro. Ceram. Soc*., 27 (7) 2641-2646 (2007).

67. C. Demetry and X. Shi, "Grain Size-dependent Electrical Properties of Rutile (TiO_2)," *Solid State Ionics*, **118** 271-279 (1999).

68. P. Knauth and H. L. Tuller, "Electrical and Defect Thermodynamic Properties of Nanocrystalline Titanium dioxide," *J. Appl. Phys*., **85**(2) 897-902 (1999).

PAPER

1. EFFECTS OF SINTERING TEMPERATURE ON THE MICROSTRUCTURE AND DIELECTRIC PROPERTIES OF TITANIUM DIOXIDE CERAMICS

Sheng Chao, Vladimir Petrovsky and Fatih Dogan
Department of Materials Science and Engineering,
Missouri University of Science and Technology, Rolla Missouri, 65409

Abstract

Nanostructured (~200nm grain size) titanium dioxide (TiO_2) ceramics were densified at temperature as low as 800^{o}C by pressureless sintering in pure oxygen atmosphere. Phase transition and microstructural development of sintered samples were studied by X-ray diffraction (XRD) and scanning electron microscopy (SEM). Dielectric properties including d.c. conductivity, dielectric constant, loss tangent and dielectric breakdown strength (BDS) were determined for samples sintered at various temperatures. The influence of sintering temperature on the microstructural development, defect chemistry and dielectric properties of TiO_2 is discussed. Nanostructured TiO_2 ceramics with high sintering density (>98%) lead to improved dielectric properties; high BDS (~1800KV/cm), low electrical conductivity ($\sim 5\times10^{-15}$ S/cm), high dielectric constant (~130) and low loss tangent (~0.09% at 1kHz), promising for application in high energy density capacitors.

Keywords

Titanium dioxide, Dielectric properties, Space charge, Grain size, Energy storage

Introduction

TiO_2 as one of the widely used metal oxides has broad range of applications, including pigments, gas and humidity sensors, catalyst support, solar cells and capacitors [1-6]. As a dielectric material, TiO_2 combines the merit of both relatively high dielectric constant [7] and high BDS [8] which are two important parameters for capacitors with high energy density. Therefore it has the potential to be utilized in high energy density capacitors, in that the energy density of dielectrics is mainly determined by dielectric constant and BDS. Fig. 1 shows the relationship between the electric displacement (D, C/m^2), electric field (E, V/m) and volumetric energy density (W, J/m^3) for ideal linear dielectrics. If the dielectric constant of the material is >>1, polarization (P, C/m^2) is used instead of dielectric displacement.

Although TiO_2 has been widely studied with respect to synthesis of nanosized powders [9,10], thin film fabrication [11,12] and sintering of nanostructured TiO_2 ceramics [13-15], little attention has been paid on dielectric properties of nanostructured bulk TiO_2 ceramics. It is well known that the properties of electroceramics are affected by their microstructural features (such as grain size, porosity, secondary phases) and defect structure (such as point and electronic defects). The objectives of this study are to investigate the effect of sintering conditions on the microstructural development and dielectric properties of TiO_2 ceramics for potential application in high energy density capacitor.

Experimental

Sintering studies of TiO_2 were conducted using nanosized TiO_2 powders (Nanophase Technologies Corporation Romeoville, IL). Powder characteristics and main impurities (from the product data sheet) are shown in Table 1 and 2. Green compacts were prepared by uniaxial pressing of powders (without binder) at ~100MPa followed by cold isostatic pressing at ~300MPa . Sintering of the samples was conducted at various temperatures (700^{o}C-1000^{o}C) in pure oxygen (1 atm.) for 12hrs with a heating and cooling rate of 4 and 5^{o}C/min, respectively. Sintered densities were determined by Archimedes' method using water as immersion liquid and assuming theoretical densities of anatase 3.89g/cm^3 and rutile 4.25g/cm^3 [14]. Phase evolution of the samples at various temperatures was determined by XRD (Philips X'Pert, Holand). Microstructural development of as-fired fracture surfaces was observed by SEM (Hitachi S4700, Japan). Grain size of the samples was determined by linear intercept method by counting of at least 100 grains of SEM images.

For electrical measurements, the samples (~10mm diameter and ~0.8mm thickness) were polished using 5µm diamond suspension and electroded with silver paste as top and bottom electrodes. Electrical properties were measured in a temperature controllable Delta 9023 environmental chamber (Delta Design, Inc. San Diego, CA, USA) in air. D.C. conductivity measurements were performed using Keithley 6517 Electrometer (Keithley

Instruments, Cleveland, USA). Dielectric constant of the samples was calculated according to the capacitance measured with Solartron 1260 impedance analyzer connected with Solartron 1296 dielectric interface (Solartron analytical, Hampshire, England) in the frequency range of 1 Hz to 1 M Hz and voltage amplitude of 1 V. Polarization as a function of electrical field was measured with a ferroelectric tester (RT6000, Radiant Technology, NM, USA). For BDS measurements, d.c. voltage was supplied by a Spellman SL30 high voltage generator (Spellman high voltage electronics corporation, New York, USA), with a fixed ramp rate of 250V/sec. A dimpled electrode configuration was employed for BDS measurements (Fig. 2.) to ensure that maximum electrical stress is concentrated at the thinnest point (~80-100μm) of the sample. This sample configuration allowed to measure intrinsic BDS of the samples by eliminating of electrical field enhancement at the electrode edges [16]. A more detailed description of sample preparation and BDS measurements is given elsewhere [17].

Results and Discussion

Microstructural Development

Relative densities of TiO_2 ceramics sintered at various temperatures are shown in Fig. 3. A sintering density of 97.3 % was obtained at 780^{o}C, further increase of the sintering temperature up to 1000^{o}C lead to nearly full densification of the samples. Although TiO_2 nanopowders have been densified at even lower temperatures (700^{o}C by spark plasma sintering [18] or 400^{o}C by hot-pressing at very high pressures [14]), in present study highly dense TiO_2 ceramics were obtained by conventional pressureless sintering at 800°C. Enhanced sintering of the samples is attributed to nanosized starting powders and well-compacted (~ 60% packing density) green pellets after isostatic pressing. As shown in Table 3, a high green density led to a high sintering density as it applies for densification of most ceramic materials.

Fig. 4 shows the microstructure of TiO_2 ceramics with a grain size ranging from ~0.15μm for samples sintered at 700°C to ~2.70μm after sintering at 1000°C. Residual porosity is observed in samples sintered at temperatures below 800°C (Fig. 4 (g) and (h)) in accordance with the density measurements. The samples sintered at lower temperatures revealed a uniform grain size, whereas a bimodal grain size distribution was observed in samples sintered at higher temperatures, indicating that the grain growth occurred according to Ostwald-ripening mechanism.

Fig. 5 shows XRD patterns of TiO_2 samples sintered at various temperatures. Weak intensity peaks corresponding to the remaining anatase phase (JCPDS 73-1764) were identified in the sample sintered at 700°C while samples sintered at temperatures equal to or higher than 750°C showed the rutile phase (JCPDS 21-1276). The temperature of anatase to rutile phase transformation is reported to be ~915°C [19]. In the present study, greatly reduced phase transition temperature is attributed to nanosized starting powders with high specific surface area. Similar results were obtained in a study by Eastman [20], that reported the completion of anatase to rutile transformation of TiO_2 nanosized powders between 650°C and 800°C.

Dielectric Properties

Dielectric properties were measured on selected samples sintered at 700°C, 800°C, 900°C and 1000°C (named as T7, T8, T9 and T10, respectively afterwards). The frequency dependence of dielectric constant and loss tangent of these samples measured at room temperature are shown in Fig. 6. While the dielectric constant of sample T7 decreased from 133 at 1 Hz to 113 at 100 kHz, a more stable frequency dependent dielectric constant was observed in case of sample T8. In the frequency range from 1 Hz to 100 kHz, dielectric constant of sample T8 decreased slightly from 134 to 133. Relatively large variation in dielectric constant of sample T7 is attributed to high d.c. conductivity that led to high apparent dielectric constant and high loss tangent at low frequencies. Because of the lower sintering density of sample T7, the intrinsic dielectric constant measured at high frequency (100 kHz) was ~15% lower than that of sample T8.

Unlike low temperature sintered samples (T7 and T8), the dielectric constant of sample T9 and T10 was found to have a strong dependence on the measuring frequencies. At low frequencies (1-1 kHz), the dielectric constant of T9 and T10 exceeded the intrinsic dielectric constant of randomly orientated polycrystalline TiO_2 ceramics [21]. With increasing frequency, the dielectric constant gradually decreased and finally reached a plateau with K: ~133, matching the dielectric constant of sample T8. High dielectric constant at low frequencies may arise from a polarization mechanism other than electronic and ionic polarizations. As the external stimulus frequency increases, this polarization mechanism gradually lag behind and damp out, resulting in a decrease of the dielectric constant as the frequency increases.

As shown in Fig. 6 (b), accompanied with this dielectric constant anomaly, a pronounced loss tangent peak was observed for samples sintered at higher temperatures (T9 and T10). It is attributed to the polarization mechanism that contributes to both dielectric constant and dielectric loss. According to the frequency range at which this relaxation process took place, it is likely to be caused by the space charge polarization.

The loss tangent measured from 25°C to 200°C is shown in Fig. 7. For sample T7, the lowest loss was measured at 100°C instead of 25°C, that was caused by the influence of humidity. With further increase of the temperature, loss tangent increases due to higher electrical conductivity. For sample T8 with high sintering density, the loss tangent increases gradually with the increase of temperature so that the measurement was not influenced by humidity. A decreasing of loss tangent with increasing frequency indicates the dominance of conduction losses. In case of TiO_2 samples sintered at higher temperatures, the loss peak found at room temperature still exists at high temperatures and shifts towards higher frequencies with increasing temperature. At the same time, the magnitude of the loss peak increases with increasing temperature. This observation shows that the relaxation process is thermally stimulated and the enhanced magnitude of loss peak indicates increased number of charge carriers involved in this process.

By determining the position of characteristic frequency (f_p) of the loss peak, angular frequency (ω_p, $\omega_p=2\pi f_p$) was calculated. The temperature dependence of angular frequency was found to followed the Arrhenius law as shown in Fig. 8,

$$\omega_p = \omega_0 \exp(\frac{-E_a}{\kappa_B T}) \qquad (1)$$

where ω_0 is the pre-exponential factor, E_a is the activation energy and κ_B is the Boltzmann constant. Activation energies of 0.41eV and 0.48eV were obtained from sample T9 and T10, respectively. These values are close to the reported activation energy for electron hopping process [22].

It is interesting that this relaxation process can only be found in TiO_2 sintered at high temperatures. The presence of space charge polarization indicates nonuniform resistivity within the microstructure of the samples. Since no secondary phase was identified by XRD and SEM, grain boundaries are very likely to be the region where charge pile-up takes place due to resistivity discontinuity. With the increase of sintering temperature, the grain size becomes larger whereas grain boundary density (defined as grain boundary surface area per unit volume) decreases. Therefore, TiO_2 ceramics sintered at higher temperatures with larger grain size would have higher impurity concentration at grain boundaries as aliovalent dopants/impurities tend to segregate at the grain boundaries due to the elastic strain energy and electrostatic driving force [23].

TiO_2 starting powders have ~0.1 wt% of impurity concentration, with Fe, Mg, Ca, Al as main foreign ions (Table 2). Since the ionic radius of these elements (Fe^{2+}: 0.74Å; Fe^{3+}: 0.64Å; Mg^{2+}: 0.66Å; Ca^{2+}: 0.99Å; Al^{3+}: 0.51Å) is close to the ionic radius of Ti (Ti4+: 0.68Å), substitution of Ti lattice can take place. Hence, segregation of impurity ions at the grain boundaries is expected after high temperature sintering. When the impurities ions substitute the normal titanium site, point defects of $M_{Ti}^{'}$ or $M_{Ti}^{''}$ (M represents Fe, Mg, Ca, Al) could lead to formation of negatively charged grain boundary cores generating an electron depletion layer in the nearby space charge region. In the study of Y_2O_3 doped TiO_2, due to Y segregation to the grain boundaries, negatively charge $Y_{Ti}^{'}$ defects gave rise to the space charge effect [24].

In order to explore this assumption, high temperature impedance spectroscopy measurements were conducted and presented as Cole-Cole plot (Fig. 9). For sample T8, a single semi-circle was obtained, while a small peak at lower frequencies was also observed. On the contrary, in case of the samples T9 and T10, their impedance responses clearly show two suppressed semi-circles. An equivalent circuit consisting of two parallel capacitor (R) - constant phase element (CPE) connected in series can be used to represent the electrical response of the dielectric (insert in Fig. 9). The first high frequency R1-CPE1 circuit was attributed to the grain interior response, whereas the second low frequency R2-CPE2 circuit was attributed to the grain boundary response, determined by their capacitance values. It is revealed that the resistance of grain interior dominates in sample T8. With the increase of sintering temperature, contribution of grain boundaries to the total resistance of the dielectric increases. Values of grain interior resistivity (ρ_g), grain boundary resistivity (ρ_{gb}) and their relative ratio were calculated by the following equations [25]:

$$\rho_g = R_g \frac{A}{L} \qquad (2)$$

$$\rho_{gb} = \frac{R_{gb} C_{gb}}{R_g C_g} \rho_g \qquad (3)$$

where A is the electrode area and L is the sample thickness; C_g, C_{gb} and R_g, R_{gb} are the capacitance and resistance of grain interior and grain boundary, respectively. Table 4 shows a summary of the grain interior and grain boundary resistivity and their relative ratio. With the increase of sintering temperature, there is a substantial increase in the ratio of grain boundary resistivity to grain interior resistivity. Therefore, significantly enhanced resistivity difference between grain interior and grain boundary found in TiO_2 ceramics sintered at higher temperature gave rise to space charge polarization.

Constant phase element is used instead of ideal capacitor when the center of the semi-circle is depressed below the $Z^{'}$-axis [24]. The magnitude of depression is a measure of the deviation from ideal capacitance behavior due to chemical or geometrical inhomogenity [26]. From Table 4, it can be seen that the magnitude of inhomogenity increases with the increase of sintering temperature. The semi-circle corresponding to grain boundaries was found to be more depressed than that of the grain interior, which can be attributed to a gradually changing distribution of impurity concentration among grain interiors and grain boundaries. Similar observations were made in the study of yttrium doped TiO_2 [24], so that the degree of nonuniformity in the grain boundary region increases with the increase of yttrium dopant concentration. This effect was explained by the geometric misorientation associated with grain boundaries as the misorientation parameters is to a great extent determined by the amount of excess impurity solutes at grain boundaries [27]. In the present study, since all impurities were from the starting powders, the total amount of impurities is assumed to be the same for all samples. Therefore, gradually increased nonuniformity in grain interior should be better explained by enhanced chemical inhomogenity as original homogenously distributed impurities starts to segregate to the grain boundaries as sinter temperature increases.

In summary, it is believed that as the sintering temperature increases, more impurity ions segregated at the grain boundary region leading to greater differences in resistivity between grain interior and grain boundaries. As a result, space charge polarization occurs in TiO_2 sintered at high temperature, which accounts to a high apparent dielectric constant and loss peak.

Arrhenius plot of d.c. conductivity of TiO_2 sintered at various temperatures is shown in Fig. 10. Except for sample T7, other TiO_2 samples sintered at lower temperatures show lower conductivity. Activation energies calculated by best linear fitting for sample T7, T8, T9 and T10 are 0.79eV, 0.76eV, 0.75eV and 0.76eV, respectively (data were taken from 100°C-200°C to exclude the influence of humidity). This activation energy is much lower than half of the band gap of TiO_2 (band gap of TiO_2:2.90-3.33V [28]), suggesting that in this temperature range, conductivity is controlled by defects generated during sintering at high temperatures and/or by intrinsic impurities present in the starting powders. An activation energy of ~1.23eV was obtained in the study of TiO_2 ceramics with an average grain size ~270nm in the temperature range of 350°C to 750°C [29]. Significantly lower activation energy observed in present study is attributed to migration of charge carriers and does not contribute to formation of new defects. Higher conductivity measured on samples sintered at higher temperatures is attributed to higher concentration of charge carriers, since TiO_2 ceramics are prone to reduction at elevated temperatures [30]. This process can be described by the following defect reactions:

$$O_o^X = V_o^{\bullet\bullet} + 2e' + \frac{1}{2}O_2 \qquad (4)$$

$$2O_O + Ti_{Ti} = Ti_i^{\bullet\bullet\bullet} + 3e' + O_2 \qquad (5)$$

For sample T7, its particular high conductivity is due to the presence of remaining open porosity that serves as fast conduction passes [31].

The polarization-electric field (P-E) relationship of the samples was measured at room temperature as shown in Fig. 11. Samples T7 and T8 reveal characteristics of linear dielectrics with a linear P-E relation. On the contrary, P-E curves with a loop were obtained for samples T9 and T10. This non-linear behavior is ascribed to contribution of space charge polarization, since the crystal structure of TiO_2 does not possess permanent dipoles. Judging from the shape of P-E curves, sample T9 and T10 would not be desired for energy storage applications, as the encircled area in the loop represents the energy loss as heat upon discharge. The energy storage efficiency (defined as the ratio of retractable energy upon discharge to total energy stored when charging) of sample T9 and T10 are only 61.6% and 59.2%, respectively. Slim linear P-E curves obtained from samples T7 and T8 represent improved efficiencies with 90.6% and 92.1%, respectively. High energy storage efficiency is of critical importance because energy loss as heat increases the temperature of the dielectrics leading to higher conductivity, while enhanced conductivity in turn leads to higher loss and heat generation. Repeating of this cycle would eventually lead to thermal breakdown of the dielectric when leakage current reaches a critical level.

Dielectric breakdown strength is of prime importance in the development of dielectric materials for high energy density capacitor application. The relation between BDS and energy density is self-evident for linear dielectrics as the volumetric energy density is given by:

$$W = \frac{1}{2}\varepsilon_0 \varepsilon_r E_b^2 \qquad (6)$$

where W is the energy density (J/m^3); ε_0 is the permittivity of free space (8.85×10^{-12} F/m); ε_r is the permittivity of the dielectric material and E_b is the BDS (V/m). More reliable BDS data can be obtained by excluding of electrical field enhancement effects at the electrode edges. However, field strength is enhanced by a significant but unknown factor at the dielectric/electrode/media triple point, leading to premature edge breakdown [32]. In this study, the problem of edge breakdown was successfully overcome by using of dimpled sample geometry (Fig. 2). BDS data shown here were based on measurements with confirmed breakdown crater in the center of the dimple where the thinnest section of the sample is.

Room temperature BDS of the samples sintered at various temperatures are summarized in Fig. 12. Each data point is an average of six or more samples. It can be seen that with the increase of sintering temperature, BDS first increases from 640 kV/cm (T7) to a peak value of 1870 kV/cm (T8) and decreases to 831 kV/cm (T10) with further increase of the sintering temperature. This trend shows that BDS has a reverse relation with d.c. conductivity, i.e., the lower is the conductivity the higher is the BDS.

TiO_2 sintered at 700^{o}C has the lowest BDS mainly due to its residual porosity. Detrimental effects of porosity on the BDS of dielectric materials are well known [33]. Residual pores can intrigue partial gas discharges leading to ionization breakdown. The presence of pores in the dielectric can also lead to development of electrical field induced local stresses that can exceed externally applied electric field [34]. Beauchamp found that the BDS of MgO ceramics decreased almost by a factor of three when the porosity increased to 12% [35].

At sintering temperature higher than 800^{o}C, all samples achieved a relative density over 99%. Hence, the decrease of BDS with further increase of sintering temperature cannot be attributed to the effect of porosity. Instead, it may be associated with the grain size effect. Tunkasiri *et al* [36] found a relation of $\mathrm{BDS} \propto \mathrm{G}^{-0.5}$ between BDS and grain size (G) in $BaTiO_3$. A similar relationship, BDS $\propto G^{-0.5}$, was found in TiO_2 dielectrics with average grain size ranging from 0.27μm to 11μm [37].

One possible explanation for higher BDS found in fine grain ceramics is the reduction of the critical flaw size. As demonstrated by S. Carabajar and *et al* [38] both mechanical strength and dielectric strength of ceramic materials were affected by critical flaw size. However, in this study, coarse grained TiO_2 has slightly higher density than that of fine grained sample, and no pores and microcracks were observed by SEM. Hence, this explanation based on critical flow size does not seem to be plausible for the present study. It was noticed that the most resistive part in coarse grained TiO_2 (T9 and T10) is the grain boundary; whereas the most resistive part in fine grained TiO_2 (T8) is the grain interior. Therefore, when an electric field is applied significant portion of the field is assumed to be hold at the grain boundaries in coarse grained TiO_2, while the opposite is expected to occur in fine grained TiO_2. Since the grain boundary is a thin layer with a thickness in the range of several nanometers, a breakdown along the grain boundaries is expected at lower electrical fields. During BDS tests, a leakage current was detected before the breakdown in samples T9 and T10, that may be indicative for initiation of voltage breakdown along the grain boundary parts. Since the microstructure of the sample T8 is more uniform with a fine grain size, it is assumed that the BDS is controlled by the grain interior while breakdown along the grain boundaries is avoided. Voltage breakdown of the sample T8 always occurs before any detectable leakage current (>1μA) can be observed.

Previously reported BDS results of TiO_2 as thin films [39] or bulk ceramics [40] are relatively low comparing with the results in this study. However, McPerson *et al.* [41] predicted that the BDS of TiO_2 could reach ~2500 kV/cm according to a thermochemical model. Since this model is based on invariable physical parameters of TiO_2 such as bond strength and crystal structure, this value should be considered as the intrinsic BDS of TiO_2. Our experimental results indicate that dense and nanostructured TiO_2 ceramics could possess BDS approaching to the theoretical value.

Fig. 13 shows melting and crack formation at the location where breakdown occurred in sample T8. The breakdown process can be described as an explosive and sparking event, during which a sudden release of energy results in melting of the bulk material and rapid solidification. Breakdown crater with similar features were also observed in $BaTiO_3$ ceramics [36] and Al_2O_3 ceramics [42].

So far, it is not conclusive to determine the exact breakdown mechanism whether it is intrinsic (electronic), thermal, ionic, or electromechanical breakdown or a combination of them for TiO_2 ceramics studied in this work. Generally speaking, for ceramic materials the initial stage of breakdown is dominated by an electronic process whereas the later stages are controlled by thermal and electromechanical processes [42]. For sample T7 due to the residual porosity and high conductivity, ionization breakdown and or thermal breakdown mechanisms are more likely to be predominant. For sample T8, the breakdown mechanism may be electronic in nature. In case of samples T9 and T10, their breakdown events are believed to be controlled by premature breakdown of their grain boundaries as discussed in previous sections. Further studies are needed to understand the nature of the BDS with respect to voltage ramp rate, different electrode materials, temperature, sample thickness and other parameters.

Summary

Nanostructured dense TiO_2 ceramics were prepared by conventional pressureless sintering at 800^oC in oxygen atmosphere. It was found that TiO_2 ceramics with low sintering density or large grain size exhibit relatively high electrical high conductivity and dielectric loss. Space charge polarization was observed in TiO_2 ceramics sintered at high temperatures as a result of impurity segregation at grain boundaries. High BDS was achieved in TiO_2 ceramics with low conductivity and homogenous microstructure with smaller grain size. According to Equation (6), a potential energy density ~15 J/cm^3 can be obtained on nanostructured $TiO_{2.}$ Hence, nanostructured TiO_2 ceramics are promising dielectric materials for high energy density capacitor and pulsed power applications.

Acknowledgments

The authors like to thank Dr. Wayne Huebner and Dr. Robert Schwartz (Missouri University of Science and Technology) for their valuable discussion and correction of the manuscript. This work was supported by a MURI program sponsored by Office of Naval Research under Grant No. N000-14-05-1-0541.

References

1. Yeh YC, Tseng TT, Chang DA (1989) J Am Ceram Soc72:1472
2. Fukushima K, Yamada I (1989) J Appl Phys 65:619

3. Regan BO, Graetzel M (1991) Nature (London) 353:737

4. Bard AJ (1980) Science 207:139

5. Ha HY, Nam SW, Lim TH, Oh IH, Hong SA (1996) J Membr Sci111:81

6. Hoffman MR, Martin ST, Choi W, Bahenmann DW (1995) Chem Rev 95:69

7. Dervos CT, Thirios EF, Novacovich J, Vassiliou P, Skafidas P (2004) Mater Lett 58:1502

8. Ye Y, Zhang SC, Dogan F. Schamiloglu E, Gaudet J, Castro P, Roybal M, Joler M, Christodoulou C (2003) 14th IEEE International 1:719

9. Chen XQ, Gu GB, Liu HB, Cao ZN (2004) J Am Ceram Soc 87:1035

10. Lee KR, Kim SJ, Song JS, Lee JH, Chung YJ, Park S (2002) J Am Ceram Soc 85:341

11. Kim JH, Fujita S, Shiratori S (2006) Thin Solid Films 499:83

12. Zhou XS, Lin YH, Li B, Li LJ, Zhou JP, Nan CW (2006) J Phys D-Appl Phys 39:558

13. Hahn H, Logas J, Averback RS (1996) J Mater Res 5:609

14. Liao SC, Colaizzi J, Chen YJ, Kear BH, Mayo WE (2000) J Am Ceram Soc 83:2163

15. Angerer P, Yu LG, Khor KA, Krumpel G (2004) Mater Sci Eng A 381:16

16. Yoshimura M, Bowen HK J. (1981) Am Ceram Soc 64:404

17. Chao S, Petrovsky V, Dogan F, (2006) Proceeding of Advanced Dielectric Materials and Electronic Devices, Materials Science and Technology (MS&T) 2006: Materials and Systems 1:707

18. Lee YI, Lee JH, Hong SH, Kim DY (2003) Mater Res Bull 38:925

19. Campbell IE, Sherwood EM (Eds.) (1967) High-Temperature Materials and Technology, Wiley, New York
20. Eastman JA (1994) J Appl Phys 75:770
21. Tobar ME, Krupka J, Ivanov EN, Woode RA (1998) J Appl Phys 83:1604
22. Tuller HL, Nowick AS(1977) J Phys Chem Solids 38:859
23. Yan MF, Cannon RM, Bowen HK (1983) J Appl Phys 54:764
24. Wang QL, Varghese O, Grimes CA, Dickey EC (2007) Solid State Ionics 178:187
25. Guo X, Maier J (2001) J Electrochem Soc 148:E121
26. Macdonald JR (1987) Impedance Spectroscopy: Emphasizing Solid Materials and Systems, John Wiley & Sons, New York
27. Wynblatt P, Rohrer GS, Papillon F (2003) J Eur Ceram Soc 23:2841
28. Bak T, Nowotny J, Rekas M, Sorrell CC J Phys Chem Solids (2003) 64:1043
29. Hoshino K, Peterson NL, Wiley CL (1985) J Phys Chem Solids 46:1397
30. Pullar RC, Penn SJ, Wang XR, Reaney IM, Alford NM (2009) J Eur Ceram Soc 29:419
31. Song SH, Wang X, Xiao P (2002) Mater Sci Eng B 94:40
32. Yoshimura M, Bowen HK (1981) J Am Ceram Soc 64:404
33. Morse CT, Hill GJ (1970) Proc Br Ceram Soc18:23
34. Young AL, Hilmas GE, Zhang SC, Schwartz RW (2007) J Mate Sci 42:5613
35. Beauchamp EK J Am Ceram Soc (1971) 54:484
36. Tunkasiri T, Rujijanagul G (1996) J Mater Sci Lett 15:1767
37. Yang Y Grain Size Dependence of the Dielectric Breakdown Strength of Titanium Dioxide Dielectrics, Master Thesis, University of Missouri-Rolla, 2003.

38. Carabajar S, Olagnon C, Fantozzi G, Gressus CL (1995) Conference on Electrical Insulation and Dielectric Phenomena Proceedings, IEEE Annual Report 11:278
39. Souni ME, Oja I, Krunks M (2004) J Mater Sci Materials in Electronics 15:341
40. Kishimoto A, Koumoto K, Yanagida H (1989) J Am Ceram Soc 72:1373
41. McPherson J, Kim JY, Shanware A, Mogul H (2003) Appl Phys Lett 82:2121
42. Owate IO, Freer R (1992) J Appl Phys 72:2418

Figures:

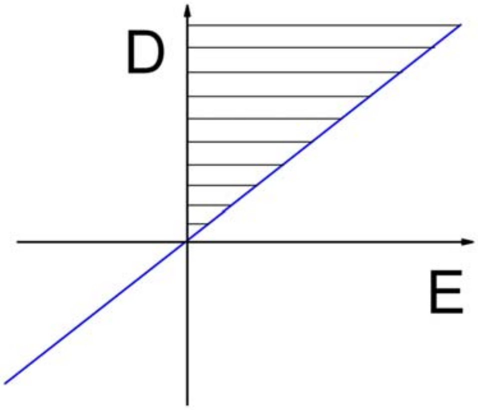

Fig. 1. Electric displacement (D) versus electric field (E) for ideal linear dielectrics (shaded region represents the volumetric energy density upon discharge.).

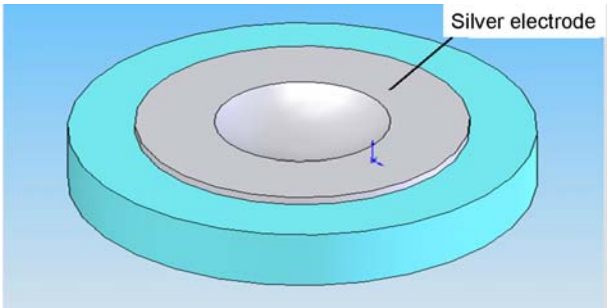

Fig. 2. Schematic drawing of a dimpled sample for BDS measurements (not to scale).

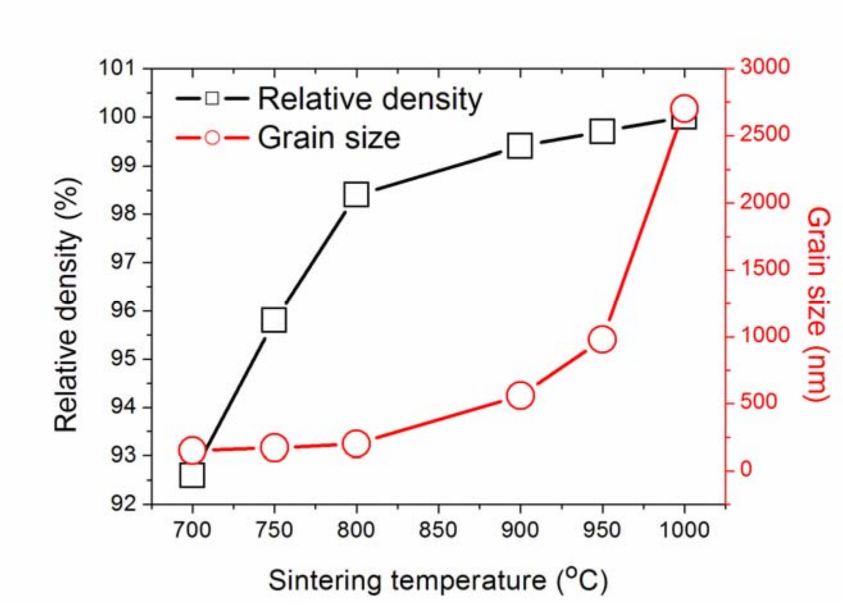

Fig. 3. Relative density and grain size of TiO_2 ceramics as a function of sintering temperature.

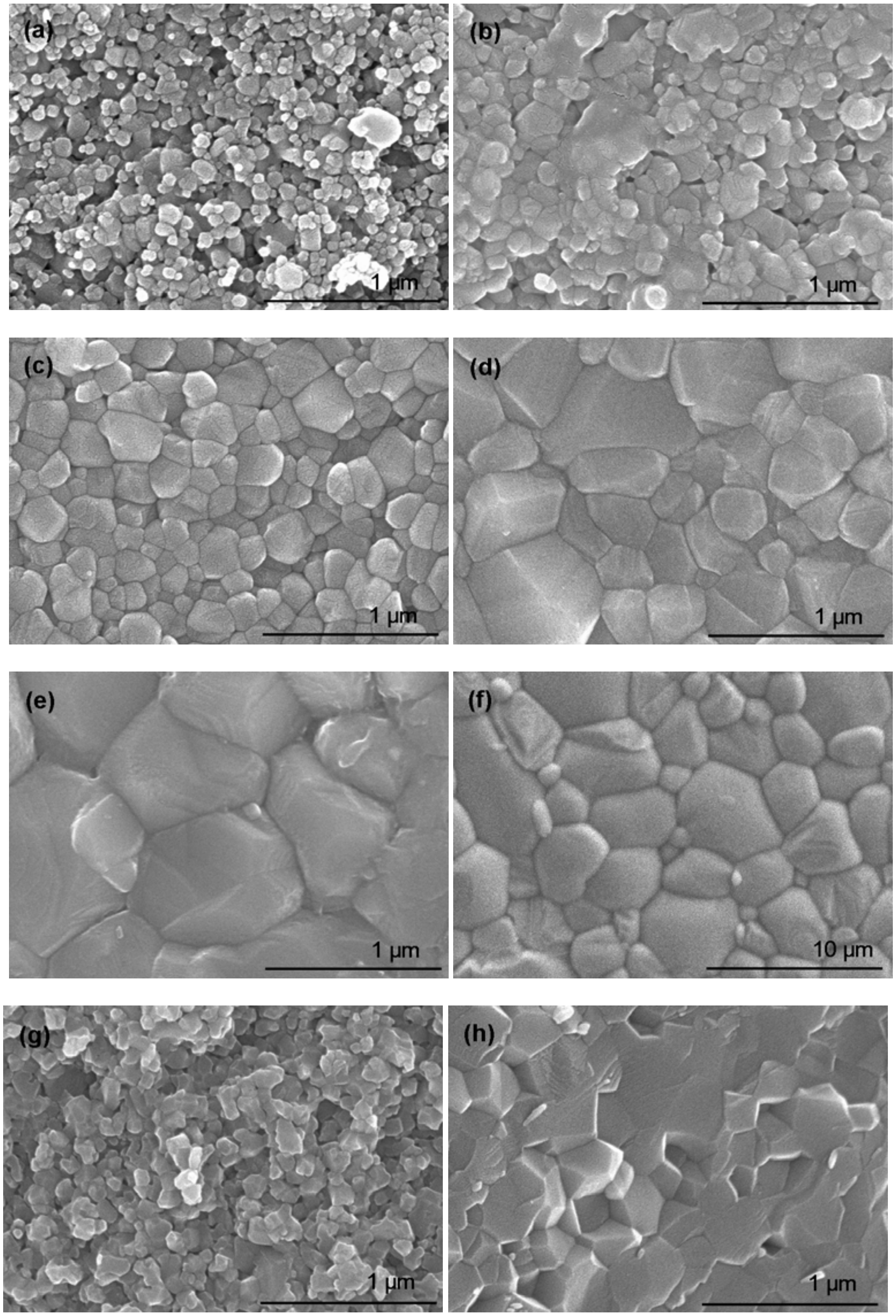

Fig. 4. Microstructural development of TiO_2 ceramics sintered at (a) 700°C (b) 750°C, (c) 800°C, (d) 900°C, (e) 950°C, (f) 1000°C, (g) 700°C (fracture surface), (h) 800°C (fracture surface).

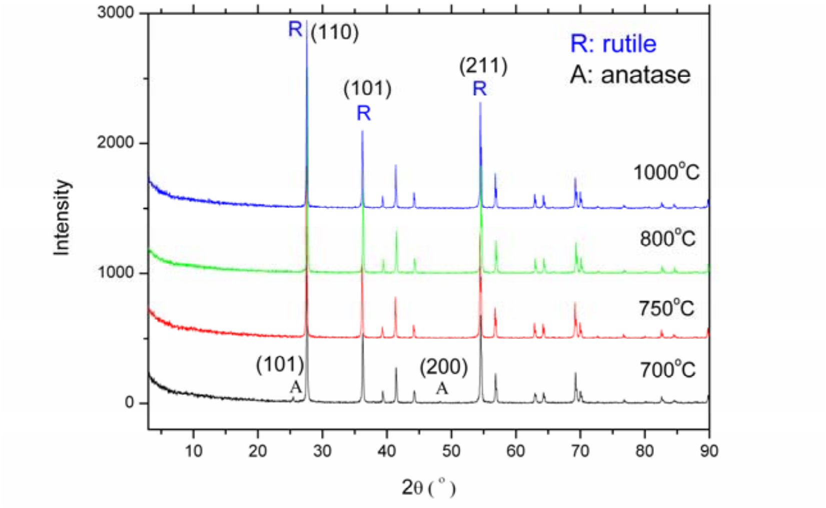

Fig. 5. XRD patterns of TiO_2 samples sintered at various temperatures (all peaks were indexed to rutile or anatase phase).

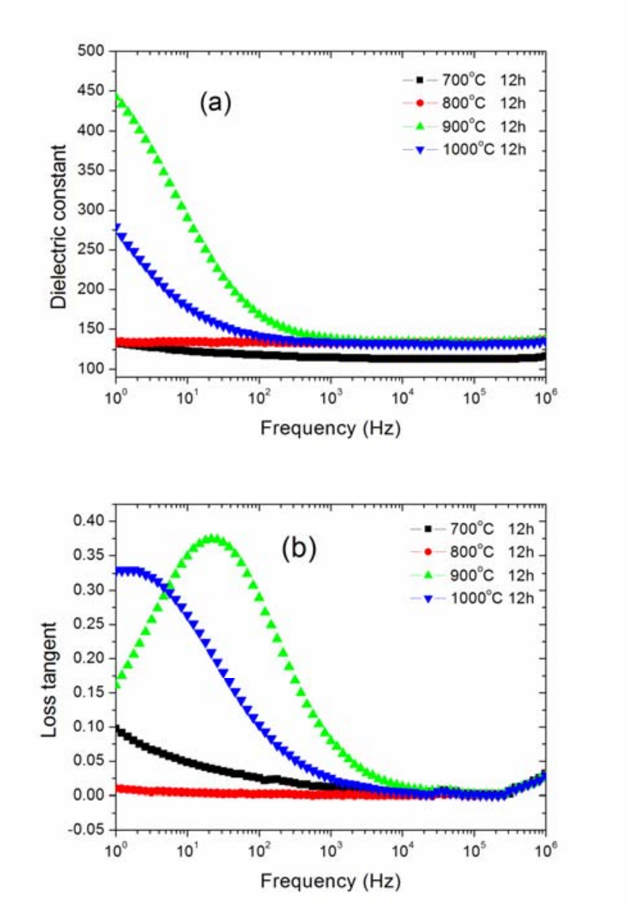

Fig. 6. (a) Dielectric constant and (b) loss tangent of TiO_2 samples sintered at various temperatures.

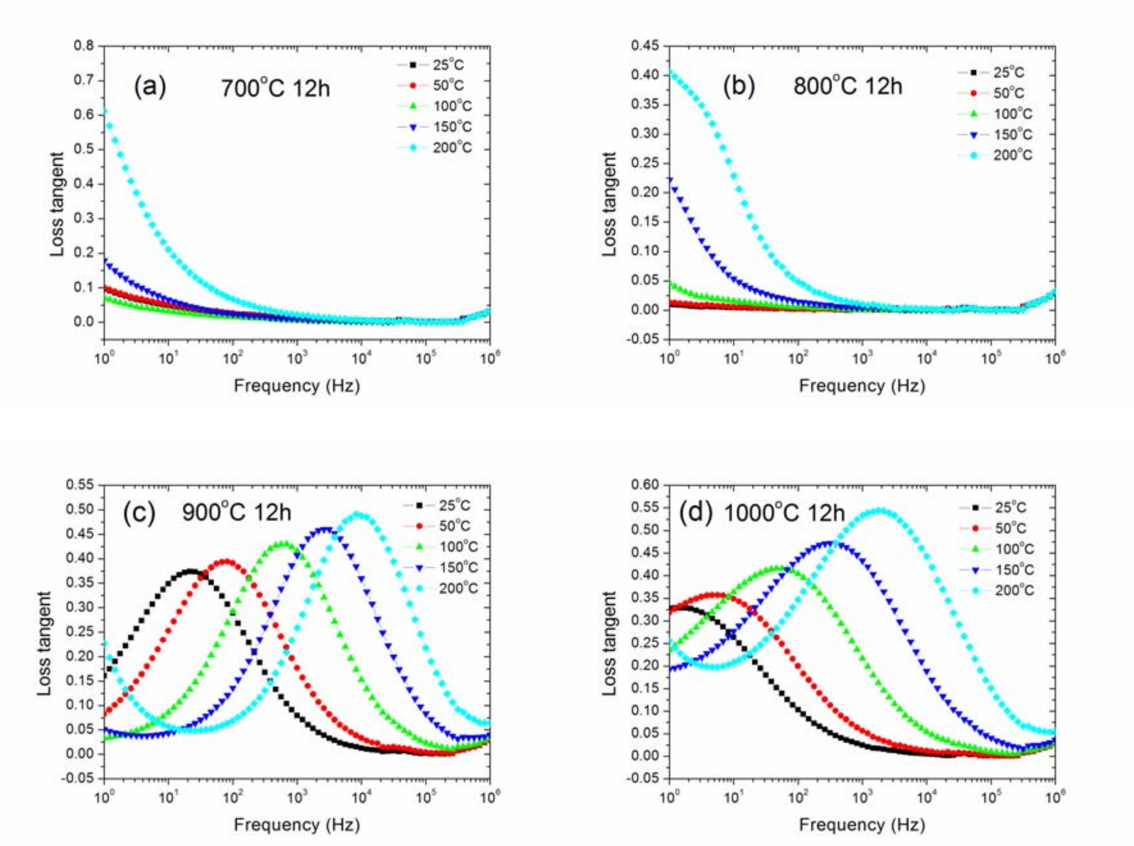

Fig. 7. Loss tangent measured from 25°C to 200°C for TiO_2 samples sintered at (a) 700°C; (b) 800°C; (c) 900°C and (d) 1000°C.

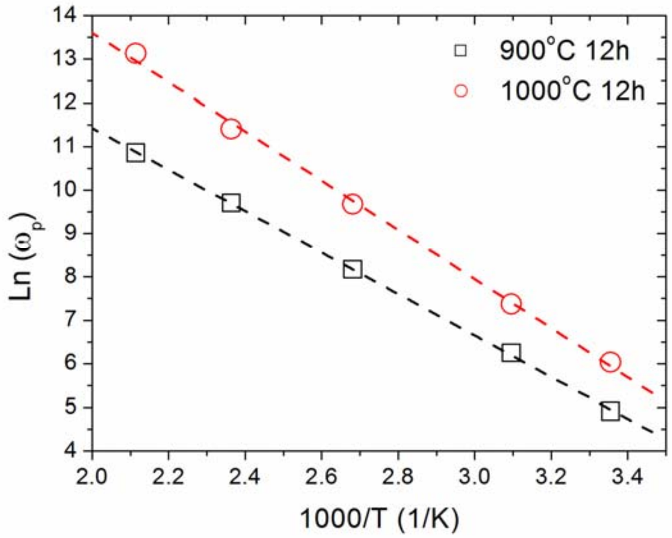

Fig. 8. Temperature dependence of loss peak angular frequency for TiO_2 ceramics sintered at 900°C and 1000°C.

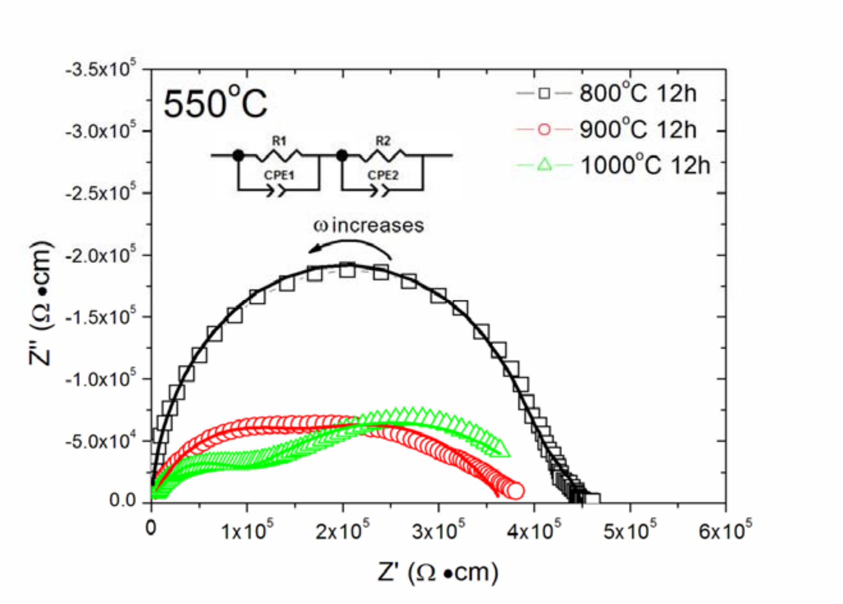

Fig. 9. Cole-cole plot of the samples T8, T9 and T10 measured at 550°C in air.

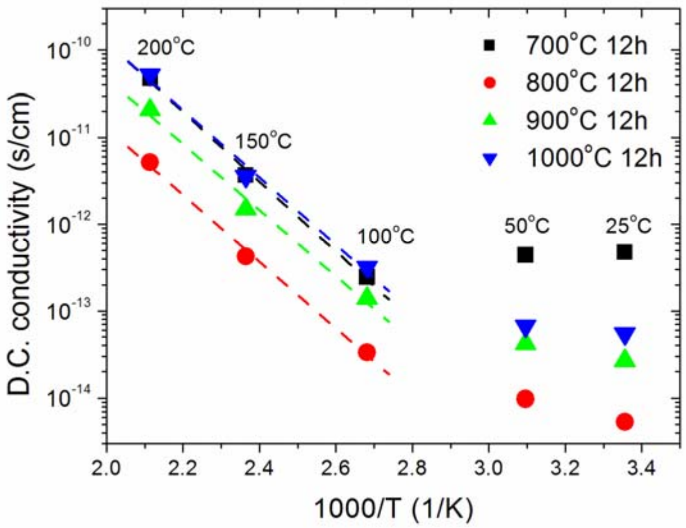

Fig. 10. Arrhenius plot of d.c. conductivity of TiO_2 samples sintered at various temperatures.

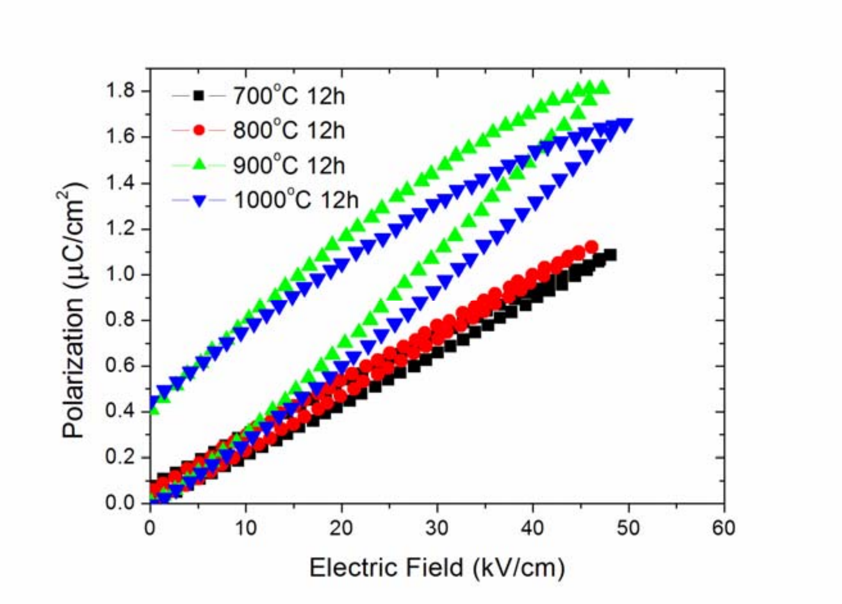

Fig. 11. Polarization vs. electric field relationship of TiO_2 samples sintered at various temperatures.

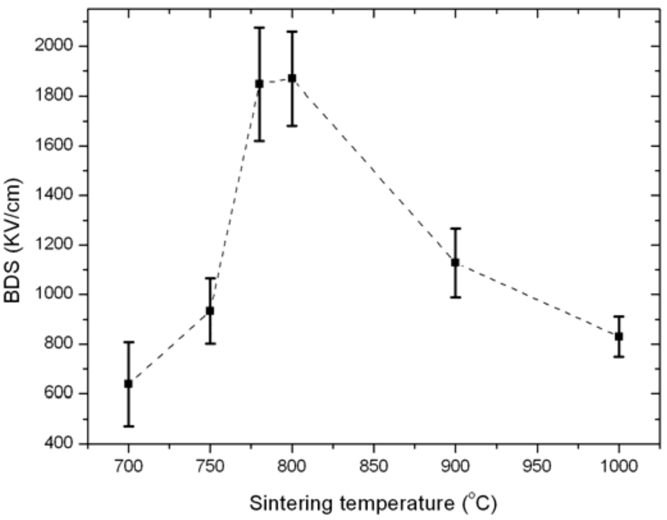

Fig. 12. Dielectric breakdown strength of TiO_2 samples as a function of sintering temperature.

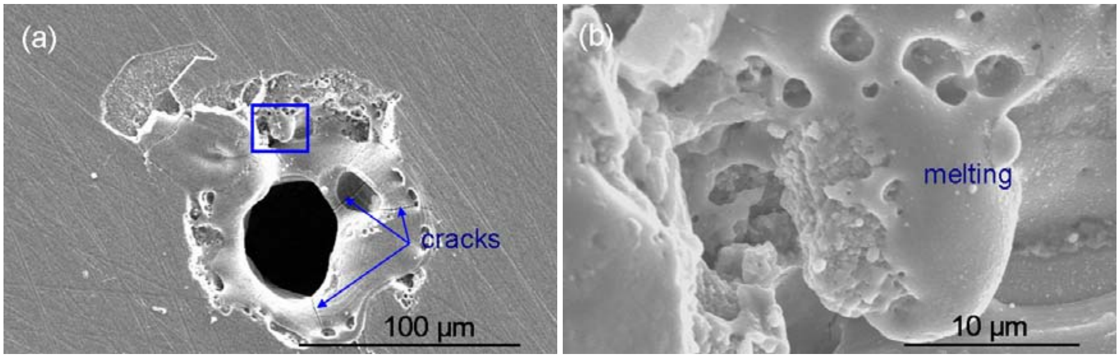

Fig. 13. (a) SEM micrographs showing a breakdown crater of a TiO_2 sample sintered at 800°C, and (b) an enlarged view of the section indicated in (a).

Tables:

Table 1. TiO_2 powder characteristics

Characteristics	Value
Purity (%)	99.9
Average particle size (nm)	40
Specific surface area (m^2/g)	38
Bulk density (g/cm^3)	0.20
True density (g/cm^3)	3.95
Crystal phase	80% anatase and 20% rutile

Table 2. Main impurities in the TiO_2 powder

Elements	Impurity level (wt %)
Fe	0.037
Mg	0.032
Ca	0.024
Al	0.0089

Table 3. Relationship between green compact density and sintering density

Green density (%)	Relative density after sintering at 800^{o}C (%)
36	82.3
41	89.3
48	96.2
60	98.3

Table 4. Fitting parameters of the impedance data measured at 550^{o}C

Samples	ρ_g (Ω·cm)	ρ_{gb} (Ω·cm)	ρ_{gb}/ρ_g	CPE1-P	CPE2-P
T8	3.96E5	9.86E6	24.9	0.97	0.73
T9	1.31E5	7.79E6	59.5	0.73	0.57
T10	8.21E4	4.35E7	530.3	0.68	0.43

2. COMPLEX IMPEDANCE STUDY OF FINE AND COARSE GRAIN TiO_2 CERAMICS

Sheng Chao, Vladimir Petrovsky and Fatih Dogan
Department of Materials Science and Engineering,
Missouri University of Science and Technology, Rolla MO 65409

Abstract

TiO_2 ceramics with various grain sizes were investigated by impedance spectroscopy techniques. Dielectric loss peak identified in coarse grain TiO_2 was attributed to space charge polarization occurring at the grain boundaries. Electric modulus representation of the impedance data showed two types of relaxation processes in coarse grain TiO_2, whereas only one type was observed in fine grain TiO_2. Long range migration of oxygen vacancies was found to be the dominant conduction mechanism for fine grain TiO_2, while electron hopping between localized states was attributed to dielectric relaxation in coarse grain TiO_2.

Ⅰ. Introduction

Recent studies showed that nanostructured TiO_2 ceramics possess significantly higher dielectric breakdown strength (BDS) than coarse grain TiO_2 ceramics, making them promising candidate materials for high energy density capacitor applications.[1] However, so far, it is still not clear of the reason for this improvement. Thus, a fundamental understanding of the different dielectric responses found in fine and coarse grain TiO_2 ceramics is of great importance. Complex impedance spectroscopy is a powerful technique to study electrical and dielectric properties of ceramics as it allows to distinguish the intrinsic (bulk) properties from extrinsic contributions associated with grain boundary, surface layer and electrode interfaces.[2] In addition, impedance analysis can give insight into relaxation mechanisms through various frequency/temperature dependent response characteristics.[3] In the present study, TiO_2 ceramics with various grain sizes were characterized by impedance spectroscopy within the frequency range of 1Hz to 1MHz and the temperature range of 25°C to 550°C. Impedance data were presented in a variety of forms to better elucidate the frequency/temperature dependent dielectric responses associated with the microstructural feature of the TiO_2 ceramics.

Ⅱ. Experimental Procedure

Commercially available TiO_2 powders (Nanophase Technologies Corporation) with an average particles size of 40nm were used to prepare pellets by uniaxially pressing at 50MPa followed by cold isostatic pressing at 300MPa. Sintering of the samples was conducted at 900°C for 1-24 hours in oxygen atmosphere. Relative densities of the sintered pellets were determined by Archimedes' method. Scanning electron microscopy (SEM, Hitachi S-4700) was employed for microstructural characterization. Impedance data were collected with a Solartron 1260 impedance analyzer and a Solartron 1296 dielectric interface followed by data processing using Zview software. Direct current (D.C.) conductivity measurements were performed with a Keithley 6517 Electrometer by using a two-probe method in dry air.

Ⅲ. Results and Discussion

SEM images of TiO_2 samples sintered at 900°C for various dwell times are given in Figure 1, which shows a gradual increase of grain size with the sintering time. The sintering densities of all samples were greater than 98%, thus the influence of porosity on the dielectric properties was neglected.

Figure 2 shows the frequency dependent spectra of loss tangent (tgδ) and loss factor (ε''). As the sintering time increases, a peak of loss tangent starts to be evident in low frequencies (~10Hz) (Figure 2a), which is attributed to the space charge polarization. The loss factor of TiO_2 sintered at 900^oC for 1h decreases almost linearly with increase of frequency, indicating that the dominate loss mechanism is conduction loss (Figure 2b). While for samples sintered for 24hrs a sign of loss peaks is observed as shown in Figure 2c and indicated by the arrow.

In considering that conduction losses may dominate the overall loss spectra at elevated temperatures, obscuring any possible relaxation processes; electric modulus presentation was adopted to reconstruct the impedance data and the results are shown in Figure 3. Electric modulus ($M^*=1/\varepsilon^*$) is the reciprocal of complex permittivity ($\varepsilon^*=\varepsilon'+i\varepsilon''$), which corresponds to the relaxation of electric field in the material when electric displacement remains constant.[4] Pronounced relaxation peaks were revealed in the spectra of imaginary component of electric modulus. With increased sintering time, each relaxation peak shows splitting marked as “1” and “2” in Figure 3d. The relaxation peaks “1” are present at the same frequency for all samples and independent of the sintering time. However, relaxation peaks “2” can only be clearly seen in TiO_2 sintered for 6h and longer, which shifted towards higher frequency region with an increasing magnitude as the sintering time increases. Comparison of the loss factor and electric modulus representation can be used to distinguish the localized dielectric relaxation processes from long-range conductivity.[5,6] In general, for a conduction process, relaxation peaks would only be observed in the imaginary component of electric modulus while absent in the corresponding loss factor spectra. On the contrary, for a dielectric relaxation process, the peaks can appear in both electric modulus and loss factor spectra. Therefore, relaxation peaks "1" are referred to the long-range migration of charge carriers for conduction, whereas the second relaxation process is attributed to jumping of charge carriers between localized states in the short-range for dielectric relaxation.

By determining the relaxation peak frequency (f), relaxation time τ, $\tau=(2\pi f)^{-1}$ was obtained and plotted in Figure. 4. Two different activation energies (E_a) were calculated according to the Arrhenius law $\tau=\tau_0 \exp(-E_a/KT)$, where τ_0 is the prefactor, K is the Boltzmann constant and T is the absolute temperature. Activation energies for relaxation peak "1" (E_{a1}) for all samples were ~1.10 eV, and the activation energies for relaxation peak "2" (E_{a2}) were ~0.50 eV. Activation energies in the range of 0.90 eV to 1.20 eV are typical for the migration of oxygen vacancies in nanocrystalline and microcrystalline TiO_2.[7] Figure 5 shows d.c. conductivity of the samples sintered for various times at 900°C. Calculated activation energies for d.c. conduction are in the range of 1.12 eV to 1.18 eV, which are close to the activation energies obtained from the first relaxation process. Thus, the relaxation process with an activation energy ~1.10 eV is attributed to the long range migration of oxygen vacancies for ionic conduction. Electron hopping mechanism is believed to be the origin of the second relaxation process with an activation energy ~0.50 eV. An activation energy ~0.30 eV was calculated for TiO_2 single crystals (anatase or rutile) based on electron hopping mechanism.[8] Higher activation energy obtained in this study may be attributed to a more effective electron entrapment due to higher defect concentrations.

Cole-cole plot of the complex impedance spectra measured at 550°C is shown in Figure 6. It was observed that with the increase of sintering time the real part of impedance decreases, which is consistent with the d.c. conductivity measurements. Another important feature is that the impedance of sample sintered for 1h shows a large semi-circle in the high frequencies with only a small depressed semi-circle at low frequencies. On the contrary, the impedance spectra of the samples sintered for 12hrs and 24hrs consist of two depressed semi-circles with a comparable magnitude. Based on the capacitance values, high and low frequency semi-circles are attributed to the bulk grain and the grain boundary response, respectively. All experimental data can be fitted well by two parallel resistor (R)-constant phase element (CPE) circuits connected in series. Using of CPE instead of pure capacitor is to account for the non-ideality of the dielectric relaxation for better fitting. Capacitance value was derived from formula suggested for CPE.[9,10] Bulk grain resistivity (ρ_1) and gain boundary resistivity (ρ_2) were also calculated according to the following equations[11]:

$$\rho_1 = R_1 \frac{A}{L} \tag{1}$$

$$\rho_2 = \frac{R_2 C_2}{R_1 C_1} \rho_1 \tag{2}$$

here, A is the electrode area and L is the sample thickness; C_1, C_2 and R_1, R_2 are the capacitance and resistance of bulk grain and grain boundary, respectively.

With the increase of sintering time, grain boundaries become the dominant resistant part instead of the bulk grains, as indicated by the increasing ratio of $R_2/(R_1+R_2)$ from 0.20 (1h) to 0.58 (12h) and 0.71 (24h). This change could be the primary reason for lower BDS in TiO_2 ceramics with coarser grains when larger proportion of the electric field was applied to the grain boundaries. Since the grain boundary thickness is in the range of a few nanometers, dielectric breakdown may be initiated along the grain boundaries at lower electrical fields. Accompanied with this change, it was also observed that the differences between and ρ_1 and ρ_2 increased. For 1h sintered sample $\rho_2/\rho_1=6.7$; for 12hrs sintered sample $\rho_2/\rho_1=34.7$ and for 24hrs sintered sample $\rho_2/\rho_1=43.9$. The increased difference between and ρ_1 and ρ_2 is believed to be the cause of the space charge polarization observed in the loss tangent spectra as charge carriers accumulated at the grain boundaries.

It should be noted that about 0.1% acceptor type impurities (Fe, Mg, Al, Ca) are present in the starting powders. Segregation of impurity ions at grain boundaries, creates a negatively charged grain boundary core due to the formation of negatively charged defects: $M_{Ti}^{'}$ or $M_{Ti}^{''}$ (M represents Fe, Mg, Al, Ca). It can be expected that with the increase of grain size, there is an increase of the impurity ion concentration at grain boundaries, caused by decreased grain boundary density. Since electrons are believed to be the dominant charge carries in TiO_2 ceramics, the formation of an electron depletion layer gave rise to the increased grain boundary resistivity. Hence, the physical origin of the space charge polarization and the change in grain and grain boundary resistivity is ascribed to the segregation of acceptor type impurities.

Ⅳ. Conclusions

TiO_2 ceramics with various grain sizes exhibited quite different dielectric responses. Impedance analysis revealed that due to the segregation of impurity ions there is an enlarged difference between grain boundary resistivity to bulk grain resistivity, which gave rise to the space charge polarization. Electric modulus study showed that electron hopping between localized states is evident for TiO_2 ceramics with relatively large grain sizes.

References

[1] Y. Ye, S. Z. Zhang, F. Dogan, E. Schamiloglu, J. Gaudet, P. Castro, M. Roybal, M. Joler, and C. Christodulou, "Influence of Nanocrystalline Grain Size on the Breakdown Strength of Ceramic Dielectrics," PPC-2003: 14th IEEE International Pulsed Power Conference, Dallas, TX, pp.719-722, (2003).

[2] M. Li, A. Feteira and D. C. Sinclair, "Origin of the High Permittivity in $(La_{0.4}Ba_{0.4}Ca_{0.2})(Mn_{0.4}Ti_{0.6})O_3$ Ceramics," *J. Appl. Phys.*, **98**, 84101, 6pp (2005).

[3] W. Li and R. W. Schwartz, "AC Conductivity Relaxation Processes in CaCu3Ti4O12 Ceramics: Grain Boundary and Domain Boundary Effects," *Appl. Phys. Lett.*, **89**, 242906, 3pp. (2006).

[4] P. B. Macedo, C. T. Moynihan and R. Bose, "The Role of Ionic Diffusion in Polarization in Vitreous Ionic Conductors," *Phys. Chem. Glasses*, **13**[6] 171-9 (1972).

[5] I. M. Hodge, M. D. Ingram, and A. R. West, "Impedance and Modulus Spectroscopy of Polycrystalline Solid Electrolytes," *J. Electroanal. Chem.*, **74**[2] 125-43, (1976).

[6] R. Gerhardt, “Impedance and Dielectric Spectroscopy Revisited: Distinguishing Localized Relaxation from Long-Range Conductivity,” *J. Phys. Chem. Solids*, **55**[12] 1491-1506 (1994).

[7] C. Demetry and X. Shi, “Grain Size-Dependent Electrical Properties of Rutile (TiO_2),” *Solid State Ionics*, **118**[3-4] 271-279 (1999).

[8] N. A. Deskins and M. Dupuis, “Electron transport via polaron hopping in bulk TiO2: A density functional theory characterization,” *Phys. Rev. B*, 75 195212 10pp (2007).

[9] J.R. Macdonald, Impedance Spectroscopy: Emphasizing Solid Materials and Systems, John Wiley & Sons, New York, (1987).

[10] T. Dittrich, J. Weidmann, F. Koch, I. Uhlendorf and I. Lauermann, “Temperature- and Oxygen Partial Pressure-Dependent Electrical Conductivity in Nanoporous Rutile and Anatase,” *Appl. Phys. Lett.*, **75**, 3980 3pp (1999).

[11] X. Guo and J. Maier, Grain Boundary Blocking Effect in Zirconia: A Schottky Barrier Analysis,” *J. Electrochem. Soc.*, **148**, E121-6 (2001).

Figures

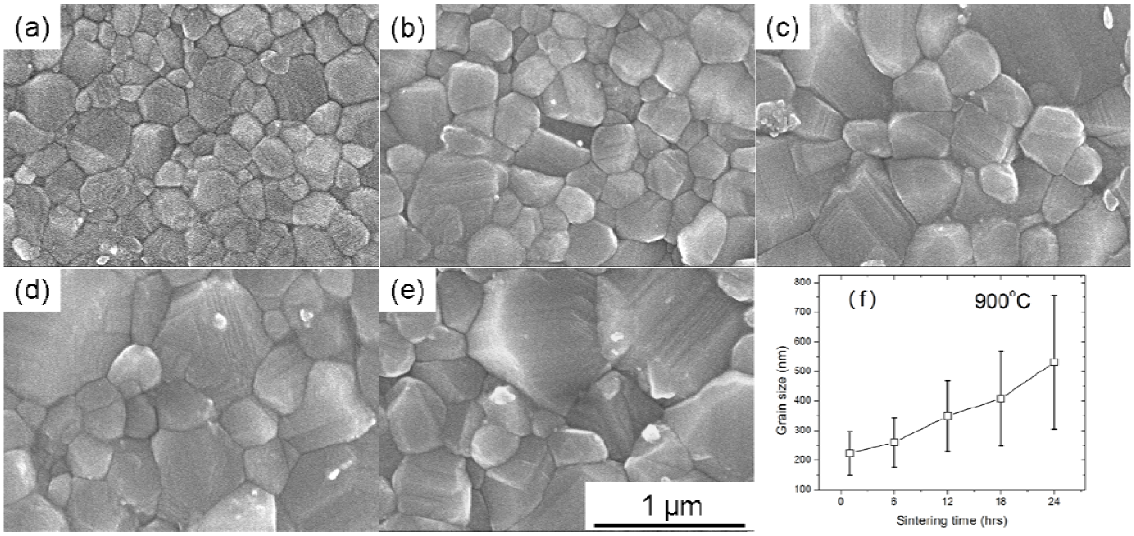

Fig. 1. SEM images of TiO_2 ceramics sintered at 900°C for (a) 1h, (b) 6h, (c) 12h, (d) 18h, (e) 24h and (f) grain size of TiO_2 sintered at various times.

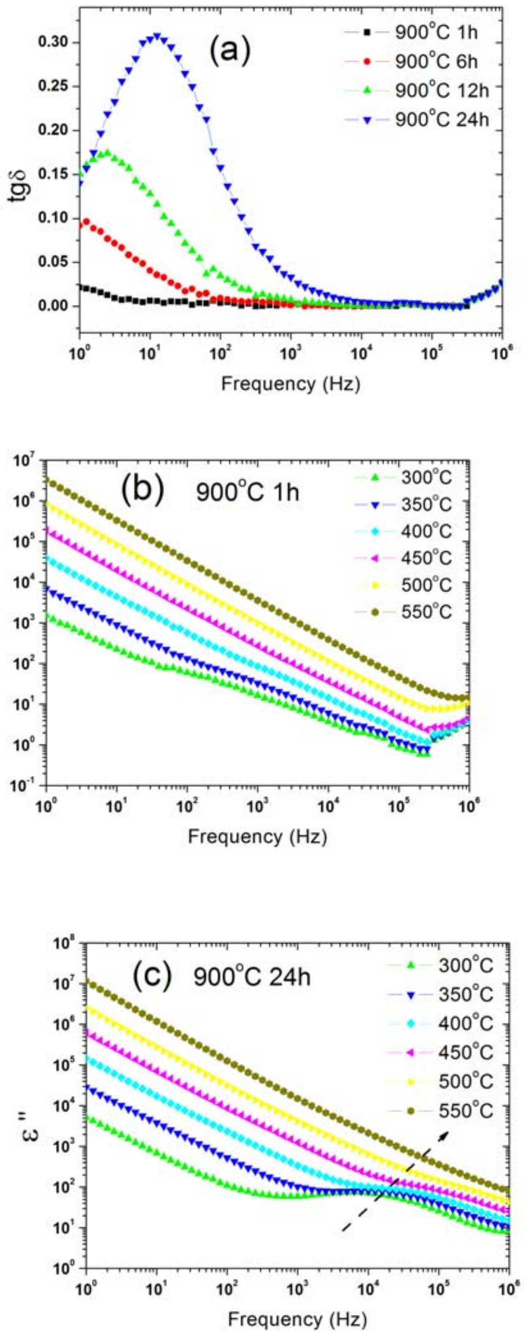

Fig. 2. (a) Room temperature loss tangent spectra of TiO_2 sintered at 900°C for various times; and loss factor spectra measured at various temperatures for TiO_2 sintered at 900°C for (b) 1h and (c) 24h.

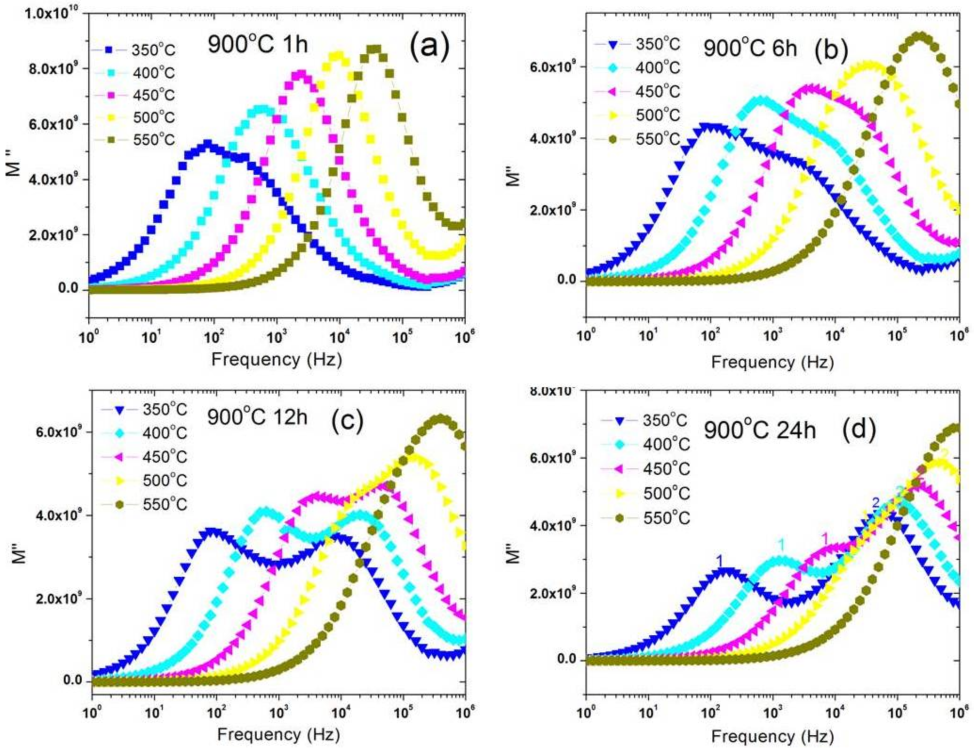

Fig. 3. Imaginary component of electric modulus spectra of TiO_2 sintered at 900°C for (a) 1h, (b) 6h, (c) 12h and (d) 24h.

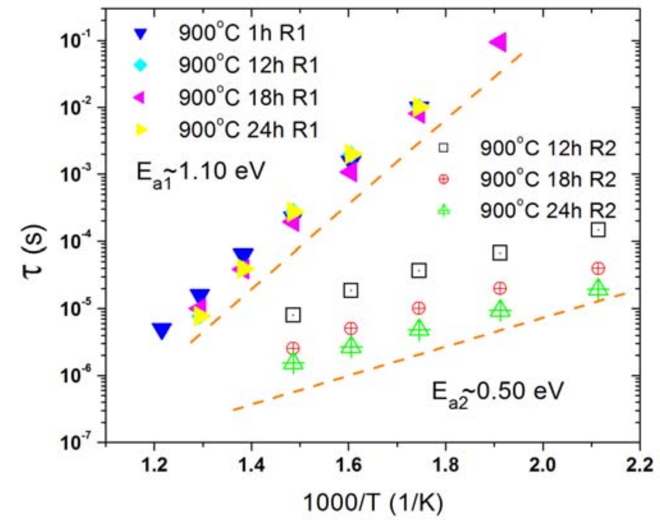

Fig. 4. Arrhenius plot of relaxation time for TiO_2 sintered at various times.

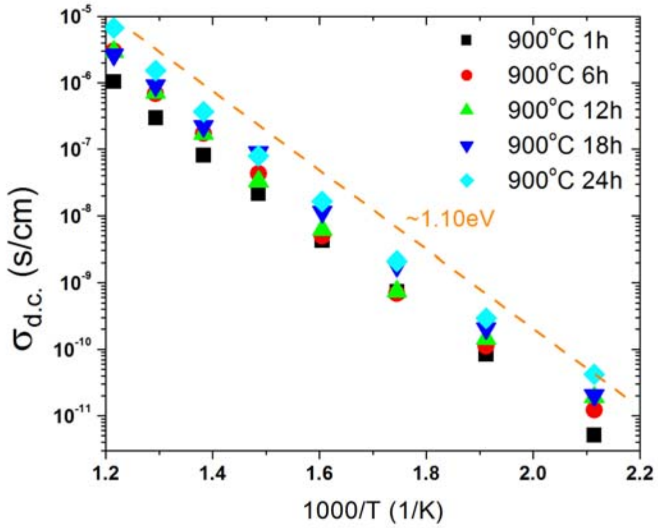

Fig. 5. Arrhenius plot of d.c. conductivity for TiO_2 sintered at various times.

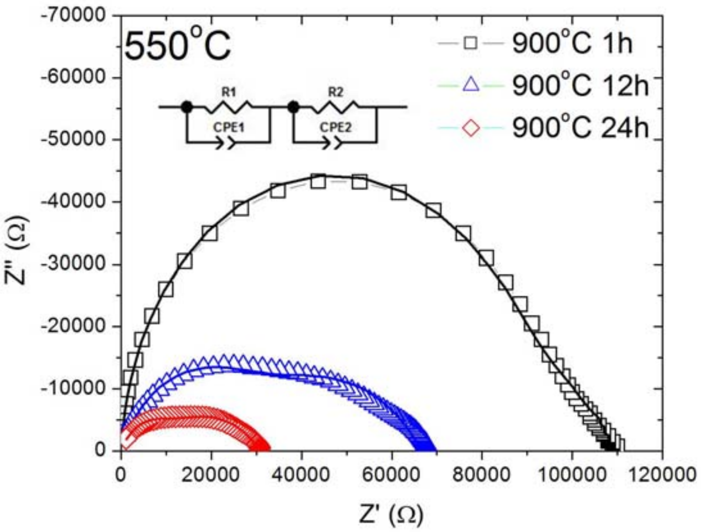

Fig. 6. Cole-cole plot of complex impedance spectra of TiO_2 measured at 550°C (open symbols: experimental data, solid lines: fitting data).

3. EFFECTS OF MANGANESE DOPING ON THE DIELECTRIC PROPERTIES OF TITANIUM DIOXIDE CERAMICS

Sheng Chao and Fatih Dogan

Department of Materials Science and Engineering,

Missouri University of Science and Technology, Rolla, MO 65409

Abstract

Dielectric properties of undoped and manganese (Mn) doped titanium dioxide (TiO_2) ceramics were measured by various test methods including impedance spectroscopy techniques. It was found that direct current (d.c.) conductivity and dielectric loss was effectively suppressed by small amount (~0.05 mol%) of Mn doping due to generation of possible electron traps. Further increase of Mn content led to formation of oxygen vacancies and increase of dielectric loss. Increased grain boundary resistivity was observed as Mn doping concentration increases, presumably due to Mn solutes segregation at the grain boundaries. Larger difference between the grain and grain boundary conductivity gave rise to space charge polarization. It was shown that TiO_2 ceramics with optimum amount of Mn doping concentration possess good dielectric properties that are suitable for energy storage applications.

Ⅰ. Introduction

The dielectric and electric properties of TiO_2 are quite sensitive to processing conditions such as oxygen partial pressure and temperature,[1] as well as the presence of intrinsic impurities and dopants.[2,3] The defect chemistry of non-stoichiometric TiO_2 has been investigated extensively.[4-6] Influence of various dopants such as Nb, Ta, Al, Ca, Y, Ba on properties of TiO_2 was studied by various research groups.[7-12] Most studies on Mn doping of TiO_2 are related to their ferromagnetic properties,[13,14] while little attention has been paid to the investigation of the dielectric properties of Mn doped TiO_2.

TiO_2 is considered as potential dielectric material for high energy density capacitor applications due to its relatively high dielectric constant (K: ~100, at room temperature) and high dielectric breakdown strength (BDS).[15] High insulation resistance, low dielectric loss and high BDS are essential material's properties for high energy density capacitors. These requirements were met through optimizing of processing parameters and incorporation of appropriate dopants at optimum concentrations. It has been well established that Mn doping is effective in achieving of high insulation resistance in $BaTiO_3$ based dielectrics,[16,17] In acceptor doped $BaTiO_3$, oxygen vacancies ($V_O^{\cdot\cdot}$) and ionized acceptors (Mn_{Ti}' and/or Mn_{Ti}'')are the dominant defects, which prevented the reduction of $BaTiO_3$ (in reduced $BaTiO_3$ oxygen vacancies and electrons are the dominant defects). In addition, it was also reported that dielectric loss (at 3 GHz) of TiO_2 ceramics was greatly reduced by introducing divalent or trivalent dopants with ionic radius in the range of 0.5-0.95 Å (ionic radius of Mn^{2+}: 0.64 Å), as the reduction of Ti^{4+} was prevented.[18] Hence, in the present study, effects of Mn doping on the dielectric properties of TiO_2 was investigated with respect to high energy density capacitor applications.

Ⅱ. Experimental Procedure

High purity (~99.99%) TiO_2 powders provided by TOHO Titanium Co. Ltd. (Japan) were used as starting materials. The powders are a mixture of about 7 % anatase and 93 % rutile phase with particle size ranging from 20-50nm as shown in Figure 1. Trace impurities of the powder (provided by the manufacturer) are listed in Table Ⅰ.

Manganese (II) acetate (tetrahydrate) (99.99%, Sigma-Aldrich) was used as Mn source for doping studies. A stock solution of Mn-precursor was prepared with high purity anhydrate ethanol (>99.5%, Sigma-Aldrich) as the solvent. TiO_2 powders were mixed with the stock solution at various dopant concentrations followed by ball milling of the slurry for 12hrs and dried under constant stirring. Dried powders were first uniaxially pressed in to pellets at a pressure of 50MPa followed by cold isostatic pressing at 300MPa. Green compacts were sintered at 900^{o}C for 2hrs in oxygen atmosphere.

Relative density of sintered samples was determined by Archimedes' method using water as immersion liquid, assuming theoretical density of 4.25g/cm^3 for rutile TiO_2. The microstructure of thermally etched (830^{o}C for 0.5h) surfaces and fractured surfaces were observed by scanning electron microscope (SEM, Hitachi S4700, Japan). Grain size of the sintered samples was determined by linear intercept method on SEM micrographs (at least 100 grains were counted). Phase evolution of undoped and Mn doped samples was determined by X-ray diffraction (XRD, Philips X'Pert, Holand).

For electrical property measurement, samples in size ~ 0.8 mm in thickness and 10 mm in diameter were polished and painted with silver paste as top and bottom electrodes, followed by heat treatment at 600^{o}C to ensure a good electrical contact. D.C. conductivity measurements were performed using Keithley 6517 Electrometer (Keithley Instruments, Cleveland, USA) by a two-probe method in ambient atmosphere. Dielectric constant of the samples was calculated according to the sample geometry and its capacitance measured using Solartron 1260 impedance analyzer connected with a Solartron 1296 dielectric interface (Solartron Analytical, Hampshire, England) in the frequency range 1 Hz to 1 MHz, with an a.c. voltage amplitude of 1V. Polarization-electric filed (P-E) relation was characterized on a ferroelectric testing system (RT6000, Radiant Technology, NM, USA). Pellets used for BDS test were further polished by 1 μm diamond paste to remove any possible surface flaws by maintaining of the sample thickness within 650 to 700 μm. For BDS measurements, D.C. voltage was supplied by Spellman SL30 high voltage generator (Spellman High Voltage Electronics Corporation, New York, USA), with a fixed ramp rate of 250V/second.

Ⅲ. Results and Discussion

XRD profile (Figure 2) shows that phase pure rutile TiO_2 was formed after firing for both undoped and Mn doped samples. According to previous investigation[13], Mn atoms can substitute Ti atoms up to a doping level of 5 mol%, without forming secondary phase. Microstructural development of TiO_2 ceramics with various amounts of Mn content are shown in Figure 3. Sintering density of the samples were > 99% th.d. measured by Archimedes's method. No significant influence of Mn doping on grain size was observed (Table Ⅱ). Hence, the effects of grain size on the dielectric properties of TiO_2 were not considered in this study. Fracture surfaces of undoped, 0.05 and Mn 0.10 mol% Mn-doped TiO_2 are shown in Figure 4. A gradual change of the fracture mode from intergranular to transgranular fracture is observed as the concentration of Mn-doping increases. This transition of fracture mode is believed to be related to the change of grain boundary bonding strength, resulted from an increase of Mn concentration at the grain boundaries.

Dielectric constant, loss tangent, d.c. conductivity and BDS that are critical parameters for energy storage capability of dielectrics were measured. Data were collected from 25^{o}C to 200^{o}C with exception of BDS which was only measured at room temperature. Frequency dependence of dielectric constant of selected samples (undoped and doped with 0.05, 0.07, 0.10, and 0.20 mol% Mn) are shown in Figure 5. It was observed that except for TiO_2 doped with 0.20 mol% of Mn, all the other samples demonstrated a non-dispersive dielectric constant around 130 at room temperature over the entire frequency range scanned. High apparent dielectric constant found in low frequencies of 0.20 mol% Mn doped TiO_2 is attributed to the influence of space charge polarization that is discussed later in more detail. All samples except TiO_2 doped with 0.05 mol% Mn showed higher dielectric constant in low frequency region at 200^{o}C compared to data obtained by room temperature measurements. However, at higher frequencies (>1 kHz), the dielectric constant measured at 200^{o}C is similar to that obtained at room temperature, because high frequency region is less susceptible to the influence of d.c. conductivity. Figure 5 (c) shows a gradual decrease of dielectric constant (1 kHz) as the temperature increases. From 25^{o}C to 200^{o}C, a roughly 11% decrease of dielectric constant was observed for TiO_2 with Mn content equal and less than 0.10 mol%. For TiO_2 doped with 0.20 mol% of Mn, higher dielectric constant measured at high temperatures was again attributed to the influence of significantly increased d.c. conductivity. As it will be discussed in the next section, excessive Mn doping leads to a significant increase of d.c. conductivity.

The frequency dependence of loss tangent measured at various temperatures is shown in Figure 6. At room temperature, a pronounced loss peak developed in TiO_2 doped with 0.20 mol% of Mn. Frequency interval of the loss peak is similar to that observed for dielectric constant, which is typical for one type of polarization mechanism starting to damp out as it can no longer keep up with the stimulus frequency.[19] Depending on the frequency region and the material, this polarization mechanism is ascribed to space charge polarization. Further proof of this assumption will be provided by impedance spectroscopy analysis. As the temperature increases, the loss peak shifts to higher frequency regions, indicating a thermally stimulated process. At higher temperatures, dielectric loss of all samples increases significantly in low frequency region due to increased d.c. conductivity. However, the dielectric loss of TiO_2 doped with 0.05 mol% of Mn is substantially lower than other samples while the dielectric loss of TiO_2 doped with 0.20 mol% is significantly higher.

To investigate the relaxation process (loss peak) in TiO_2 doped with 0.20 mol% of Mn, electric modulus was introduced to suppress the influence of high loss caused by d.c. conductivity that may obscure the actual relaxation process.[20] The electric modulus is the reciprocal of complex permittivity, which corresponds to the relaxation of electric field in the material when electric displacement remains constant. Therefore, the electric modulus represents the real dielectric relaxation process.[21] The definition of electric modulus is given by the following equations:

$$M^*_{(\omega)} = \frac{1}{\varepsilon^*} = M'_{(\omega)} + iM''_{(\omega)} \qquad (1)$$

$$M'_{(\omega)} = \frac{\varepsilon'_{(\omega)}}{\varepsilon'^{2}_{(\omega)} + \varepsilon''^{2}_{(\omega)}} \qquad (2)$$

$$M''_{(\omega)} = \frac{\varepsilon''_{(\omega)}}{\varepsilon'^{2}_{(\omega)} + \varepsilon''^{2}_{(\omega)}} \qquad (3)$$

Here, $M^{*}_{(\omega)}$, $M'_{(\omega)}$ and $M''_{(\omega)}$ are complex, real and imaginary electric modulus, respectively; while $\varepsilon^{*}_{(\omega)}$, $\varepsilon'_{(\omega)}$ and $\varepsilon''_{(\omega)}$ are complex, real and imaginary permittivity, respectively. The frequency dependency of imaginary component of electric modulus of TiO_2 doped with 0.20 mol% of Mn is shown in Figure 6 (d) which clearly reveals the presence of relaxation peaks. These peaks were difficult to identify in loss tangent spectra measured at high temperatures due to the high conduction losses as depicted in Figure 6. (c). Relaxation peaks shift towards higher frequencies as the temperature increases, indicating a decrease of relaxation time with increasing temperature. By determining the frequency (f) at which M'' peak occurs, the angular frequency (ω, $\omega=2\pi f$) was calculated. It follows the Arrhenius law ($\omega=\omega_0\exp(-E_a/KT)$) as shown in Figure 7, where E_a is the activation energy and K is the Boltzmann constant. The activation energy calculated by best linear fitting of the data is 0.33 eV that is a typical value for the electron-hopping energy.[22]

D.C. conductivity as a function of the temperature is presented in Arrhenius plot (Figure 8). It was observed that with small amount of Mn doping (up to 0.05 mol%) there is a substantial decrease of d.c. conductivity. Reduction of the conductivity is of critical importance for successful application of dielectric materials in high energy density capacitors, since conductivity is closely related to dielectric breakdown phenomenon and dielectric loss (particularly at low frequencies). A decrease in conductivity by small amount of Mn doping is attributed to creation of electron traps, which can be expressed by the following equations:

$$Mn_{Ti}^{X} + e^{'} \leftrightarrow Mn_{Ti}^{'} \quad (4)$$

$$Mn_{Ti}^{'} + e^{'} \leftrightarrow Mn_{Ti}^{''} \quad (5)$$

$$MnO \rightarrow Mn_{Ti}^{''} + V_{O}^{\bullet\bullet} + O_{O}^{X} \quad (6)$$

Formation of electron traps were attributed to the fact that Mn^{4+} and Mn^{3+} have higher tendency for reduction in comparison to Ti^{4+} while similar effects were observed in $BaTiO_3$ ceramics.[23] Further increase of Mn concentration leads to the formation of large amount of oxygen vacancies according to Equation 6; as a result, conductivity increases when Mn content is higher than 0.07 mol%. Hence, optimum concentration of Mn doping was found to be around 0.05 mol%. As discussed above, at this particular Mn concentration the loss tangent was the lowest among other samples with various amounts of Mn dopants.

BDS of undoped and 0.05 mol% Mn doped TiO_2 was measured at room temperature. Based on the results of eight samples, average values of 423±83 kV/cm and 531±59 kV/cm were obtained for undoped and 0.05 mol% Mn doped TiO_2, respectively. Thus, there is a 25% increase of BDS with optimized amount Mn doping which is equivalent to ~56% increase in energy density for a linear dielectric governed by the following equation:

$$W_{(vol.)} = \frac{1}{2}\varepsilon_0 \varepsilon_r E_b^2 \quad (7)$$

where ε_0 is the permittivity of vacuum (8.854×10^{-12} F/m), ε_r is the dielectric constant and E_b (V/m) is BDS. It should be noted that BDS values were obtained using samples with a thickness ranging from 650 to 700μm, which is much thicker than dielectric layer thickness in multi-layer ceramic capacitors (MLCCs) normally ranging from several to tens of micrometers. Much higher BDS and consequently much higher energy density can be expected if sample thickness is reduced to actual dielectric thickness in MLCCs. An increase in the sample thickness can lead to a substantial decrease in BDS due to the well-known weakest chain theory since the thicker the sample the higher is the possibility of the presence of defects that can intrigue dielectric breakdown.[24] It was reported that just by reducing the dielectric layer thickness from 910μm to 50μm, BDS increased from 117 to 764 kV/cm for 0.7 $BaTiO_3$-0.3 $BiScO_3$ ceramics.[25]

In consideration of reduced dielectric loss, much more improvement in energy storage and energy storage efficiency (energy storage efficiency is defined as the ratio of retractable energy upon discharge to total energy stored) can be achieved in TiO_2 doped with 0.05mol% Mn. The energy storage efficiency can be calculated from the polarization-electric field relationship depicted in Figure 9. The energy loss (energy stored subtracted by retractable energy) is represented by the area encircled in the charge and discharge curve. At room temperature, the energy storage efficiency of undoped TiO_2 is 93.6%, while the energy storage efficiency of 0.05 mol% Mn-doped TiO_2 is 98.5%. This difference greatly increased at 200°C, with energy storage efficiency of 35.5% and 96.7% for undoped and 0.05 mol% Mn-doped TiO_2, respectively. Significantly reduced energy storage efficiency of undoped TiO_2 at 200°C is attributed to its high conductivity.

On the contrary, 0.05 mol% Mn-doped TiO_2 shows the potential to be applicable at 200°C as it still maintains a high efficiency.

Complex impedance measurements were conducted, as this technique allows distinguishing the intrinsic (bulk) properties from extrinsic contributions such as grain boundaries, surface layers, and electrode contact problems.[26] Interpretation of impedance data is based on the brick layer model of polycrystalline ceramics. In this model, relative conductive cubic shaped grain cores (d: grain size) are surrounded by more resistive grain boundaries (δ: grain boundary thickness). Only the series path via grain cores and capping grain boundaries is considered, while the parallel grain boundary path is ignored. In the absence of any precipitates or electrode polarization effects, there are only two parallel RC (Resistor-Capacitor) circuits connected in series representing the grain core and grain boundaries response[27].

An example of complex impedance spectra measured at 550°C of TiO_2 doped with various amount of Mn is shown in Figure 10. For TiO_2 ceramics with Mn doping level equal or less than 0.05 mol%, there was only one semi-circle representing the bulk grain response (determined by the capacitance value). However, when the doping level reaches 0.07 mol% and higher, two semi-circles were observed. The second semi-circle found at low frequencies was attributed to the contribution of grain boundaries. Experimental data can be well fitted (<5% error) by either one CPE (constant phase element)-R parallel circuit or two CPE-R parallel circuits connected in series. Here CPE instead of pure capacitor was used for the fitting of experimental data in order to account for the non-ideality of the relaxation process.[12] The gradual development of grain boundary response was caused by increased grain boundary resistivity, which resulted in a grain boundary blocking effect. As Mn concentration increases, because of the elastic strain-energy driving force and electro-static driving force,[10] more Mn ions are expected to segregate to the grain boundaries. In a similar system, Mn segregation at the grain boundaries was believed to be the cause of enhanced positive-temperature-coefficient effect in $BaTiO_3$.[28] As a result, negatively charged defects (Mn_{Ti}' or Mn_{Ti}'') created a negatively charged grain boundary core as significant amount of segregated Mn^{3+} or Mn^{2+} replaces Ti^{4+} sites, which was balanced by positive space charge layer in the nearby depletion region for electrons, forming a back-to-back Scotty barrier.[12,29]

Detailed impedance analysis was based on the fitting of the experimental data. The grain core resistance (R_1) and grain boundary resistance (R_2) were directly obtained from fitting results. Grain core and grain boundary capacitance (C_1 and C_2) was determined by the following formulation:

$$C = (R^{1-n}Q)^{1/n} \tag{8}$$

where the value of Q and n were obtained from fitting results of CPE element. And n is a measure of the deviation from ideal capacitor behavior (ideal capacitor behavior when n=1). Grain and grain boundary resistivity (ρ_1, ρ_2) were calculated by the following relations:

$$\rho_1 = R_1 \frac{A}{L} \tag{9}$$

$$\tau_1 = R_1 C_1 = \varepsilon_1 \rho_1 \tag{10}$$

$$\tau_2 = R_2 C_2 = \varepsilon_2 \rho_2 \tag{11}$$

$$\varepsilon_1 = \varepsilon_2 \tag{12}$$

$$\rho_2 = \frac{R_2 C_2}{R_1 C_1} \rho_1 \qquad (13)$$

where A is the electrode area and L is the sample thickness; τ_1 and τ_2 are the relaxation time of grain core and grain boundary respectively; and ε_1 and ε_2 are the dielectric constant of grain core and grain boundary, respectively. The feasibility of assuming equal value of ε_1 and ε_2 has been validated by other researchers.[29] Sample data extracted at 550°C is listed in Table III and the same approach was used to extracted data measured at other temperatures.

It was found that for grain core the n values (n_1) are all close to one, independent of the Mn doping concentration, while for grain boundary, the n values (n_2) are much less than one and decreases with the increasing of Mn concentration. It is believed that the value of n is associated with the geometrical or chemical inhomogenity.[30] Close to ideal capacitor behavior of grain core response indicates a uniform distribution of dopants inside of the grains. However, a large deviation from ideal capacitor behavior (depressed semi-circle) was observed for the grain boundary response, suggesting that there is some degree of nonuniformity along the grain boundaries. Enhanced grain boundary misorientation as a result of non-homogeneous distribution of Mn dopants accumulated at the grain boundaries is believed to be the cause of this phenomenon. Similar behavior was also observed in yttrium doped TiO_2.[12] Only a small variation of grain core capacitance (C_1) was observed for TiO_2 with different amounts of Mn, and the values are in good agreement with the dielectric constant of TiO_2. On the other hand, an increase of the grain boundary capacitance (C_2) was found as Mn concentration increases, which may be attributed to reduced grain boundary layer (space charge layer) thickness.[31] In addition, dipolar relaxation occurring at the grain boundaries might also contribute this result.

From Table Ⅲ it can be seen that there is more than two orders of magnitude difference between grain core and grain boundary resistivity for TiO_2 doped with more than 0.07 mol% of Mn. This difference becomes greater as Mn concentration increases (from 174 for 0.07 mol% Mn to 757 for 0.20 mol% Mn). Due to this discontinuity of resistivity at the grain and grain boundary interface, space charge polarization occurs when charge carriers are piled up at the grain boundaries. Therefore, the space charge polarization identified in the loss tangent spectra (Figure 6) can be satisfactory explained.

Grain core and grain boundary conductivity were plotted in Arrhenius relation shown in Figure 11. It can be seen that the grain core conductivity differs greatly with various amounts of Mn-doping, especially at low temperatures. Higher concentration of mobile oxygen vacancies created by Mn doping is believed to be the cause of this phenomenon. At higher temperatures, more oxygen vacancies are generated by thermal energy, resulting in a less difference of conductivity. The activation energy for electrical conductivity was determined by using Arrhenius equation ($\sigma=\sigma_0\exp(-E_a/KT)$), where σ is conductivity. A sharp decrease of activation energy was observed for grain core conductivity with the increase of Mn concentration (from 1.70eV for undoped to 0.85eV for 0.20 mol% Mn doped), which is attributed to the presence of acceptor status in the band gap.[12] Variations in the activation energy for grain boundary conductivity were much less. With increasing Mn concentration, only a slight increase (from 1.19eV to 1.28eV) of the activation was observed. This behavior is in consistent with the study of yttrium doped TiO_2.[12] Further investigation on the conduction mechanism is necessary to clarify to variation of conductivity and activation of both grain core and grain boundaries.

Ⅳ. Conclusions

The influence of Mn doping on the dielectric properties of TiO_2 was studied. An optimized doping concentration of 0.05 mol% was identified, resulting in reduced conductivity and loss tangent as well as improved BDS and energy storage capability. It was found that small amounts of Mn doping leads to generation of electron traps resulting in enhanced dielectric properties. Higher amounts of Mn doping generate mobile oxygen vacancies resulting in higher loss factor. Impedance analysis revealed that with the increase of Mn doping concentration, the difference between grain and grain boundary conductivity enlarged, presumably due to excess Mn solutes segreatating at the grain boundaries, which gave rise to a grain boundary blocking effect and space charge polarization.

Acknowledgments

The authors would like to thank Dr. Robert Schwartz (Missouri University of Science and Technology) for his thoughtful discussion and correction of the manuscript.

References

[1] A. J. Moulson, J.M. Herbert, “Electroceramics,” Chapman and Hall, London, (1990).

[2] J. F. Baumard, D. Panis and A.M. Anthony, “A study of Ti-O system Between Ti_3O_5 and TiO_2 at High Temperature by Means of Electrical Resistivity,” *J. Solid State Chem.,* **20** [1] 43-51 (1977).

[3] J. F. Baumard and E. Tani, “Electrical Conductivity and Charge Compensation in Nb Doped TiO_2 Rutile,” *J. Chem. Phys.*, **67** [3] 857 4pp. (1977).

[4] F. Millot, M.G. Blanchin, R. Tetot, J.F. Marucco, B. Poumellec, C. Picard and B. Touzelin, “High Temperature Nonstoichiometric Rutile TiO_{2-x},” *Prog. Solid State Chem.*, **17 [4]** 263-293 (1987).

[5] U. Balachandran and N.G. Eror, “Electrical Conductivity in Non-stoichiometric Titanium Dioxide at Elevated Temperatures,” *J. Mater. Sci.*, **23** [8] 2676-2682 (1988).

[6] T. Bak, J. Nowotny, M. Rekas and C.C. Sorrell, “Defect Chemistry and Semiconducting Properties of Titanium Dioxide: I. Intrinsic Electronic Equilibrium,” *J. Phys. Chem. Solids.,* **64** [7] 1043-1056 (2003).

[7] W. Y. Wang, D. F. Zhang, T. Xu, L.F. Li, T. Zhou and X. L. Chen, “Nonlinear Electrical Behavior and Dielectric Properties of (Ca, Ta)-doped TiO_2 Ceramics,” *J. Alloys Compd.*, **335** [1-2] 210-215 (2002).

[8] R. Guo, Y. Jiang and A. S. Bhalla, “Processing and Annealing Conditions on the Dielectric Properties of $(Ta_2O_5)_{0.92}(TiO_2)_{0.08}$ ceramics,” *Mater. Lett.*, **57** 270-274 [2] (2002).

[9] M. A. McCormick and E.B. Slamovich, “Microstructure Development and Dielectric Properties of Hydrothermal $BaTiO_3$ Thin Films,” *J. Eur. Ceram. Soc.*, **23** [12] 2143-2152 (2003).

[10] J. A. S. Ikeda and Y.-M. Chiang, “Space Charge Segregation at Grain Boundaries in Titanium Dioxide: I, Relationship between Lattice Defect Chemistry and Space Charge Potential,” *J. Am. Ceram. Soc.*, **76** [10] 2437-2446 (1993).

[11]Q. Wang, G. D. Lian and E. C. Dickey, "Grain Boundary Segregation in Yttrium-doped Polycrystalline TiO_2," *Acta Mate.*, **52** [4] 809-820 (2004).

[12]Q. L. Wang, O. Varghese, C. A. Grimes and E. C. Dickey, "Grain Boundary Blocking and Segregation Effects in Yttrium-doped Polycrystalline Titanium Dioxide," *Solid State Ionics.*, **178** [3-4], 187-194 (2007).

[13]N. H. Hong, J. Sakai, A. Ruyter and V. Brizé, "Does Mn Doping Play Any Key Role in Tailoring the Ferromeganetic Ordering of TiO2 Thin Films," *App. Phys. Lett.*, **89** 252504 3pp. (2006).

[14]K. J. Kim, Y. R. Park, J. H. Lee, S.-L. Choi, H. J. Lee, C. S. Kim and J. Y. Park "Room-temperature Ferromagnetic Properties in Mn-doped Rutile $TiO_{2-\delta}$ Thin Films," J. Magn. Mag. Mater. **316** e215-e218 (2007).

[15]S. Chao and F. Dogan, "Sintering and Dielectric Properties of Nanostructured High Purity Titanium Dioxide," *Ceramic Transactions (Advances in Energy Materials),* **205** 23-30 (2009).

[16]D. W. Hahna and Y. H. Han, "Quantitative Analysis of Oxidation–Reduction Behavior of Mn-doped $BaTiO_3$," *Ceram. Inter.*, **34** [5] 1341-1344 (2008).

[17]Y. Takezawa, K. Kobayashi, F. Nakasone, T. Suzuki, Y. Mizuno and H. Imai, "Mn-Doped $BaTiO_3$ Thin Film Sintered Using Nanocrystals and Its Dielectric Properties," *J. J. of App. Phys.*, **48** [11] 111408 5pp. (2009).

[18]A. Templeton, X. Wang, S. J. Penn, S. J. Webb, L. F. Cohen and N. M. Alford, "Microwave Dielectric Loss of Titanium Oxide," *J. Am. Ceram. Soc.*, **83**[1] 95-100 (2000).

[19]K. C. Kao, "Dielectric Phenomena in Solids," Elsevier Academic Press (2004).

[20]K. L. Ngai, S. W. Martin, "Correlation between the Activation Enthalpy and Kohlrausch Exponent for Ionic Conductivity in Oxide Glasses," *Phys. Rev. B.*, **40** 10550-10556 (1989).

[21]M. Tomozawa1, J. Cordaro1 and M. Singh, "Low Frequency Dielectric Relaxation From Complex Impedance and Complex Electric 'Modulus' ,"*J. Mater. Sci.*, **14** [8] 1945-1951 (1979).

[22]H. L. Tuller and A. S. Nowick, "Small Polaron Electron Transport in Reduced CeO_2 Single Crystals," *J. Phys. Chem. Solids.*， **38** [8] 859-867 (1977).

[23] H.-J. Hagemann, and D. Hennings, "Reversible Weight Change of Acceptor-doped $BaTiO_3$," *J. Am. Ceram. Soc.*, **64** [10] 590-594 (1981).

[24]R. Gerson and T. C. Marshall, "Dielectric Breakdown of Porous Ceramics," *J. Appl. Phys.*, **30** 1650 4pp. (1959).

[25]H. Ogihara, C. A. Randall and S. Trolier-McKinstry, "High-Energy Density Capacitors Utilizing 0.7 $BaTiO_3$–0.3 $BiScO_3$ Ceramics," *J. Am. Ceram. Soc.*, **92** [8], 1719-1724 (2009).

[26]M. Li, A. Feteira and D. C. Sinclair, "Origin of the High Permittivity in $(La_{0.4}Ba_{0.4}Ca_{0.2})(Mn_{0.4}Ti_{0.6})O_3$ Ceramics," *J. Appl. Phys.*, **98**, 84101 6pp. (2005).

[27]N. J. Kidner, N. H. Perry and T. O. Mason, "The Brick Layer Model Revisited: Introducing the Nano-Grain Composite Model," *J. Am. Ceram. Soc.*, **91** [6] 1733-1746 (2008).

[28]W. Heywang, "Barium Titanate As Semiconductor With Blocking Layers," Solid State Electron. **3** 51–58 (1961).

[29]X. Guo and J. Maier, “Grain Boundary Blocking Effect in Zirconia: A Schottky Barrier Analysis,”*J. Electrochem. Soc.*, **148** [3] 121-126 (2001).

[30]T. Watanabe, T. Murakami and S. Karashima, “Misorientation Dependence of Grain Boundary Segregation,” *Scripta Met.*, **12** [4] 361-365 (1978).

[31]M. Vollman and R.Waser, “Grain Boundary Defect Chemistry of Acceptor-Doped Titanates: Space Charge Layer Width,” *J. Am. Ceram. Soc.*, **77** [1] 235-243 (1994).

Figures

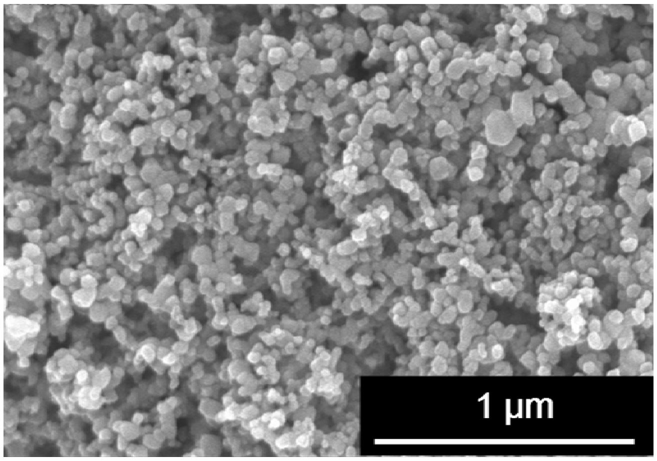

Fig. 1. SEM image of TiO_2 starting powders.

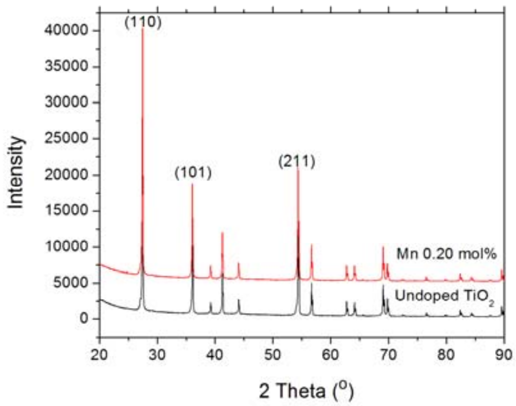

Fig. 2. XRD profile of undoped and Mn 0.20 mol% doped TiO_2 ceramics

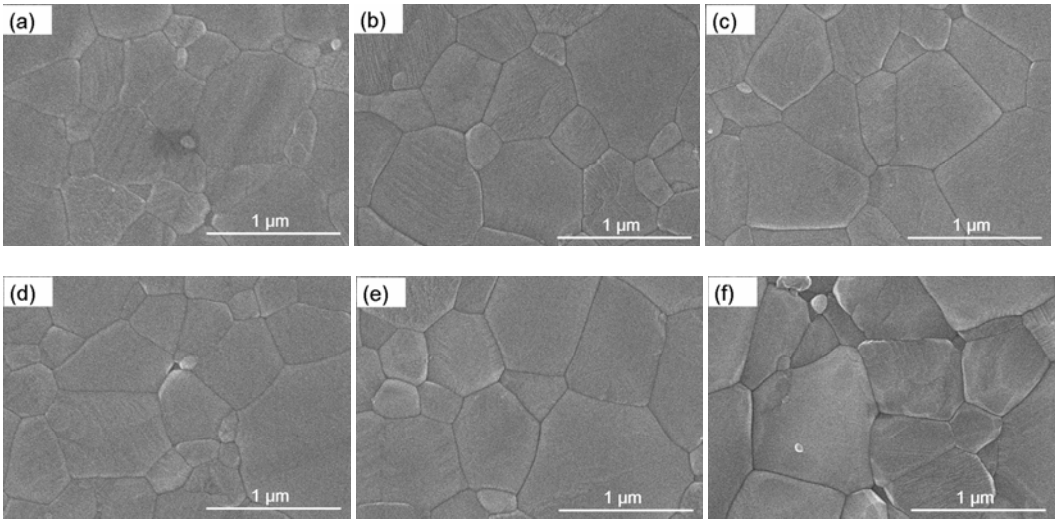

Fig. 3. SEM images of thermal etched surface of TiO_2 with various amounts of Mn content (a) undoped; (b) 0.03mol%; (c) 0.05mol%, (d) 0.07mol%; (e) 0.10mol%; (f) 0.20mol%.

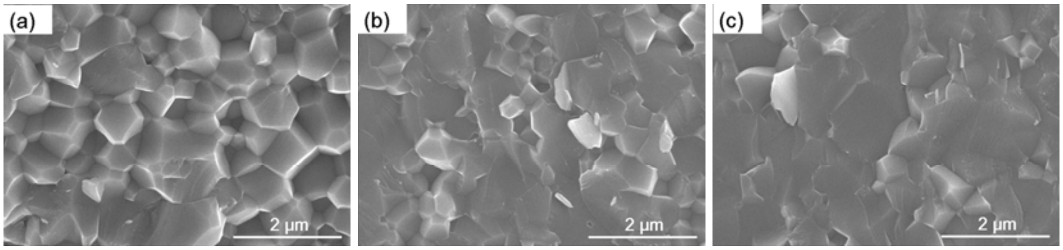

Fig. 4. SEM images of the fracture surface of TiO_2 with various amounts of Mn content (a) undoped; (b) 0.05mol%; (c) 0.10mol%.

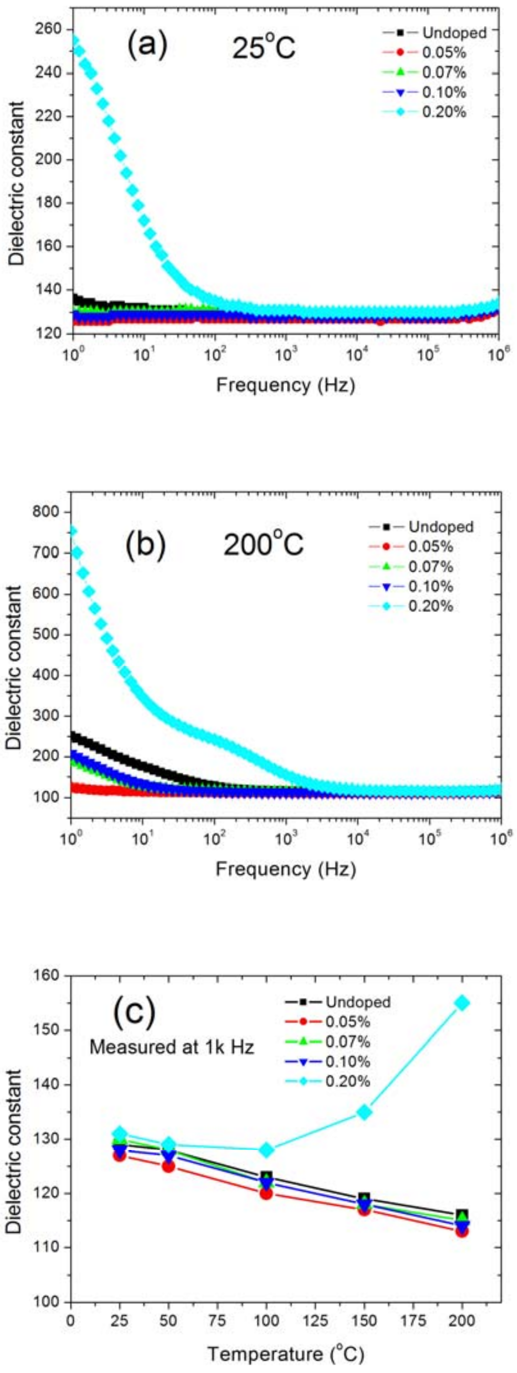

Fig. 5. Frequency dependence of dielectric constant with various amounts of Mn doping measured at (a) 25°C and (b) 200°C (c) Temperature dependent dielectric constant at 1 kHz.

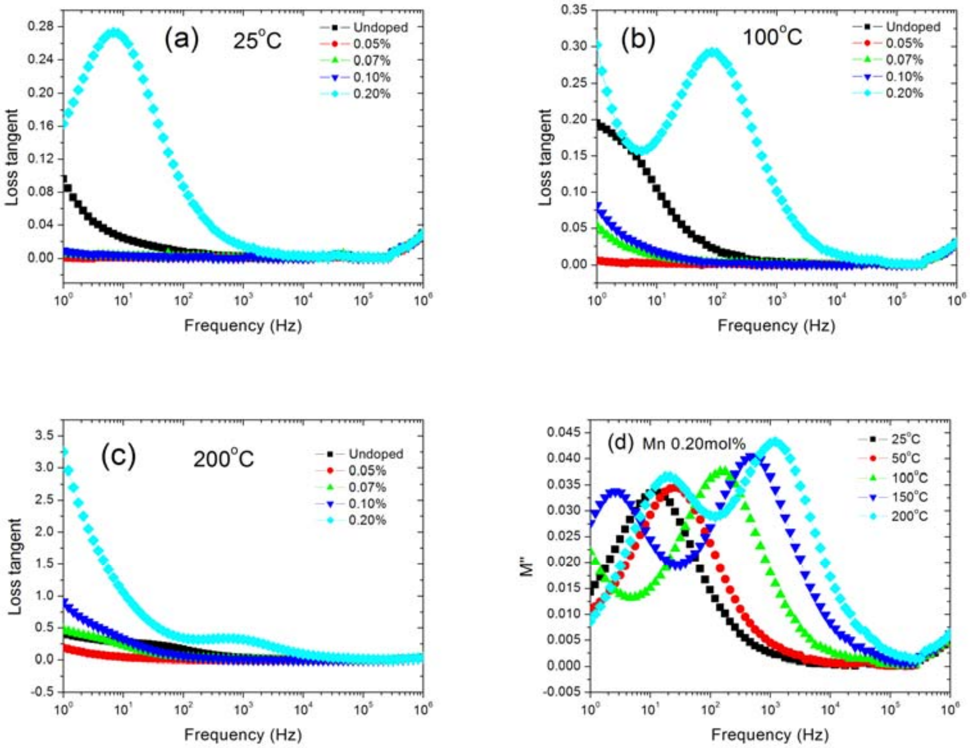

Fig. 6. Frequency dependence of loss tangent of TiO_2 with various amounts of Mn content measured at (a) 25°C; (b) 100°C and (c) 200°C. (d) Frequency dependency of electric modulus of TiO_2 doped with 0.20 mol% Mn measured at various temperatures.

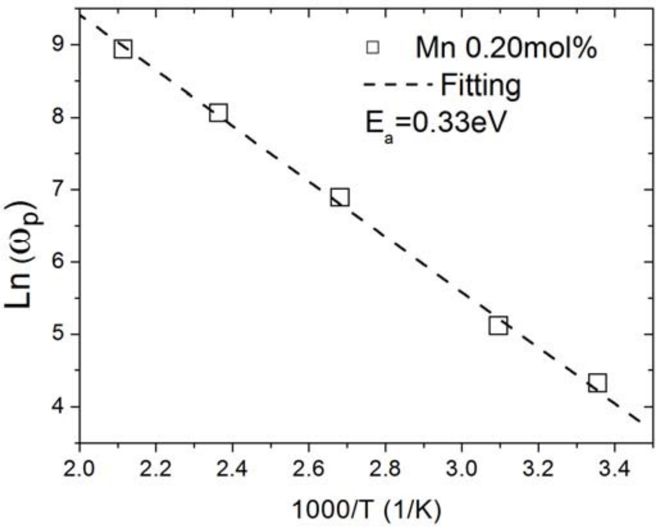

Fig. 7. Arrhenius plot of angular frequency of TiO_2 doped with 0.20 mol% Mn.

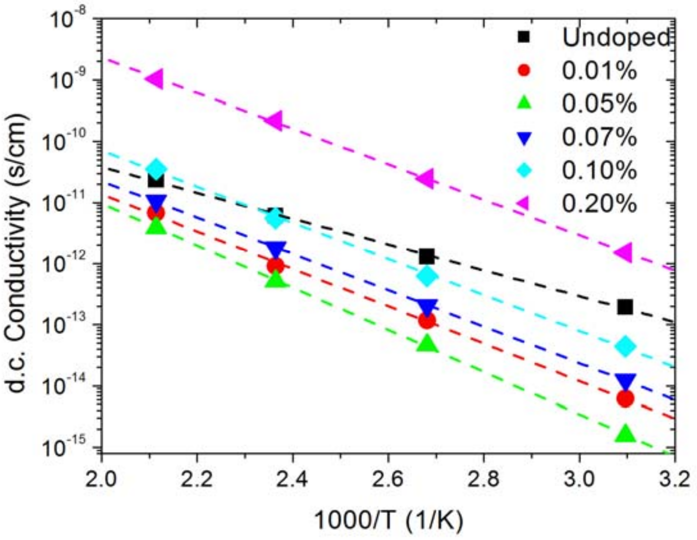

Fig. 8. Arrhenius plot of d.c. conductivity of TiO_2 doped with various amount of Mn.

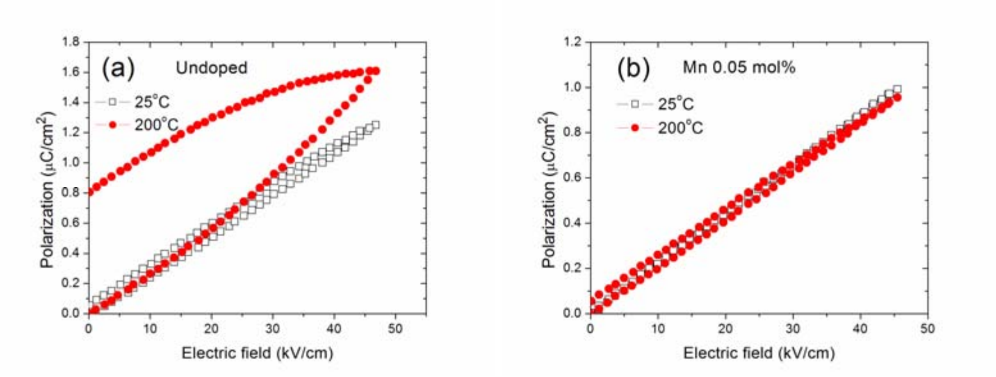

Fig. 9. Polarization-electric field relationship of (a) undoped and (b) 0.05mol% Mn-doped TiO_2 measured at 25°C and 200°C.

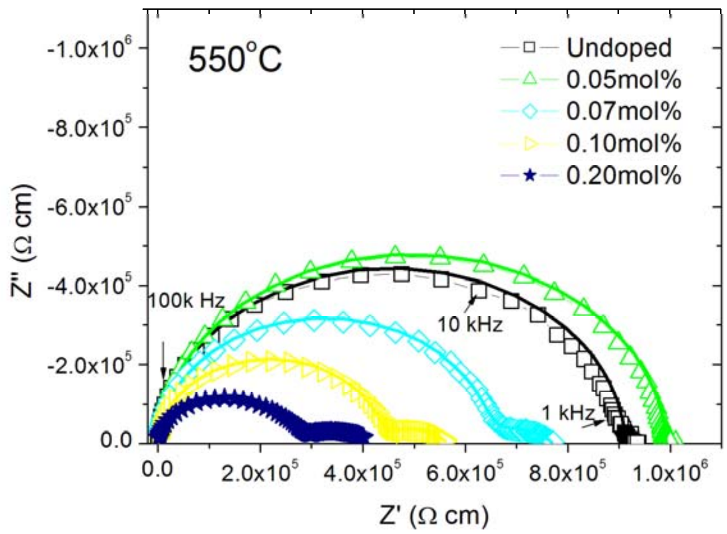

Fig. 10. Impedance spectra and equivalent circuit of TiO_2 doped with various amounts of Mn measured at 550°C (experimental data: open symbol; solid line: fitting curve).

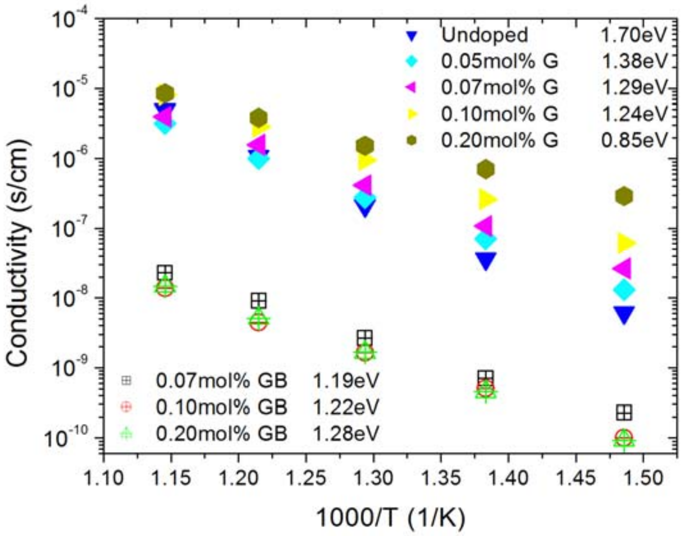

Fig. 11. Arrhenius plot of grain core (designated as G) and grain boundary (designated as GB) conductivity.

Tables

Table Ⅰ. Trace impurities in the starting powders

Elements	Fe	Al	Cl
Concentrations （wt%）	0.001	<0.001	0.016

Table Ⅱ. Grain size of TiO_2 with various amounts of Mn

Mn content (mol%)	Grain size (nm)
0.00	491±124
0.01	455±116
0.03	476±141
0.05	543±137
0.07	553±156
0.10	476±138
0.20	479±168

Table Ⅲ. Impedance data extracted from measurements conducted at 550^{o}C

Mn concentration (mol %)	ρ_1 (Ω·cm)	ρ_2 (Ω·cm)	C_1 (F)	C_2 (F)	CPE1-P (n_1)	CPE2-P (n_2)
0.00	6.21E5	---	5.64E-11	---	0.97	---
0.05	5.80E5	---	5.48E-11	---	0.98	---
0.07	5.94E5	8.61E7	5.67E-11	3.68E-8	0.98	0.62
0.10	3.32E5	9.51E7	5.27E-11	5.22E-8	0.98	0.57
0.20	1.55E5	1.14E8	6.26E-11	7.25E-8	0.95	0.50

4. PROCESSING AND DIELECTRIC PROPERTIES OF TIO_2 THICK FILMS FOR HIGH ENERGY DENSITY CAPACITOR APPLICATIONS

Sheng Chao and Fatih Dogan
Department of Materials Science and Engineering,
Missouri University of Science and Technology, Rolla MO 65401, USA

Abstract

Nanosized TiO_2 powders (~40nm) were used for preparation of tape casting slurries. Effect of various solvents and dispersants on the dispersability of TiO_2 slurries was studied by sedimentation tests and rheology measurements. TiO_2 green tapes were prepared by tape casting method and densified at 1000°C with a sintered density >95%. Dielectric properties of TiO_2 tapes were studied by measuring of dielectric constant, loss factor and dielectric breakdown strength (BDS) with respect to their microstructural development. BDS values as high as ~1400 kV/cm were obtained for sintered tapes so that energy densities up to 14 J/cm^3 could be achieved.

Keywords: Tape-casting; Dielectric properties; TiO_2; Capacitors

1. Introduction

Nanostructured TiO_2 ceramics were found to have significantly improved BDS[1]. Such linear dielectrics are promising candidates for high energy density capacitor applications as the volumetric energy density (J, J/m^3) is governed by the following equation

$$J_{(vol.)} = \frac{1}{2}\varepsilon_0\varepsilon_r E_b^2 \qquad (1)$$

where ε_0 is the permittivity of vacuum (8.854×10^{-12} F/m), ε_r is the relative permittivity (dielectric constant) of the dielectric material and E_b (V/m) is the BDS of the dielectric material.

For practical applications, most ceramic capacitors are manufactured as multi-layer ceramic capacitors (MLCCs) to achieve a high capacitance density. Tape-casting process as a cost effective method is widely used to fabricate MLCCs in large scale.[2] This process generally involves dispersion of ceramic powders in a liquid vehicle, followed by addition of organic binders and plasticizers to give the tape strength and flexibility after casting and drying.[3] Although tape-casting is a well-established ceramic processing technique, using nanopowders as starting material is still a challenging task because of the difficulty of deflocculation or dispersion of powders to prepare slurries suitable to obtain high quality green tapes.[4]

Deflocculation of the nanopowders depends on the appropriate use of both dispersant and solvent.[5] In general, dispersants stabilize the slurry by steric hindrance mechanism or electrostatic repulsion mechanism or both depending on the nature of the dispersant. The major role of solvents is to dissolve organic components and act as dispersion vehicle. Binary solvent systems are commonly used because they offer better compromise between dielectric constant, surface tension and viscosity than a single solvent.[5] The effect of various solvents and dispersants on dispersion of nanosized lead zirconate titanate and barium titanate materials powders have been reported.[6,7]

The objectives of this study are to prepare slurries using nanosized TiO_2 powders suitable for tape casting and characterization of sintered films with respect to their dielectric properties.

2. Experimental procedures

2.1. Starting materials

NanoTek® TiO_2 powders were obtained from Nanophase technologies corporation, Romeoville, USA. Powder characteristics (based on the product data sheet) are given in Table 1. Organic additives such as dispersant, solvent, binder and plasticizer, used for slurry preparation slurry are listed in Table 2.

2.2. Sedimentation tests

Dispersability of TiO_2 nanopowders was studied by performing sedimentation tests on 5vol% suspensions using xylene/ethanol (65:35 volume ratio) binary solvent. Slurries with either 5wt% KD-1 or 2wt% PE or 2.5wt% KD-1 plus 1.0wt% PE or without dispersant were prepared (wt% is based on the weight of the powders). Volumetric cylinders with sealed cap were used to prevent evaporation of the solvent. The suspensions were first sonicated for 2 minutes to break up soft agglomerates of TiO_2 nanopowders before testing. Sedimentation height was recorded at certain time intervals at the interface between the dense sediment and supernatant solvent. The sediment density was calculated by H/H_0, where H is the instantaneous sediment height and H_0 is the initial height.

2.3. Viscosity measurements

To investigate the effectiveness of various dispersants and influence of various solvent systems on the dispersability of TiO_2 nanopowders, viscosities of the slurries were measured. Slurries with 20 vol% solid loading were prepared for viscosity measurements. In order to ensure a good absorption of dispersants on particle surfaces, ball milling of slurries was conducted for 12 hours. Viscosity measurements were performed using a viscometer (VT550, Gebruder HAAKE, Germany) with shear rate shear rate from 100 s^{-1} to 500 s^{-1}.

2.4. Tape-casting of slurries

TiO_2 powders were dried at 200°C overnight before use. First, powders, dispersants and solvents (xylene/ethanol with a 65:35 ratio) were mixed in a high density polyethylene bottle with cylindrical yttria stabilized ZrO_2 milling media (1cm in height and 1cm in diameter). Milling was conducted for 24 hours before adding of the pre-dissolved binder and plasticizer. After milling for another 24 hours, the milling media was removed and milling speed was reduced in order to remove trapped air bubbles. Further de-gassing of the slurry was performed in a vacuum chamber before casting. Tapes were cast on silicon-coated Mylar substrate using doctor-blade with a gap height set to 300μm. After casting, the tapes were dried at room temperature in stagnant air atmosphere for 2 hours. Then the tapes were carefully peeled off from the substrate and laminated at 90°C for 20 minutes under 45 MPa applied pressure.

2.5. Sintering and Characterization

Before sintering, binders were removed at a slow heating rate (0.5°C/min) to 550°C for 1h in ambient air. Sintering was performed in pure oxygen atmosphere (1 atm.) at temperatures ranging from 900°C -1000°C with heating and cooling rates of 5°C/min. The relative density of sintered films was determined by Archimedes' method using water as immersion liquid, assuming the theoretical density of 4.25g/cm^3 for rutile phase of TiO_2. Microstructural development of the green tapes and sintered films were observed by scanning electron microscopy (SEM, Hitachi S4700, Japan) techniques. The grain size was determined by linear intercept method on SEM micrographs by counting of at least 200 grains.

For electrical property measurements, sintered films with a thickness about 0.1 mm were polished by 600 grade grinding papers. Silver paste was painted as top and bottom electrodes followed by annealing at 600°C. D.C. conductivity measurements were performed on a Keithley 6517 Electrometer (Keithley Instruments, Cleveland, USA) by a two-probe method in ambient atmosphere. Dielectric constant was calculated according to the sample geometry and its capacitance measured on a Solartron 1260 impedance analyzer connected with a Solartron 1296 dielectric interface (Solartron analytical, Hampshire, England) in a frequency range of 1Hz to 1M Hz, with voltage amplitude of 1

V. Polarization-electric field (P-E) measurements were conducted using a ferroelectric test system (RT6000, Radiant Technologies, NM USA). For BDS measurements, D.C. voltage was supplied by a Spellman SL30 high voltage generator (Spellman high voltage electronics corporation, New York, USA), with a fixed ramp rate of 250 V/second. The occurrence of BDS was determined by the detection of leakage current over 100 μA.

3. Results and discussion

3.1. Tape-casting and microstructure

The sedimentation height as a function of time of 5vol% TiO_2 suspension is shown in Fig. 1. In general, the suspension with better dispersability should have longer settling time and higher sediment density represented by a low H/H_0 value.[7] From Fig.1 it can be seen that without dispersant, the suspension started to settle immediately after preparation and the H/H_0 value reached a plateau of about 0.5 after seven days. However, by adding dispersant, all the suspensions were very stable, no sign of sedimentation was observed after seven days. KD-1 and PE as well as their mixture were effective dispersants for nanosized TiO_2 powders, but their effectiveness was difficult to compare by sedimentation tests.

Viscosity measurements were employed to determine the optimum combination of solvent and dispersant. Figure 2 shows the viscosities of 20vol% solid loading slurries with 1.2wt% of PE as dispersant using three different solvent mixtures (xylene/ethanol 65:35, toluene/ethanol 40:60, MEK/ethanol 65:35) as a function of shear rate. A shear thinning behavior (viscosity decreases with increasing shear rate) was observed for all slurries with different solvents. This is because with increasing shear rate, viscous force broke some of the agglomerates, resulting in a increase of the suspension fluidity due to the release of immobile liquid within agglomerates.[8] It can be found that the viscosity of the suspension using xylene/ethanol as solvent is consistently lower than the other two types of solvents. It has been reported that both solvent and dispersant will compete with each other for the absorption on the surface of the particles.[6] Polar liquids with strong hydrogen bonding have strong affinity to oxide powder surface. Thus, presumably polar liquid may have the capability to reduce the effectiveness of dispersant. Since ethanol is a polar, MEK weekly polar, toluene and xylene are non-polar liquids, xylene/ethanol solvent mixture (65:35) with minimum amount of polar liquids exhibited the lowest viscosity. Therefore, xylene/ethanol binary solvent was chosen to prepare slurries for tape casting.

The efficiency of dispersants was also examined by viscosity measurement as shown in Fig. 3. The amount of dispersant was optimized by obtaining of minimum viscosity at a shear rate of 100 s^{-1}. PE was found to be more effective than KD-1 as the viscosity of the suspension using PE (1.8wt%) as dispersant is about seven times lower than that of using KD-1 (7wt%) as dispersant.

KD-1 is polyester/polyamide copolymer with an estimated molecular weight about 10,000. It is composed of an anchoring group, which is absorbed onto the particle surface and a polymeric chain with a chemical structure designed to have good solvency in the dispersion medium so as to give optimum steric hindrance to the dispersion.[9] PE contains hydroxyl group, which are ionized to form negatively charged oxygen, and react with ceramic powders electrostatically in the solvent.[10] Thus, PE is expected to stabilize the suspension by both steric hindrance and electrostatic repulsion mechanisms. For tape-casting slurries , dispersants were added as 5.0wt% KD-1, or 2.5wt% KD-1 plus 1.0wt% PE or 2.0wt% PE (these notation will be shorted as KD1, KD1+PE and PE respectively afterwards).

Three different types of tapes were successfully cast by using of KD-1 or KD1+PE or PE as dispersants. The SEM micrographs of green tape surface are revealed in Fig. 4. In general, these tapes show uniform filling and dense packing of powders, an indication of well-dispersed slurry. However, the surface roughness of the tape prepared using KD1 as dispersant is higher than that of tapes prepared using KD1+PE or PE as dispersant. Fig. 5 shows the tape surface after binder removal indicating the formation of large pores or voids. By measuring the weight and the geometry of the tape after binder removal, a density of ~45% was obtained for all three green tapes.

Sintering of the tapes was conducted at temperatures as low as 900°C. It was found that sintering temperature of 900°C and 950°C can only lead to relativity densities of ~81% and ~89%, respectively. Relatively poor sinterability can be ascribed to lower green density, as pellets with ~55% green density can be densified at 900°C.[11] An optimized sintering condition of 1000°C-6h was determined for these tapes, resulting in relative density of 97.9%, 97.7% and 95.1% for KD1, KD1+PE and PE tape, respectively. The SEM images of the film surfaces after sintering at 1000°C for 6h are shown in Fig. 6. Refinement of the grain size is observed in films with PE as dispersant. The average grain size of KD1 film, KD1+PE film and PE film are 1.09μm, 0.48μm and 0.38μm, respectively. It should be mentioned that except the type of the dispersant, the slurry composition of these three different films was the same. Hence, microstructural refinement is attributed to the effect of PE on sintering behavior of TiO_2 tapes. It was reported that PE even in a small amount would decompose; leaving P_2O_5 as solid residue.[12] In other systems such as Al_2O_3[13] and $BaTiO_3$[12], sintering was greatly affected by the presence of PE. Fig. 7 shows that the fracture surfaces of the sintered films prepared using PE as dispersant are significantly different. For KD1 tape, the dominant fracture mode is transgranular, whereas for PE containing tape, the fracture mode is predominantly intergranular. The change of fracture mode is a good indication that the residual phosphorous led to weakening of the bonding strength along the grain boundaries. As discussed in previous sections, PE as a dispersant is strongly absorbed on the surface of TiO_2 nanopowders. After binder removal, phosphorus residues are expected to be uniformly distributed on the particle surface leading to higher phosphorous concentration along the grain boundaries during the sintering process.

In the study of the effects of residual phosphorus on $BaTiO_3$,[12] the effect of grain growth inhibition was attributed to reduced grain boundary mobility as a result of so called solute drag mechanism that may also apply for sintering of TiO_2. During the grain growth, solute elements (Phosphorus) are carried with the moving grain boundary. The solute diffusion coefficient in the grain boundary region is usually lower than the intrinsic diffusion coefficient of host atoms across the boundary plane,[14] thus making solute drag become the rate-limiting factor. According to the solute drag mechanism proposed by Cahn[15] the boundary mobility (M_b) is given approximately by:

$$M_b = D/(\Delta CkT) \qquad (2)$$

where D is the diffusivity of the solute cation, ΔC is the excess concentration of the solute cation in the grain boundary, κ is the Boltzmann constant and T is the absolute temperature. It can be reasonably assumed that ΔC increases with the increase of PE content, leading to a decrease of M_b. The fact that the average grain size of PE film is even smaller than the grain size of KD1+PE film supports the proposed solute drag mechanism. The residual phosphorus content in PE tape was determined to be 0.15 wt% by using of inductively coupled plasma mass spectrometry (ICP-MS).

3.2 Dielectric Properties

Fig. 8 shows the dielectric constant (k) and loss tangent (tgδ) of three types of films. A distinctive difference is observed between the films with or without PE addition. TiO_2 films using KD1 as dispersant exhibit a relatively high apparent dielectric constant ~416 at 1 Hz, while K decreases to ~130 at 1 kHz. The high dielectric constant at lower frequencies is not attributed to the intrinsic property of TiO_2 since it is well-known that the dielectric constant of randomly orientated polycrystalline TiO_2 ceramics is around 100.[16] Thus, the high dielectric constant should be ascribed to extrinsic contribution of polarization mechanisms in addition to the electronic and ionic polarization. With the increase of the frequency, the dielectric constant of KD1 film decreases as the dipoles gradually begin to lag behind the external stimulus frequency. Finally, a plateau about 120 is reached corresponding to the intrinsic dielectric constant of TiO_2. Accompanied with the high dielectric constant, a pronounced loss peak was also observed in KD1 film. The frequency dependency of k' (dielectric constant), k'' (dielectric loss factor, $k''=$

tgδ·k′), and tgδ of KD1 film are shown in Fig. 9. At first glance, the dielectric response looks like the classical Debye-type relaxation, which can be described by the following Debye equations:

$$k' = k_\infty + \frac{k_s - k_\infty}{1+\omega^2\tau^2} \tag{3}$$

$$k'' = (k_s - k_\infty)(\frac{\omega\tau}{1+\omega^2\tau^2}) \tag{4}$$

$$tg\delta = \frac{k''}{k'} = \frac{(k_s - k_\infty)\omega\tau}{k_s + k_\infty\omega^2\tau^2} \tag{5}$$

where ω is the angular frequency; ωτ =1 when the loss factor is at the maximum; k_s and K_∞ represent the static or zero-frequency dielectric constant and dielectric constant at high frequency, respectively.[17] Based on the above equations, the value of K_s and K_∞ were calculated to be ~380 and ~200, respectively. These values are not in perfect match with the experimentally measured data, so that the relaxation processes observed are somewhat deviated from the ideal Debye-type.

Based on the frequency range in which the relaxation occurs, interfacial polarization at the grain boundaries is likely to take place in polycrystalline material (conductivity and/or permittivity difference between grain and grain boundary), as charge carriers piled up at the grain/grain boundary interface. Unlike KD1 tape, the dielectric constant and loss tangent of the tape with PE addition shows non-dispersive characteristics over the entire frequency range scanned. As discussed above, residual phosphorus is expected to segregate at the grain boundaries. Thus, the absence of interfacial relaxation in PE containing tapes should be related to the presence of residual phosphorus at grain boundaries.

In order to further study the effects of PE on the electrical response of TiO_2, complex impedance measurements were conducted for undoped and 2.0 wt% PE doped TiO_2 ceramics sintered at 1000°C for 6 hrs (Fig. 10). At 500°C the individual response of grain interior (high frequency arc) and grain boundary (low frequency arc) can be clearly differentiated for undoped TiO_2, whereas only one semi-circle was indentified for PE doped TiO_2. It was found that the impedance response of undoped TiO_2 can be fitted with two parallel resistor-constant phase element (CPE) circuits connected in series. On the contrary, for doped TiO_2 one parallel resistor-capacitor circuit was sufficient for fitting of the impedance data. While the undoped TiO_2 showed differences in grain and grain boundary conduction, such a difference was not observed for PE doped TiO_2. Although these measurements were conducted at high temperatures to increase the conductivity of TiO_2 for impedance measurements, the microstructural differences should also exist at room temperature. Hence, interfacial polarization occurring at grain boundary was believed to be the cause of anomaly for dielectric constant and loss tangent found in KD1 film.

Dielectric constant and loss tangent measured at certain frequencies are listed in Table 3. It is shown that the loss tangent decreases with increasing frequency, suggesting that the dielectric loss is caused by D.C. conduction. Since TiO_2 does not possess permanent dipoles in the crystal structure, the predominant loss mechanism is expected to be due to the conduction losses. Significantly reduced loss tangent (more than one order of magnitude lower) in PE containing film is due to the combined influence of lower conductivity and the absence of the low frequency relaxation. Suppressed D.C. conductivity with the increasing content of the PE addition is attributed to the defect structure. When donor dopants P^{5+} substitute the normal Ti^{4+} sublattice, charge compensation may take place by formation of V_{Ti}'''', which are believed to have much lower mobility in comparison with oxygen vacancies.[18] The exact reason for the reduced conduction in PE containing tapes require further investigation.

BDS is of great importance to the energy storage capability of dielectric materials as shown in equation 1. Table 3 reveals that the BDS of PE containing film is significantly higher than that of KD1 film, that is in agreement with previous studies that the finer the grain size is the higher the BDS.[1] Generally speaking, the lower the conductivity is, the higher the BDS would be. However, PE films with low conductivity did not lead to high BDS because of their relatively low sintering density. Residual pores can lead to local field concentration[19] and gas discharge inside of the pores may also lead to premature breakdown.[20]

Polarization-electric field relations of the TiO_2 tapes were measured up to ~ 300kV/cm (Fig. 11). Almost ideal linear response was observed for films with PE additions, suggesting a field independent dielectric constant and low dielectric loss. One the contrary, KD1 film exhibits a hysteresis loop similar to those of ferroelectric materials. This loop is believed to be caused by high dielectric loss due to the interfacial polarization as discussed above. The dielectric constant (the slop of the polarization-electric field curve) of the KD1 film is higher than PE containing film, which is in agreement with the low field dielectric constant measurement. The area enclosed within the loop is due to the heat dissipation upon discharge. Hence, the energy storage efficiency (total energy charged/energy released upon discharge) is lower for KD1 films, whereas the nearly linear charge/discharge curve of PE containing films indicates very high efficiency for energy storage. If the polarization-electric filed curve of the TiO_2 tapes with KD1+PE as dispersant can be extended to 1400 kV/cm (BDS value of the tape), an estimated energy density about 14 J/cm^3 would be achieved.

4. Conclusions

TiO_2 nanosized powders with mean particle size ~40nm were dispersed in a mixture of xylene and ethanol as solvents and phosphate ester as dispersant for preparation of tape casting slurries. Green tapes were sintered at 1000^{o}C. Residual phosphorous from decomposition of phosphate ester hindered densification of TiO_2 during sintering and acted as grain growth inhibitor. .The presence of phosphorus affected grain boundary properties of TiO_2 and suppressed the interfacial polarization that was observed in samples without phosphorus. Breakdown strength as high as 1400kV/cm was achieved, indicating a potential energy density of 14 J/cm^3 in phosphorous doped TiO_2.

Acknowledgments

This work was supported by a MURI program sponsored by Office of Naval Research under Grant No. N000-14-05-1-0541.

References

1. Y. Ye, *Grain size dependence of the dielectric breakdown strength of titanium dioxide dielectrics*, Master thesis, University of Missouri-Rolla, Rolla, MO, 2003.

2. R. E. Mistler, and E. R. Twiname, *Tape Casting: Theory and Practice*, The American Ceramic Society, 735 Ceramic Place, Westerville, Ohio, 2000.
3. J. X. Zhang, D. L. Jiang, W. Lars and G. Peter , “Deflocculants for tape casting of TiO_2 slurries,” *J. Euro. Ceram. Soc.*, **24** [8] 2259-2265 (2004).
4. L. P. Meier, L. Urech and L. J. Gauckler, “Tape casting of nanocrystalline ceria gadolinia powder,” *J. Euro. Ceram. Soc.*, **24** [15-16] 3753-3758 (2004).
5. J. X. Zhang, D. L. Jiang, W. Lars and G. Peter, “Binary solvent mixture for tape casting of TiO_2 sheets,” *J. Euro. Ceram. Soc.*, **24** [1] 147-155 (2004).
6. S. B. Reddy and P. P. Singh, ”Effect of type of solvent and dispersant on NANO PZT powder dispersion for tape casting slurry,” *J. Mater. Sci.,* **37** 929-934 (2002).
7. V. Vinothini, P. Singh and M. Balasubramanian, “Optimization of barium titanate nanopowder slip for tape casting,” *J. Mater. Sci.* **41** 7082-7087 (2006).
8. K. H. Zuo, D. L. Jiang, J. X. Zhang, and Q. L. Lin, “Forming nanometer TiO_2 sheets by nonaqueous tape casting,” *Ceram.s Int.*, **33** [3] 477-481 (2007).
9. X. Xu, O. I. L. L. Marta, R. L. Fu and J. M. F. Ferreira, , “Effect of dispersant on the rheological properties and slip casting of concentrated sialon precursor suspensions,” *J. Euro. Ceram. Soc.*, **23** [9] 1525-1530 (2003).
10. L. W. Chu, K. N. Prakash, M.-T. Tsai and Lin, I-N., “Dispersion of nano-sized $BaTiO_3$ powders in nonaqueous suspension with phosphate ester and their applications for MLCC,” *J. Euro. Ceram. Soc.*, **28** [6], 1205-1212 (2008).
11. S. Chao, V. Petrovsky, and F. Dogan, ”Effects of Thermal History on the Dielectric Properties of Nanostructured Titania,” Proceedings of Energy Materials and Technologies I, Materials Science and Technology (MS&T) pp 203-212 2007.

12. A. C. Caballero , J. F.Fernández, C. Moure and P.Durán, ”Effect of residual phosphorus left by phosphate ester on $BaTiO_3$ ceramics,” *Mater. Res. Bull.*, **32** [2] 221-229 (1997).
13. M. Geho, and H. Palmour, “Sources of sintering inhibition in tape-cast aluminas,” *Ceram. Eng. Sci. Proc.*, **14** [11-12] 97-129 (1993).
14. Y.-M. Chiang, D. Birnie Ⅲ, and W.D. Kingery, “Physical Ceramics, Principles for Ceramics and Engineering,” pp. 351-428, MIT Series in Materials Science and Engineering, Edited by C. Robichaud, K. Santor. John Wiley and Sons, New York, NJ, 1996.
15. J.W. Cahn, “The Impurity-Drag Effect in Grain Boundary Motion,” *Acta Mater.*, **10** [9] 789-798 (1962).
16. A. J. Moulson and J. M. Herber, *Electroceramics: Materials, Properties, Applications*, pp. 241 Chapman & Hall, 1990.
17. L. L. Hench and J. K. West, *Principles of Electronic Ceramics*, pp 198-203, John Wiley and Sons, New York, NJ, 1990.
18. L. R. Sheppard, T. Bak, J. Nowotny and M.K. Nowotny, “Titanium dioxide for solar-hydrogen V. Metallic-type conduction of Nb-doped TiO_2,” *Inter. J. Hydrogen Energy*, **32** 2660-2663 (2007).
19. E.P. Gorzkowski, M. J. Pan, B. Bender and C. C. M. Wu, “Glass-ceramics of barium strontium titanate for high energy density capacitors,” *J. Electroceram*, **18** [3-4] 269-276 (2007).

20. C. Mayoux and C.Laurent, “Contribution of partial discharges to electrical breakdown of solid,” *Insulating Materials, IEEE Trans. on Dielectrics and Electrical Insulation,* **2** [4] 641-652 (1995).

Figures

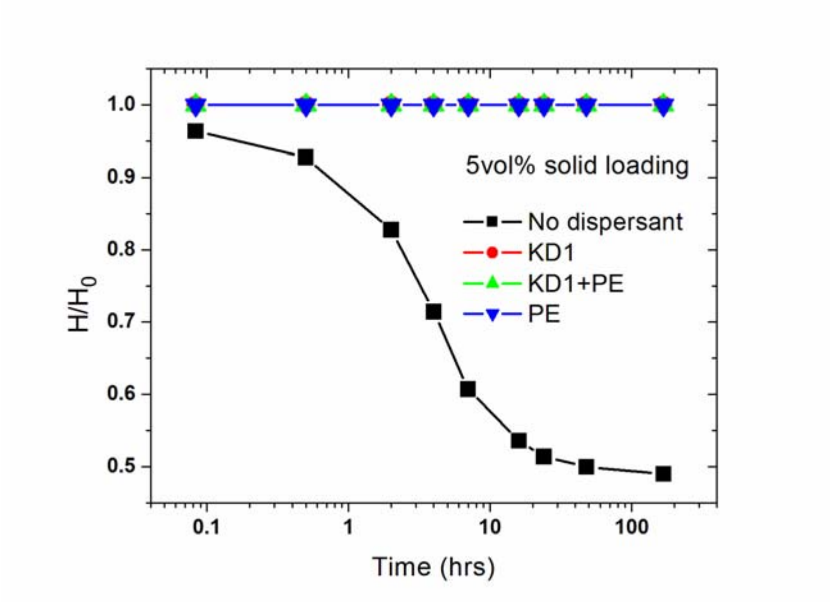

Fig.1. Sedimentation density as a function of time for 5vol% TiO_2 xylene/ethanol suspension with or without dispersant.

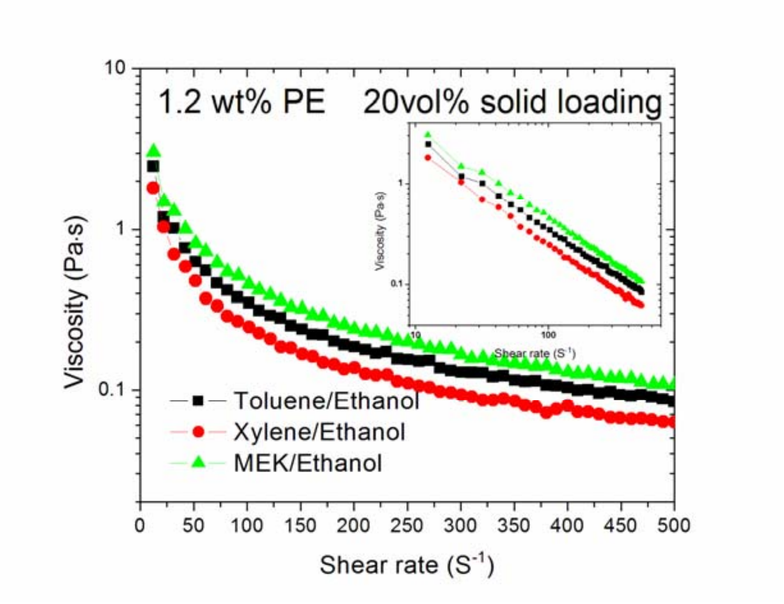

Fig. 2. Viscosity as a function of shear rate of TiO_2 suspension in various types of solvents (the insert is plotted in log-log scale).

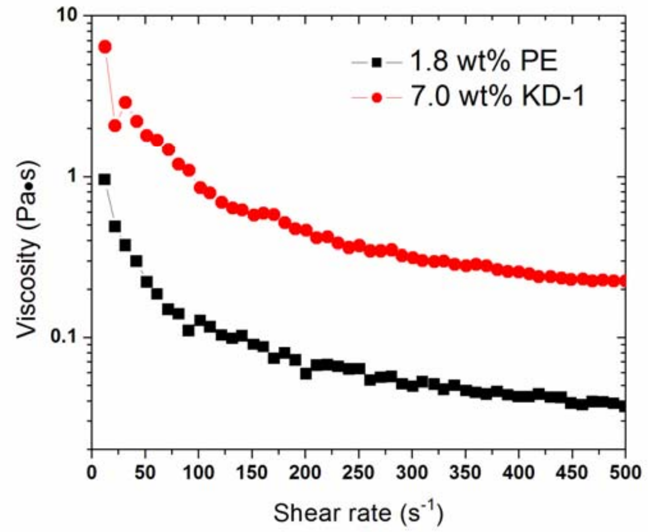

Fig. 3. Viscosity as a function of shear rate of TiO_2 suspension in xylene/ethanol with PE or KD-1 as dispersants.

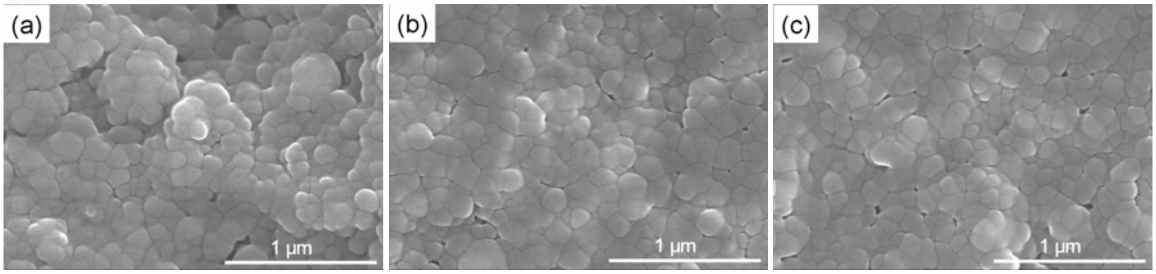

Fig. 4. SEM micrographs of the TiO_2 green tape surfaces using (a) KD1; (b) KD1+PE; (c) PE as dispersant.

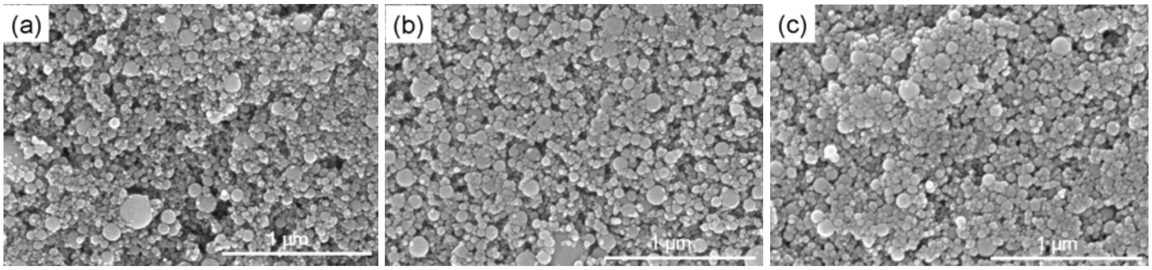

Fig. 5. SEM micrographs of the TiO_2 tape surfaces after binder removal using (a) KD1; (b) KD1+PE; (c) PE as dispersant.

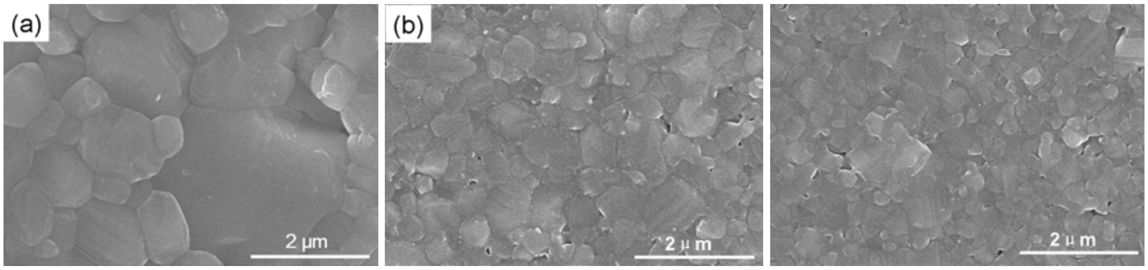

Fig. 6. Microstructure of TiO_2 film surfaces sintered at 1000°C for 6h using (a) KD1; (b) KD1+PE; (c) PE as dispersant.

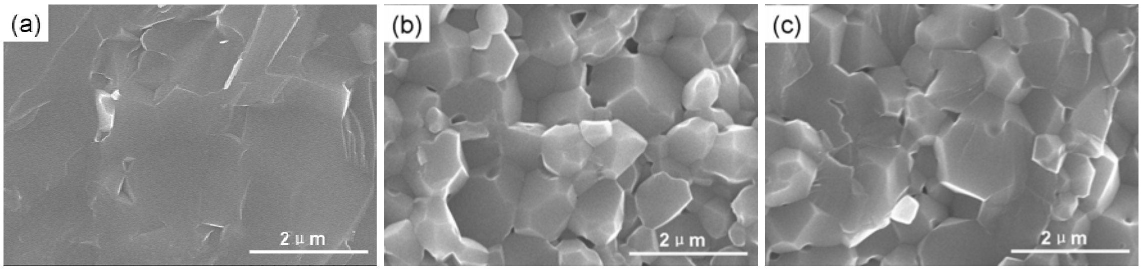

Fig. 7. Fracture surfaces of the TiO_2 film sintered at 1000^oC for 6h using (a) KD1; (b) KD1+PE; (c) PE as dispersant.

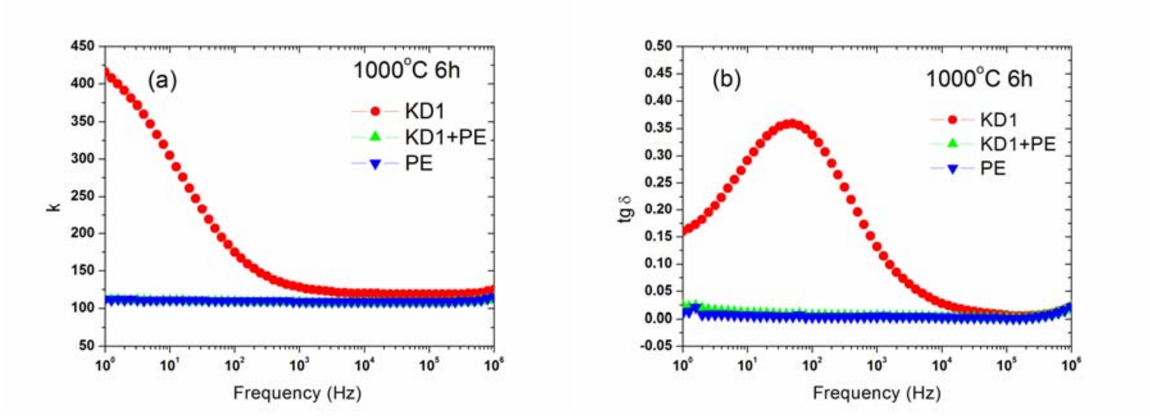

Fig. 8. (a) Dielectric constant and (b) dielectric loss of TiO_2 films sintered at 1000°C for 6h.

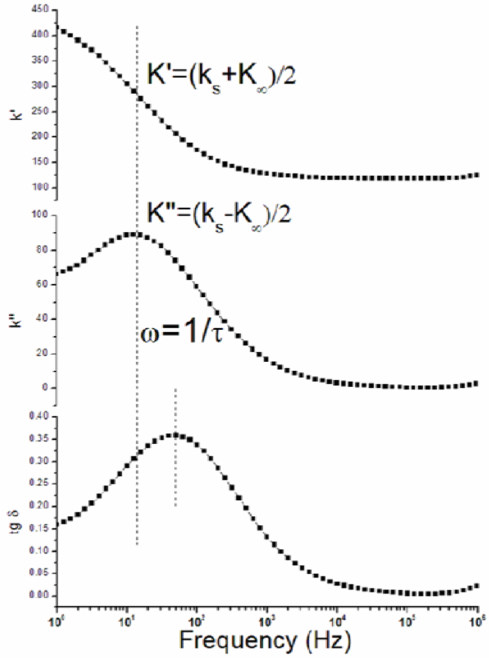

Fig. 9. Dielectric constant, dielectric loss factor and loss tangent as a function of frequency for KD1 films.

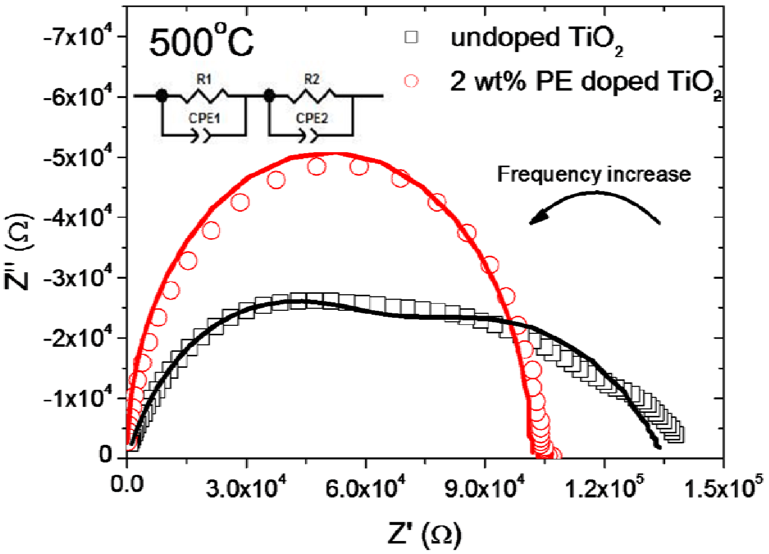

Fig. 10. Impedance response of undoped and PE doped TiO_2 measured at 500°C (open symbols were experimental data and solid lines are the fitting results).

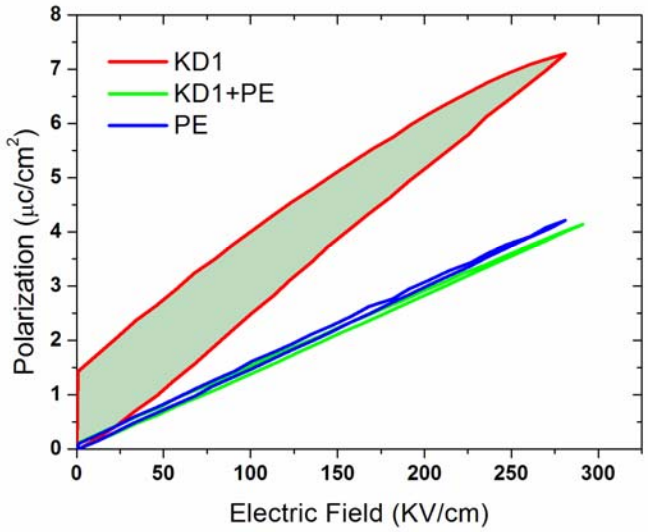

Fig. 11. Polarization-electric field relationship of the TiO_2 films sintered at 1000°C for 6h.

Tables:

Table Ⅰ

Properties of TiO_2 starting powders.

Characteristics	Value
Purity (%)	99.9
Average particle size (nm)	40
Specific surface area (m^2/g)	38
True density (g/cm^3)	3.95
Crystal phase	80% anatase and 20% rutile

Table Ⅱ

Raw chemicals and suppliers.

Functions	Chemicals	Supplier
Solvent	m-Xylene >99.0% (xylene)	Sigma-Aldrich
	Toluene anhydrous 99.8%	Sigma-Aldrich
	Methyl Ethyl Ketone >99.0% (MEK)	Sigma-Aldrich
	Ethanol anhydrous 99.5+% (ethanol)	Sigma-Aldrich
Dispersant	Phosphate ester, Emphos PS-21A (PE)	Witco Chemicals
	Polyester/polyamide copolymer (KD-1)	Tape Casting Warehouse
Binder	Polyvinyl Butyral (PVB-79)	Tape Casting Warehouse
Plasticizer	Dioctyl phthalate 99.0% (DOP)	Sigma-Aldrich

Table III

Electrical and dielectric properties of TiO_2 films sintered at 1000°C for 6h.

	Conductivity (S/cm)	BDS (kV/cm)	Dielectric constant (1kHz)	Loss tangent		
				1k Hz	10k Hz	100k Hz
KD1	2.33E-13	743	128	0.132	0.028	0.006
KD1+PE	1.27E-13	1402	108	0.005	0.002	0.001
PE	8.05E-14	1230	109	0.004	0.003	0.001

5. $BaTiO_3$-$SrTiO_3$ LAYERED DIELECTRICS FOR ENERGY STORAGE

Sheng Chao and Fatih Dogan
Department of Materials Science and Engineering,
Missouri University of Science and Technology, Rolla Missouri, 65409

Abstract

$BaTiO_3$-$SrTiO_3$ (BST) thick films (~250-390 μm) with layered structures were fabricated by tape-casting and lamination process. Layered composites with various Ba/Sr ratios were obtained by lamination of $BaTiO_3$ (BT) and $SrTiO_3$ (ST) tapes in different spatial configurations (2-2). As-prepared BST ceramics showed much improved sinterability over the laminates of pure BT or pure ST tapes. Dielectric properties of materials were measured in the temperature range of 25°C to 200°C. The method of utilizing of layered structures offered flexibility to maximize the energy storage capability at specific operating conditions: (temperature and electric field) by tailoring the dielectric properties through varying the spatial configurations of BT and ST films.

Keywords: $BaTiO_3$, $SrTiO_3$, Dielectric properties, Energy storage

1. Introduction

$Ba_{1-x}Sr_xTiO_3$ (BST) ceramics are widely studied ferroelectric materials with tunable ferroelectric to paraelectric transition temperature by varying of Ba/Sr ratios. BST is a continuous solid solution of BT and ST over the entire range of concentrations [1]. Due to its high dielectric constant (K), low dielectric loss and high tunability, BST has been extensively investigated for its potential applications including capacitors, sensors, phase shifters, and dynamic random access memories [2-4].

Most of the BST related studies were focused on either bulk ceramics or thin films. For bulk ceramics, a solid state reaction process was commonly adopted by using of $BaCO_3$, $SrCO_3$, TiO_2 as starting materials [5,6]. For fabrication of thin films, various techniques such as radio frequency magnetron sputtering [4] or chemical solution deposition methods, including sol-gel method [7, 8] have been used. Functionally graded BST ceramics with a series of Ba/Sr ratios were investigated [9, 10], in order to further lower the temperature coefficient and to broaden the maximum of the dielectric constant.

BST ceramics were considered for application in energy storage capacitors [11], as the energy density of dielectrics is mainly determined by its permittivity and dielectric breakdown strength (BDS). The energy density of dielectrics is given by the following equation:

$$J = \varepsilon_0 \int \varepsilon_r(E) E dE \qquad (1)$$

where J is the energy density (J/cm^3), ε_0 is the permittivity of free space (8.85×10^{-12} F/m), $\varepsilon_r(E)$ is the electric field dependent dielectric constant and E is the electric filed (V/m). It has been demonstrated that the energy density of ferroelectrics can be optimized if their properties (spontaneous polarization, Curie temperature and BDS) are known [12]. In the present study, BST ceramics were fabricated by lamination of individual BT and ST tapes to form a 2-2 composite configuration. Dielectric properties of composites were characterized with an emphasis on the energy storage capability.

2. Experimental procedure

BT and ST thick films were prepared by tape-casting method. Tape casting slurries were prepared by using of Methyl ethyl ketene/Toluene (1:1 volume ratio, Sigma Aldrich), polyvinyl butyl (PVB-79, Tape Casting Warehouse) and benzyl butyl phthalate (Sigma Aldrich) as binary solvent, binder and plasticizer, respectively. High purity (>99.9%) BT and ST powders ~200nm (TPL, Inc.) were first dispersed in the solvent by adding of KD-1 (Polyester/polyamide copolymer, Tape Casting Warehouse) as dispersant. After adding of binder and plasticizer, the slurry was ball milled for 24 hrs. After casting on Mylar substrates, BST layered structures were fabricated by lamination of BT and ST green tapes in various configurations as shown in Fig. 1. The tapes were laminated first isostatically at 180 MPa at room temperature, followed by hot pressing at 85^{o}C under an applied pressure of 40MPa. Binder removal process of the tapes was conducted at 500^{o}C for 1h, followed by sintering at 1300^{o}C for 1h in ambient air.

Microstructural development of sintered films was observed by scanning electron microscopy (SEM, Hitachi S-4700) techniques. The samples were electroded with silver paste for measurement of dielectric properties. Dielectric constant and loss tangent were measured with a Solartron 1260 impedance analyzer connected with a Solartron 1296 dielectric interface using an a.c. voltage of 1V at 1k Hz. Polarization-electric filed (P-E) relationships were measured with a ferroelectric testing system (RT6000, Radiant Technology). BDS measurements were conducted under D.C. bias by using a high voltage generator (Spellman SL30).

3. Results and discussion

Fracture surface of BST laminates are shown in Fig. 2. It was found that the BST laminates containing both BT and ST tapes showed better sintering behavior (~20% more shrinkage in thickness direction) than laminates composed of BT or ST tapes. Nearly full density was achieved in BST laminates with BT and ST alternating layers, while BT and ST dielectrics showed residual porosity.

Dielectric constant and loss tangent of BST laminates were measured from 25^oC to 200^oC (Fig. 3). For BT laminates at T_c ~130^oC, a sharp peak of dielectric constant was observed, which is typical for BT materials. With the increase of Sr content, peak of dielectric constant become sluggish. It was reported that the T_c decreases to near room temperature for $Ba_{1-x}Sr_xTiO_3$ ceramics with x=0.30 [10]. In the present study, laminates of BT: ST 6:2 with an overall composition of $Ba_{0.72}Sr_{0.28}TiO_3$ did not exhibit this behavior, indicating the presence of a compositional gradient. With the increase of Sr content, the dielectric constant of the laminates gradually decreases from K:~3800 for BT:ST 6:2 to K:~290 for ST 6 at room temperature . The temperature coefficient capacitance (TCC) was calculated, which is a measure of temperature stability of capacitance:

$$TCC = \frac{k(T^oC) - k(25^oC)}{k(25^oC)} \qquad (2)$$

where k(T°C) is the dielectric constant at a given temperature and k(25°C) is the dielectric constant at 25°C. In Ba-rich (from BT 6 to BT: ST 3:2) BST laminates, except for BT 6, all samples have nearly the same maximum TCC values at ~75% within the temperature range measured. In Sr-rich BST laminates (from BT: ST 5:5 to ST 6), maximum TCC values decrease from ~72% for BT:ST 5:5 to ~30% for ST 6. The variation of TCC observed in this study is much lower than that of BST ceramics with fixed Ba/Sr ratio, i.e., BST without a compositional gradient. For instance, it was reported that for BST with Ba/Sr=1:1, TCC changed ~300% within the temperature range from 25°C to 175°C [1]. Less variation of capacitance is beneficiary for operation of capacitor in a wider temperature range, and this is attributed to graded compositions of BST laminates as a result of inter-diffusion of BT and ST during sintering.

Loss tangent of the laminates showed a strong dependence on compositions. Both pure BT and pure ST laminates exhibited relatively high losses. It can be seen that with the increase of Sr content, the loss tangent increases particularly at higher temperatures. A similar trend was observed in the study of BST ceramics of homogeneous composition with a series of Ba/Sr ratios, which was attributed to disordered and more mobile Sr ions [13]. However, laminates with composition of BT:ST 6:2, BT:ST 4:2 and BT:ST 3:2 demonstrated lower dielectric loss (~1%- 2%), in comparison with BST of similar but homogeneous compositions [5, 13].

P-E relationships were measured at room temperature as shown in Fig. 4. The energy storage capability of the dielectrics can be directly illustrated by their P-E relationships, as depicted in the insert of Fig. 4 (a). The shaded area represents retractable energy density upon discharge, while the area within the charge and discharge curve is attributed to the energy loss. For most applications, a high polarization is required while a narrow P-E hysteresis loop is desired to minimize the loss.

BST laminates in Ba-rich compositions demonstrated the characteristics of ferroelectric materials (Fig. 4a). With the increase of Sr content, both saturation polarization and remanent polarization decreases. The P-E relationship of BST laminates in Sr-rich compositions (Fig. 4b) showed linear characteristics, indicating that they are in paraelectric states. Thus, it was demonstrated that by employing of layered structures, various P-E relationships can be obtained by compositional and/or structural design. Consequently, the energy storage capability of the dielectrics can also be tailored to meet the needs of specific applications.

The energy density was calculated by integration of the area within the discharge curve and polarization axis. Since the thicknesses of the samples are not identical (due to different number of layers), the energy densities summarized in Table 1 are the values at the maximum electric field applied, except for the sample BT 6 which was measured near its BDS. It was observed that BST laminates (BT:ST 6:2 and BT:ST 4:2) with a narrow P-E curve and relatively high polarizations, demonstrated better energy storage capability. BDS of the BST laminates increases with the increase of Sr content (Table 1). The BDS value of the samples BT 6 and ST 6 are comparable to data reported in the literature, such as ~85kV/cm for BT ceramics [14] and ~ 414 kV/cm for ST single crystal [15]. Higher energy density is attainable if P-E measurements are conducted at higher fields; however, in present study the output voltage was limited to 4 kV due to the limitation of the power supply. In addition, it should be mentioned that much higher BDS and consequently much higher energy density can be expected if the sample thickness could be reduced, as BDS has a strong dependence on the dielectric thickness.

4. Summary

BST thick films with a compositional gradient were fabricated by a tape-casting and lamination process. Dielectric properties such as dielectric constant maximum, loss tangent, TCC and P-E relationships of the composites were tailored by varying of spatial configuration of BT and ST layers. Higher sintering densities were achieved in layered BST ceramics prepared with a compositional gradient in comparison to BST with a homogeneous chemical composition. Consequently, the dielectric properties and energy storage capability of layered BST composites can be tailored for specific capacitor applications.

Acknowledgments

This work was supported by a MURI program sponsored by Office of Naval Research under Grant No. N000-14-05-1-0541.

References

[1] Zhang L, Zhai J, Yao X. Mater Res Bull. 2009; 44:1058-61.

[2] Guo HL, Gao W, Yoo J. Mater Lett. 2004; 58: 1387-91.

[3] Tick T, Peräntie J, Jantunen H, Uusimäki A. J Eur Ceram Soc. 2007; 28: 837-42.

[4] Tsai MS, Sun SC, Tseng TY. J Am Ceram Soc. 1999; 82:351-58.

[5] Rhim SM, Hong S, Bak H, Kim OK. J Am Ceram Soc. 2000; 83:1145-48.

[6] Berbecaru C, Alexandru HV, Porosnicu C, Velea A, Ioachim A, Nedelcu L, Toacsan M. Thin Solid Films. 2008; 516: 8210-4.

[7] Schwartz RW, Glem PG, Voigt JA, Byhoff ER, Stry M, Headley TJ, Missert NA. J Am Ceram Soc. 1999; 82: 2359-67.

[8] Liu QX, Tang XG, Deng YY, Wang J, Chan HLW. Mater Chem Phys. 2008; 112: 281-4.

[9] Viviani M, Barrel J, Buscaglia MT, Buscaglia V, Vardavoulias M, Stytsenko E. J Euro Ceram Soc. 2007; 27: 4353-7.

[10] Jeon JH, Hahn YD, Kim HD. J Euro Ceram Soc. 2001; 21:1653-6.

[11] Dong G, Ma S, Du J, Cui J. Ceram Inter. 2009; 35: 2069-75.

[12] Fletcher NH, Hilton AD, Ricketts BW. J Phys D: Appl Phys. 1996; 29: 253-8.

[13] Mohan CRK, Bajpai PK. Physica B. 2008; 403: 2173-88.

[14] Tunkasiri T, Rujijanagul G. J Mater Sci Lett. 1996; 15:1767-9.

[15] Barrett HH. J Appl Phys. 1964;5: 1420-5.

Figures

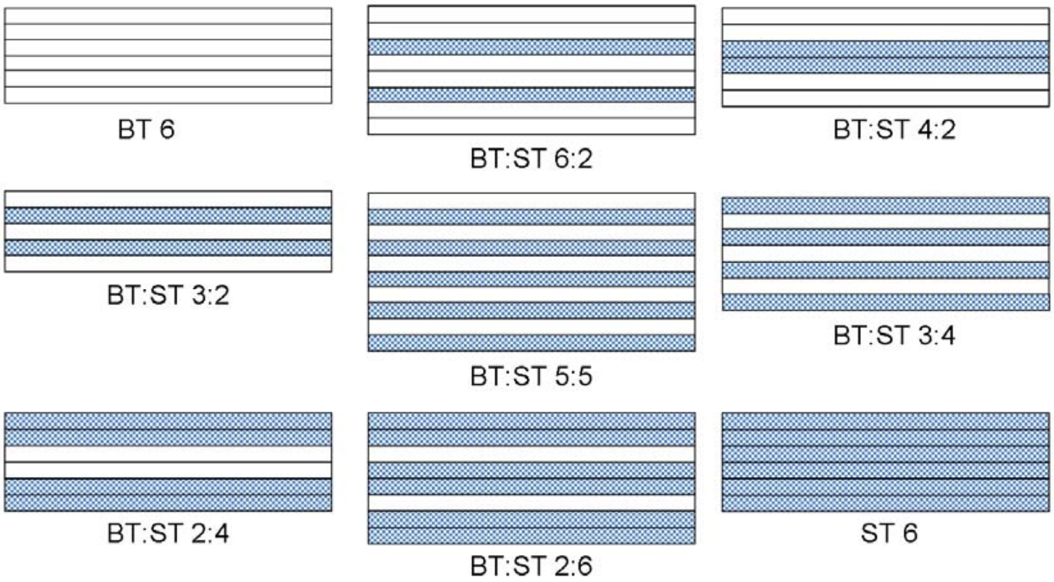

Fig. 1. Spatial configuration of BST laminates.

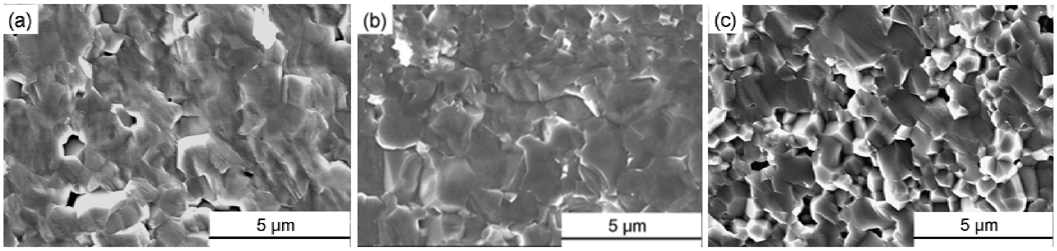

Fig. 2. Microstructure of the fracture surface of BST laminates: (a) BT 6, (b) BT:ST 5:5 and (c) ST 6.

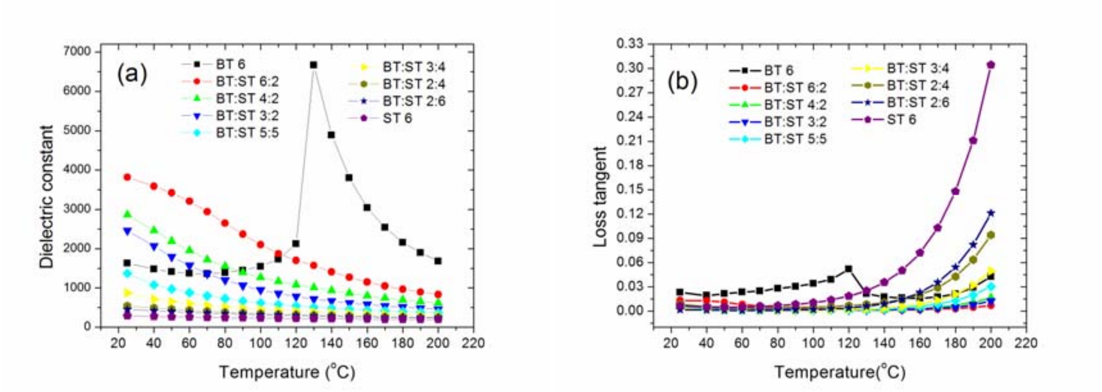

Fig. 3. Dielectric constant (a) and loss tangent (b) of BST laminates measured at various temperatures.

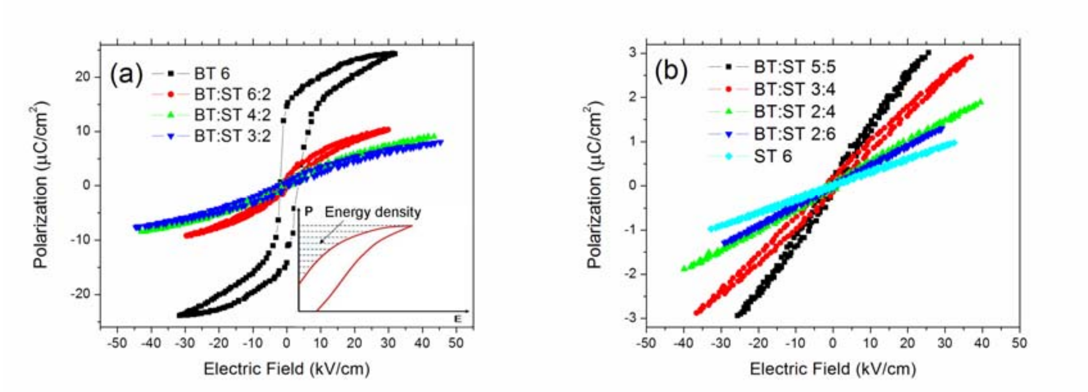

Fig. 4. P-E relationship of BTS laminates in (a) Ba-rich composition and (b) Sr-rich composition measured at room temperature.

Tables

Table 1. Energy densities calculated from P-E curves based on the applied electrical field and breakdown strength (BDS) of BST laminates at room temperature

Samples	Sample thickness (μm)	Energy density (J/cm^3) @ electric field (kV/cm)	BDS (kV/cm)
BT 6	310	0.31 @ 62	97±21
BT:ST 6:2	330	0.65 @ 119	190±93
BT:ST 4:2	250	1.16 @ 157	218±86
BT:ST 5:5	390	0.47 @ 101	233±92
BT:ST 2:6	350	0.30 @ 112	275±74
ST 6	320	0.25 @ 123	353±65

APPENDIX 1

EFFECTS OF DONOR DOPING ON THE DIDLECTRIC PROPERTIES OF TITANIUM DIOXIDE CERAMICS

1. Research background

In the main body of the thesis it was discussed that due to the presence of acceptor type of impurities or dopants, space charge polarization would take place as electric-conduction blocking grain boundaries were formed due to the creation of negatively charge defects at grain boundary core. During the study of TiO_2 thick films fabricated by tape casting method, it was found that with presence of residual phosphorus, the space charge polarization process was completely removed and only one semi-circle representing the bulk grain response can be observed. This observation indicates that with the introducing of donor type impurities/dopants, charge neutralization may take place according to the following defects reaction:

$$Null = D_{Ti}^{\bullet} + A_{Ti}^{'} \qquad (1)$$

here $D^{\bullet}_{Ti}$ represents the defect created by donor doping with one positive charge, while $A^{'}_{Ti}$ represents the defect created by acceptor doping with one negative charge. By eliminating the influence of space charge, dielectric loss was substantially reduced and the BDS was greatly enhanced, both of which are important for the improvement of the energy storage capability. Hence, it is worthwhile to do a systematic investigation on the influence of donor doping on the dielectric properties of TiO_2 ceramics.

2. Sample preparation

TiO_2 powders obtained from Nanophase Technologies Corporation were used as undoped baseline materials. Two type of donor dopants Phosphorus (P) and Vanadium (V) were introduced. For P doping, phosphate ester was used as P source. Appropriate amount of phase ester was added into the TiO_2 powders and ball milled in 2-proponal solution for 12hrs. Drying was conducted under constant stirring on a hot plate. After crushing, TiO_2 powders with a series of P doping levels were obtained. For V doping, vanadium isopropoxide was used as V source. Powder preparation method was similar to that of P doped TiO_2 powders. Pellets for electrical property measurements were fabricated in the same way as described in papers listed in the main body of the thesis. Sintering of the pellets was performed in a series of temperatures from $800^{o}C$ to $1000^{o}C$ for 2hrs in oxygen atmosphere. Dielectric properties were measured at various temperatures using the same equipments and methods described in the papers listed in the main body of the thesis.

3. Results and discussion

Since it was found that the presence of P can retard the sintering process. P doped TiO_2 ceramics were sintered from $850^{o}C$ to $1000^{o}C$ for 2hrs, in order to find out the suitable densification temperature. A plot showing the relationship between sintering temperature and relative density is given in Fig. 1. It can be seen that generally the higher the doping concentration is, the lower the density would be at the same sintering temperature. This phenomenon was attributed to the solute drag mechanism that reduced the mobility of the grain boundaries. This study showed that for P doped samples, a densification temperature of $950^{o}C$ or higher is necessary. Fig. 2 shows the SEM images of undoped and P doped TiO_2 ceramics sintered at $950^{o}C$ for 2hrs. A grain size refinement in P doped TiO_2 ceramics was evident. Again, this phenomenon was ascribed to the solute drag mechanism due to the presence of P elements at grain boundaries.

Unlike P doped samples, V doping did not have a substantial influence on the sinterability and grain size of TiO_2 ceramics, as shown in Fig. 3. Hence, if V doping can affect the dielectric properties of TiO_2 the same way as P doping, it would be a preferred donor dopants as densification can be completed at lower temperatures.

The dielectric constant and loss tangent of undoped and P or V doped samples (at their individual optimum doping levels) sintered at 1000^{o}C for 2hrs are shown in Fig. 4. It was observed that both P and V doping can effectively remove the space charge polarization taking place at ~10Hz, resulting in significantly lowered dielectric loss. Even at 200^{o}C, the dielectric loss of P or V doped samples was reduced to <2% at 1k Hz (Table 1), which is critically important for high temperature applications.

Impedance measurements were conducted to differentiate the individual response of bulk grain and grain boundary. One example is given in Fig. 5 showing distinctive differences between undoped and P or V doped samples. For undoped sample, two semi-circles representing bulk grain and grain boundary response, respectively can be clearly seen. However, for P or V doped samples, one big semi-circle attributed to the bulk grain effect dominates the impedance spectra. This difference indicates that by introducing of P or V as dopants, the originally heterogeneous microstructure becomes uniform. Charge neutralization among negatively charged and positively charged defects is believed to be the cause of this change, which can be described by equation (1).

Polarization-electric field relationships were measured at room temperature (Fig. 6) and 200^{o}C (Fig. 7). It was observed that at room temperature, all samples demonstrated almost ideal linear P-E relationships. Overlapped charge and discharge curves indicate that near 100% energy storage efficiency can be achieved. However, at

$200^{o}C$, undoped sample starts to show energy losses which is represented by the area encircled by the charge and discharge curve. Energy storage efficiency reduced to 82.8% for undoped TiO_2 at $200^{o}C$. On the contrary, good linear P-E relationships were maintained in P or V doped samples, with much higher energy storage efficiency of 96.4% and 94.8% for P doped and V doped sample, respectively. Therefore, it can be seen that both P and V doping can effectively improve the energy storage capability of TiO_2 ceramics at elevated temperatures.

4. Summary

Donor doping of P or V can neutralize the negatively charged defects at grain boundary cores caused by segregation of acceptor type of impurities in the starting powders. As a result, the microstructure of P or V doped TiO_2 become homogeneous, and the phenomenon of space charge was eliminated. The dielectric loss was significantly reduced while the energy storage capability was greatly enhanced particularly at elevated temperatures, when P or V was introduced as donor dopants.

Figures

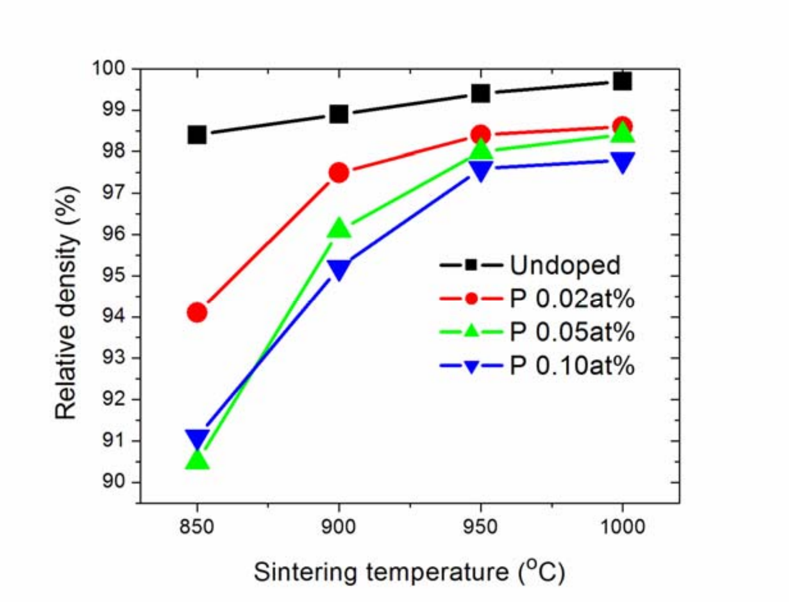

Fig.1. Relative density as a function of sintering temperatures of undoped and P doped TiO_2 ceramics.

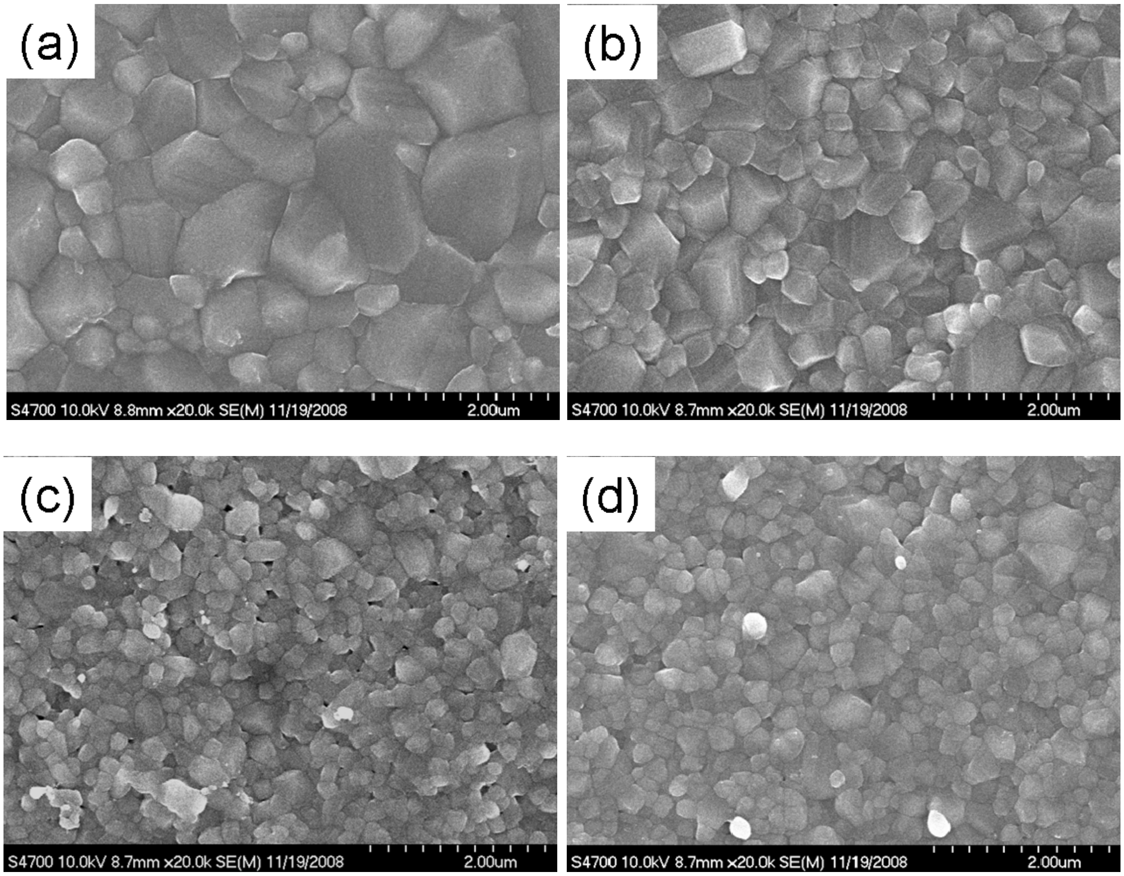

Fig. 2. SEM images of the surfaces of (a) undoped TiO_2; (b) P 0.02 at% doped TiO_2; (c) P 0.05 at% doped TiO_2 and (d) P 0.10 at% doped TiO_2 sintered at 950°C for 2hrs.

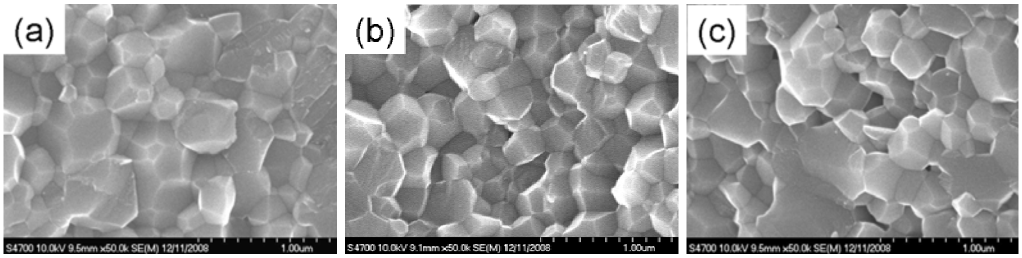

Fig. 3. SEM images of fracture surfaces of (a) undoped TiO_2; (b) V 0.05 at% doped TiO_2 and (c) V 0.10 at% doped TiO_2 sintered at 800^oC for 2hrs.

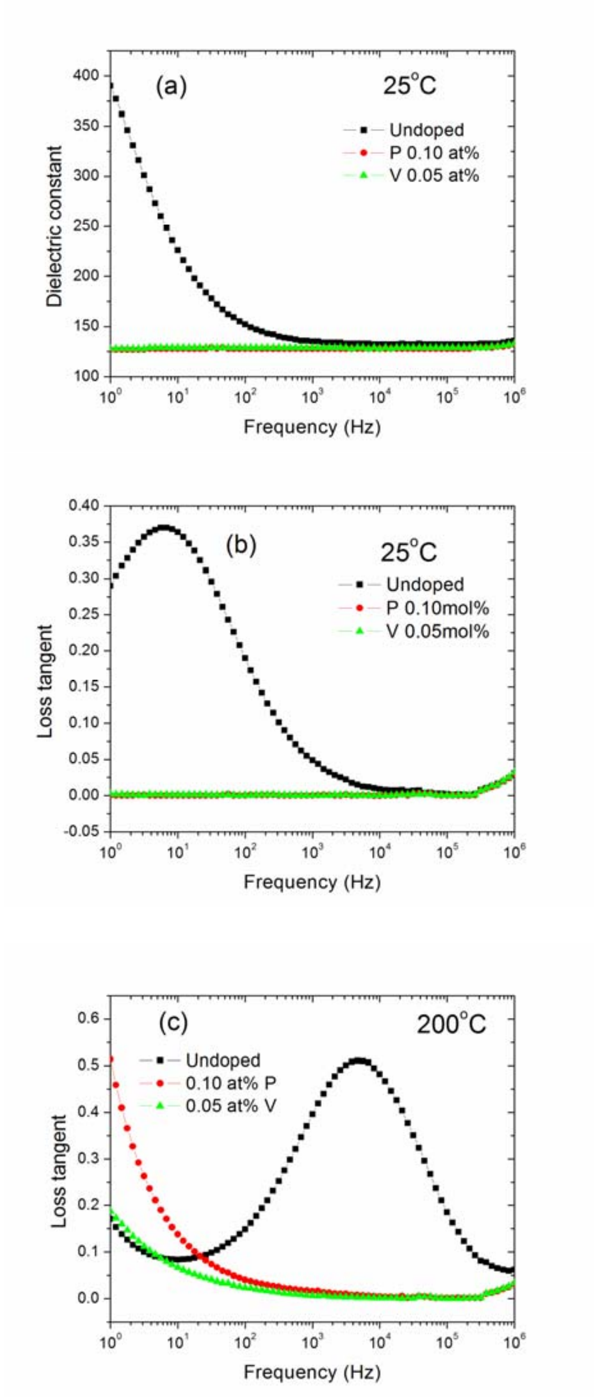

Fig. 4. (a) Dielectric constant (room temperature); (b) loss tangent (room temperature) and (c) loss tangent (200°C) of undoped and P or V doped TiO_2 ceramics sintered at 1000°C for 2hrs.

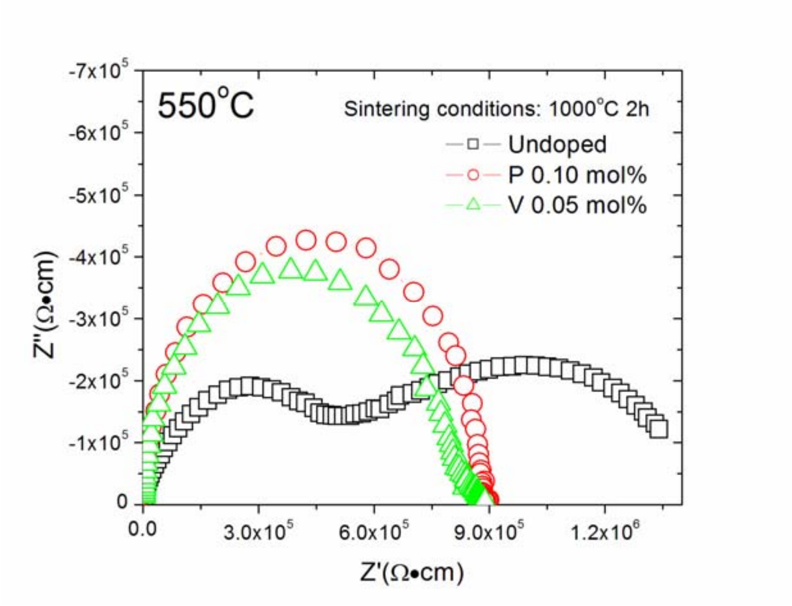

Fig. 5. Complex impedance spectra of undoped and P or V doped TiO_2 ceramics measured at 550°C.

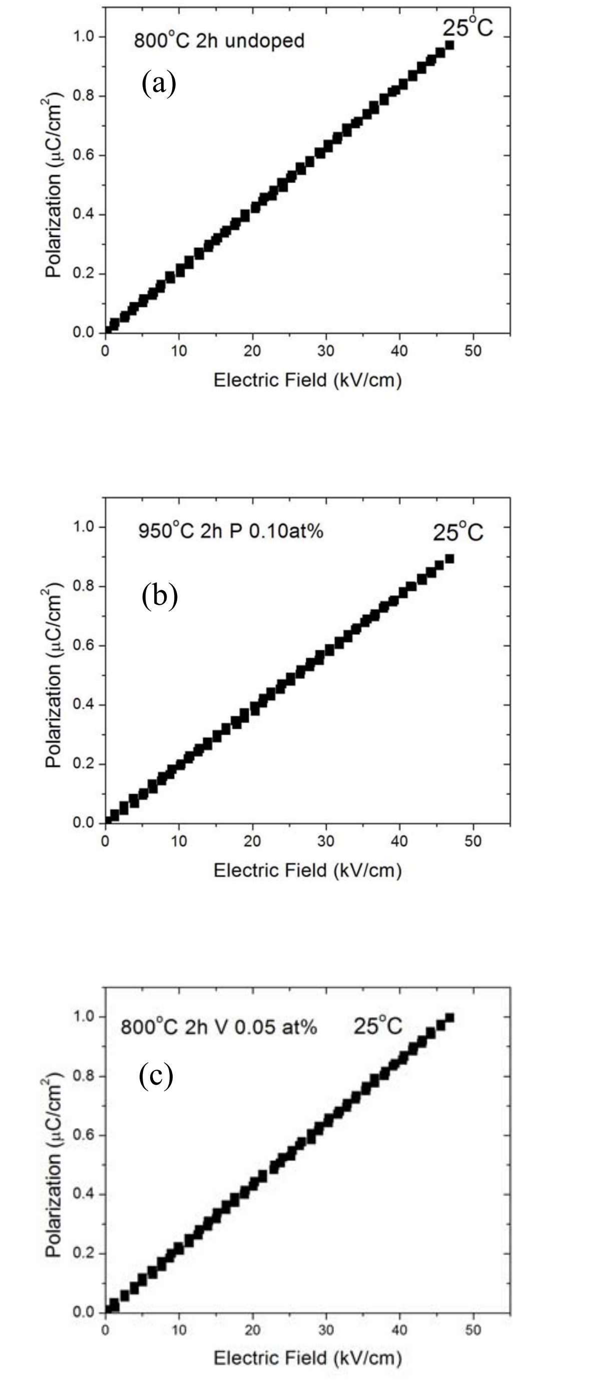

Fig. 6. Room temperature polarization vs. electric field relationships of (a) undoped; (b) P doped and (c) V doped TiO_2 ceramics sintered at designated conditions.

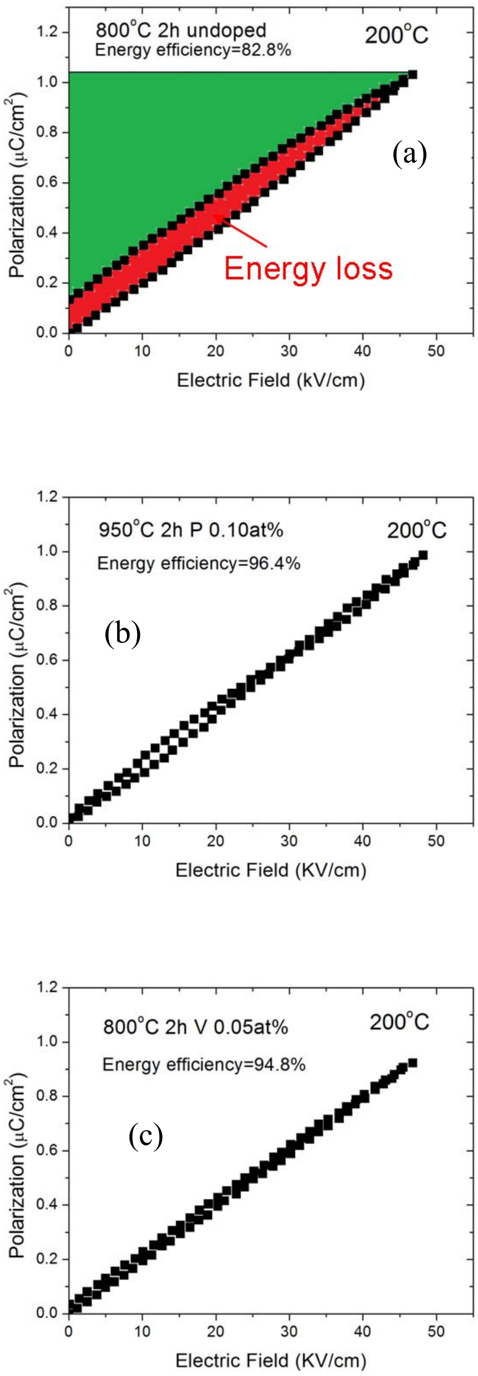

Fig. 7. Polarization vs. electric field relationships of (a) undoped; (b) P doped and (c) V doped TiO_2 ceramics sintered at designated conditions measured at 200°C.

Tables

Table.1 Loss tangent of undoped and P or V doped TiO_2 measured at 25^oC and 200^oC

Samples	tgδ @ 25^oC 1k Hz	tgδ @ 200^oC 1k Hz
Undoped	4.88%	39.60%
P 0.10at%	0.02%	1.58%
V 0.05at%	0.02%	0.67%

APPENDIX 2

PROCESSING AND CHARACTERIZATION OF HYDROTHERMAL $BaTiO_3$ FILMS ON STAINLESS STEEL

1. Sample Fabrication

Stainless steel was used as substrates, onto which poly(dibutyltitanate) (Gelest Inc.) diluted with 1-Butanol (Fisher Scientific) was spin coated at 2500 rpm for 30 seconds. A second layer was spin coated after baking at 95°C. Then the bi-layer precursor was pyrolyzed at 500°C for 1h in air. 0.5M, 1 M and 2M aqueous solution of $Ba(OH)_2$ was prepared by adding appropriate amount of $Ba(OH)_2 \bullet 8H_2O$ (Alfa Aesar) to pre-boiled D.I. water. Pyrolyzed film was placed in a horizontal position in a polyethylene bottle containing 20ml of as-prepared $Ba(OH)_2$ solution and sealed instantly. Reaction took place at 90°C for a duration time ranging from 4-24 hours. After reaction, films were removed and rinsed with boiled D. I. water and dried at 150°C. Some of the films were also heated at 500°C for various times.

2. Characterization

Phase analysis of the films was performed by using X-ray diffraction (XRD, Philips X-Pert). Film morphology and roughness were examined by Scanning Electron Microscopy (SEM, Hitachi S-4700) and Atomic Force Microscopy (AFM, NanoScope IIIa). X-ray Photoelectron (XPS, Kratos Axis 165) and Auger Electron Spectroscopy (AES, Physical electronics 545) analysis were also performed to study the surface chemistry and element depth profile of the film.

3. Microstructure Development

3.1 Effect of $Ba(OH)_2$ Concentration

SEM micrographs of $BaTiO_3$ films synthesized using 0.5M, 1.0M and 2.0M

$Ba(OH)_2$ solutions for 6hrs are shown at Fig. 1. It can be seen that all films were composed of uniform size of grains about 20nm, independent of the $Ba(OH)_2$ solution concentration. Previously, it was found that increasing the $Ba(OH)_2$ concentration may cause a decrease in grain size [1]. However, there is little effect of $Ba(OH)_2$ concentration on grain size in this study, which could be contributed to low processing temperature and short processing times as the grains have not enough thermal energy and time to grow. Fig. 2 shows the XRD pattern of the $BaTiO_3$ films synthesized in 2.0M $Ba(OH)_2$ solution for 12hrs. Peaks of both $BaTiO_3$ (PDF 05-0602) and stainless steel (PDF 33-0397) are detected. Generally, hydrothermal synthesis at <240°C leads to formation of cubic $BaTiO_3$, with a particle size of <100nm [2]. However, in this study $BaTiO_3$ peaks show little characteristics of tetragonal phase (peak splitting at $2\theta \sim 45^o$) even though the particle size is only around 20nm. Since XRD along may not be convincing enough to prove the presence of tetragonal phase, other characterization techniques are need to confirm the crystal structure of as-synthesized $BaTiO_3$ films.

3.2 Effect of Reaction Time

Fig. 3 shows the SEM micrographs of the $BaTiO_3$ films synthesized at different reaction times. Films processed in 1.0M $Ba(OH)_2$ for 4hrs failed to form a complete coverage of the substrate (Fig. 2(a)). After 12hrs' reaction, the substrate was completely covered by $BaTiO_3$ particles (Fig. 2(b)). Dark regions between the grains are thinner sections of the film, which are revealed by AFM image (Fig. 4). Increasing the $Ba(OH)_2$ concentration to 2.0M led to the formation of denser films (Fig. 2(c)). According to the film morphology it seems that nucleation starts first at certain sites of the substrate, then the entire surface of the substrate was slowly covered. Film formation was facilitated by increasing the $Ba(OH)_2$ concentration and the processing time.

4. Chemical Characterizations

4.1 XPS Surface Analysis

XPS survey in the 0-1000eV binding energy range for the $BaTiO_3$ film treated in 2M $Ba(OH)_2$ solution for 8hrs showed surface carbon contamination, which disappeared after the Ar ion sputtering. The O 1 s peak shown in Fig. 5 (a) can be splitted into two peaks after fitting. The main peak located at 529.0eV is attributed to oxygen presented in $BaTiO_3$ while the small peak at 530.7eV is believed to be associated with oxygen in hydroxyl (OH^-) groups. This result is in good agreement with literature [3]. Hydroxyl groups are commonly observed in powders or films fabricated by hydrothermal techniques, which is one of the major drawbacks of this technique since the presence of these hydroxyl groups are believed to be detrimental to dielectric properties [4]. Heat treatment is helpful to remove absorbed hydroxyl groups, as evidenced by Fig. 5 (b). It can be seen that after 500^{o}C 1h heat treatment in air, the shoulder of O 1S peak becomes smaller. It is possible that residual hydroxyl groups presenting in the lattice of $BaTiO_3$, and heat treatment at higher temperature is necessary to remove them.

4.2 AES Depth Profile

An AES depth profile of $BaTiO_3$ film treated in 2M $Ba(OH)_2$ solution for 24hrs is shown in Fig. 6. Near the surface, the carbon signal was very strong then it decreased sharply at a distance about 15nm inside the film. $BaCO_3$, which is easily formed in air, may be the source of the strong carbon signal. Good correlation between Ba, Ti, and O signals indicates stoichiometric or near stoichiometric $BaTiO_3$ films. A diffusion region about 100nm in depth, in which Ba, O, Ti signals decreases sharply while Fe, Cr, Ni signals increase significantly, is revealed. About 2 at% of Fe diffused into the $BaTiO_3$ films, which may lead to a Fe doping effects since Fe ions could occupy the Ti sites [5]. From the AES analysis, the estimated film thickness is about 200 nm which corresponds well to the SEM cross-section observation. In this study, the film thickness can be controlled by the thickness of Ti precursor films, as it is the only Ti source.

5. Conclusions

$BaTiO_3$ films were synthesized on stainless steel substrates at $90^{o}C$ under atmospheric pressure. SEM and AFM analysis revealed that the films are composed of nanosized grains (~20nm) which may have a tetragonal crystal structure according to the XRD results. Higher concentration of $Ba(OH)_2$ solution and longer reaction times promote the formation of the films. Heat treatment of the films results in reduction of hydroxyl groups.

References

[1] Elliott B. Slamovich and Ilhan A. Aksay, Structure Evolution in Hydrothermally Processed (<$100^{o}C$) $BaTiO_3$ Films, *J. Am. Ceram. Soc.*, Vol 79 [1], 1996, p 239-247.

[2] Asiaie R., Zhu W. D., Akbar S. A. and Dutta P. K., Characterization of Submicron Particles of Tetragonal $BaTiO_3$, Chem. Mater., Vol 8 [1], 1996, p 226–234

[3] Mauricio E. Pilleux, Carlos R. Grahmann, and Victor M. Fuenzalida, Hydrothermal Strontium Titanate Films on Titanium: An XPS and AES Depth-Profiling Study *J. Am. Ceram. Soc*., Vol 77 [6], 1994, p 1601-1604

[4] Mark A. McCormick1 and Elliott B. Slamovich, Microstructure Development and Dielectric Properties of Hydrothermal $BaTiO_3$ Thin Films, *J. Eur. Ceram. Soc.,* Vol 23, 2003, p 2143-2152

[5] Sharma H. B. and Mansingh A., Phase Transition in Sol-gel Derived Barium Titanate Thin Films, *J. Phys. D-Appl. Phys.,* Vol 31(13), 1998, p 1527-1533

Figures:

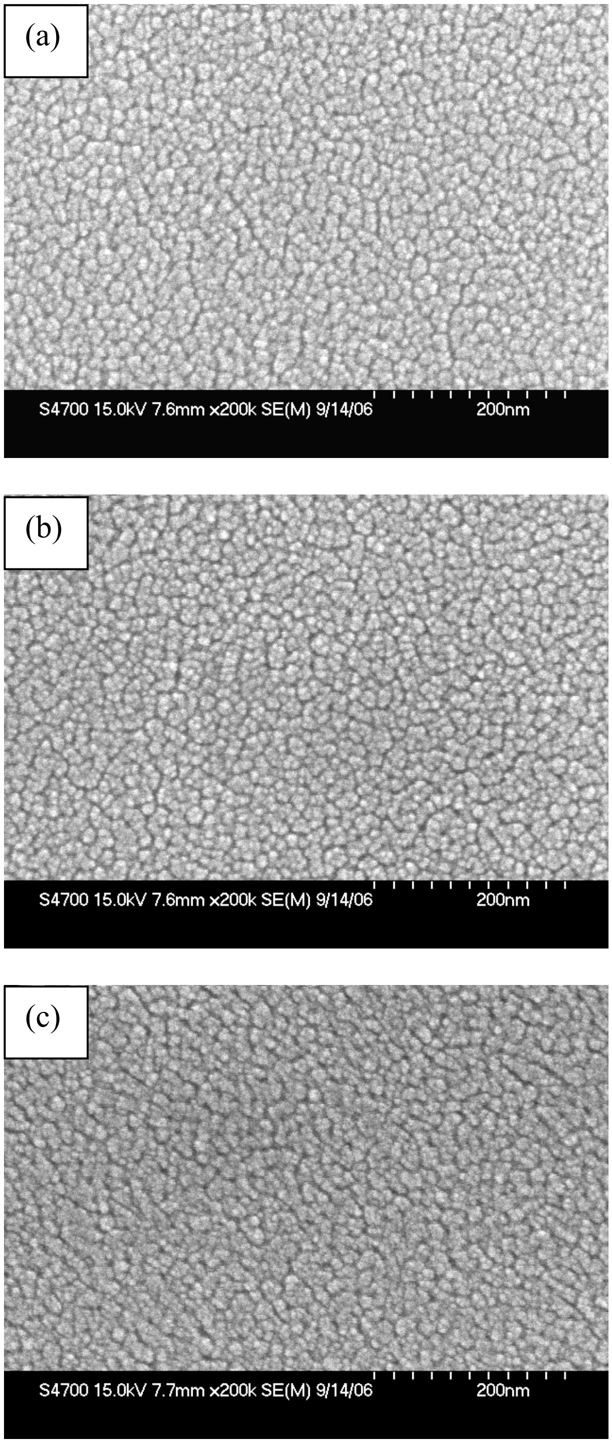

Fig.1. SEM micrographs of $BaTiO_3$ films synthesized in (a) 0.5M $Ba(OH)_2$; (b) 1.0M $Ba(OH)_2$; (c) 2.0M $Ba(OH)_2$ at 90°C for 6hrs

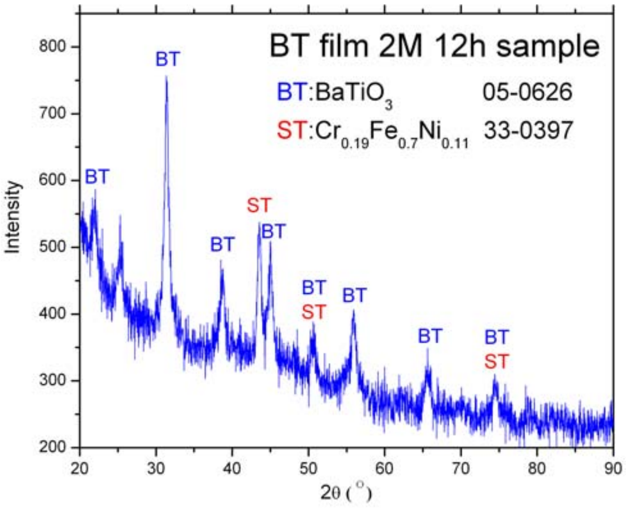

Fig.2. XRD pattern of $BaTiO_3$ films synthesized in 2.0M $Ba(OH)_2$ solution at 90°C for 12hrs.

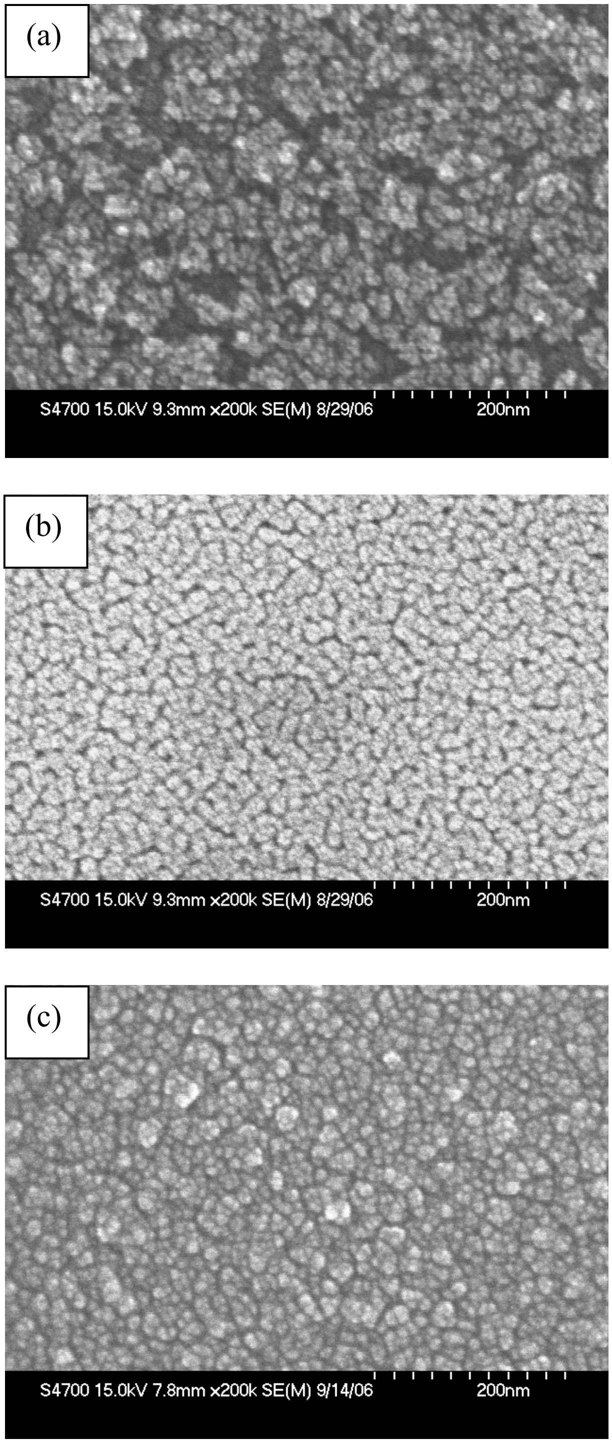

Fig.3. SEM micrographs of $BaTiO_3$ films synthesized by (a) 1.0M $Ba(OH)_2$ for 4hrs; (b) 1.0M $Ba(OH)_2$ for 12 hrs; (c) 2.0M $Ba(OH)_2$ for 12hrs.

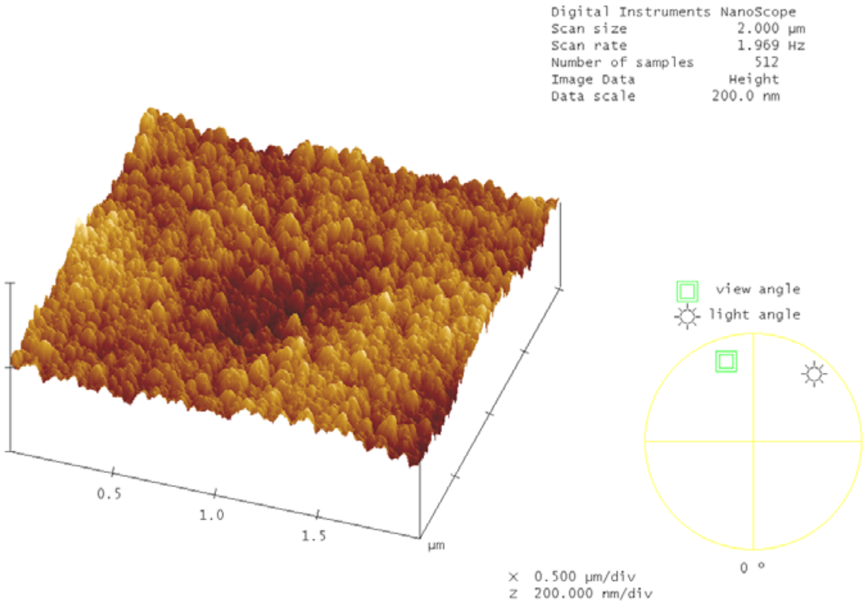

Fig.4. AFM image of $BaTiO_3$ films synthesized in 1.0M $Ba(OH)_2$ for 12hrs

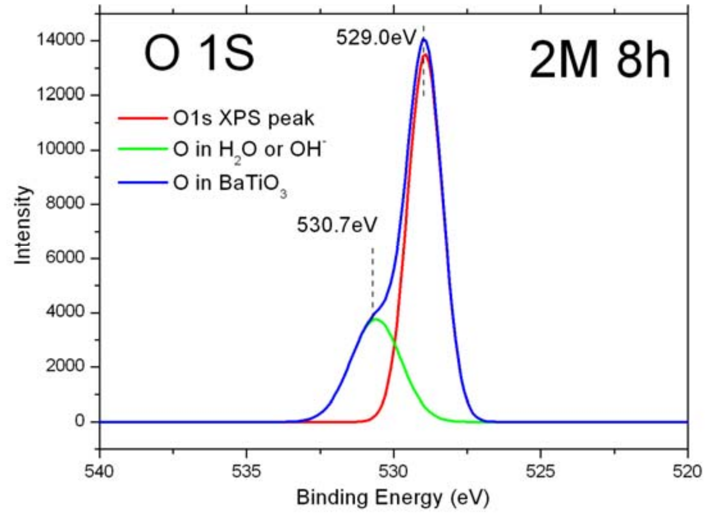

(a)

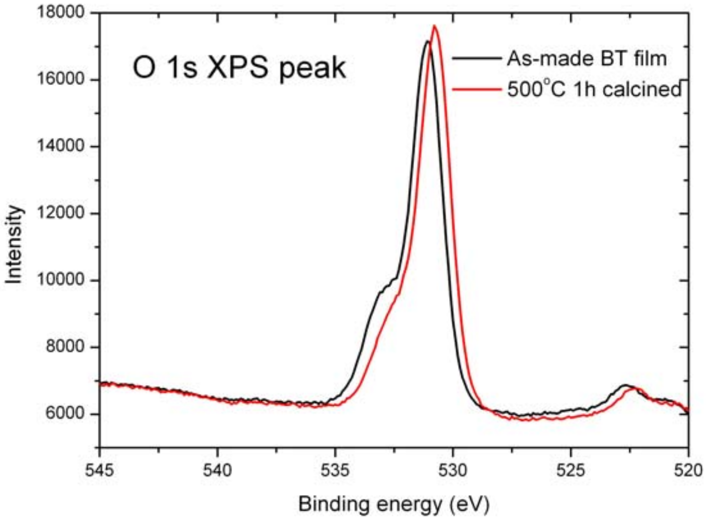

(b)

Fig. 5. XPS spectra of (a) O1 S peak in $BaTiO_3$ film treated in 2M $Ba(OH)_2$ solution for 8hrs; (b) O1 S peak in $BaTiO_3$ film treated in 2M $Ba(OH)_2$ solution for 8hr before and after heat treatment.

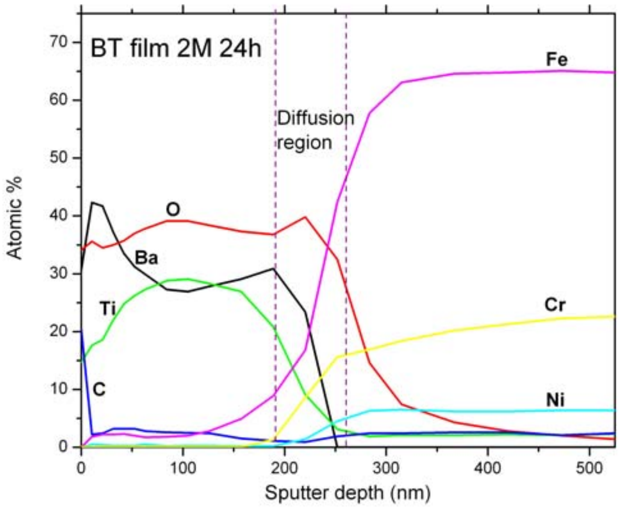

Fig. 6. AES depth profile of $BaTiO_3$ films treated in 2M $Ba(OH)_2$ solution for 24hrs

APPENDIX 3

SYNTHESIS AND SINTERING OF NANO STRUCTURED HIGH PURITY TITANIUM DIOXIDE CERAMICS

1. Sample Preparation

High purity nanosized TiO_2 powders were prepared by precipitation of Ti(IV)-isopropoxide followed by freeze-drying of the precipitates. 50ml Ti(IV)-isopropoxide ($Ti[OCH(CH_3)_2]_4$ 99.995%, Alfa-Aesar) was added into 1L deionized water under constant stirring. The precipitate was mixed with 1L of 2-Propanol (99.5% Alfa-Aesar) and ultrasonicated (SONICS, Vibra-Cell, Newtown, CT, USA) for 1 minute to deflocculate the hydroxides. Gel-like precipitates were freeze-dried (Genesis SQ Freeze Dryers, Winchester, Hampshire,UK) at -25^{o}C under vacuum for 72hrs. Fluffy precursor powders were calcined at various temperatures (400^{o}C, 500^{o}C, 600^{o}C and 700^{o}C) for 1h with a heating and cooling rate of 2^{o}C/min and 5^{o}C/min, respectively. The crystallinity and phase composition of the calcined powders were determined by X-ray diffraction (XRD, Philips X'Pert, Holland). The size and morphology of powder were observed by Scanning Electron Microscopy (SEM, Hitachi S-4700, Japan). Pellets were prepared by uniaxial pressing at 50MPa followed by iso-static pressing at 300MPa using powders calcined at 400^{o}C and 700^{o}C. Commercially available TiO_2 powders (99.9%, Sigma Aldrich) were also pressed into pellets following the same procedure. Sintering was performed at 900^{o}C, 950^{o}C and 1000^{o}C for 2hrs in oxygen atmosphere with a heating rate of 4^{o}C/min.

2. Phase Evolution of TiO_2 Powders

Hydrolysis of the Ti(IV)-isopropoxide resulted in formation of titanium hydroxide precipitates. XRD analysis (Fig. 1) reveals that there is no crystalline phase (absence of diffraction peaks) in as-prepared powders. Well-crystallized anatase TiO_2 were obtained by calcination at temperature as low as 400^{o}C. Further increase the calcination temperature leads to sharper diffraction peaks, indicating higher degree of crystallinity and larger crystallite size. At 700°C, a small amount (~9%) of rutile phase was identified. This anatase to rutile phase transition temperature is lower than commonly observed temperature around 915°C [1], which may be attributed to the difference in particle size of hydroxide precursors. The temperature of phase transformation was found to be lowered in nanosized powders [2]. The commercial powders were found to be a mix of anatase phase and rutile phase, with an average crystalline size close to that of the powders calcined at 700°C. The phase and the crystallite size of the powders determined by XRD are summarized in Table 1.

3. Sintering of the TiO_2 powders

The morphology of powders, observed by SEM, is shown in Figure 2. It is revealed that at calcination temperatures below 600°C, the average particle size of powders is similar, which is in good agreements with the XRD results. After calcination at 600°C, particles of the size ~20nm form a certain degree of agglomeration. It is apparent that partial sintering (neck formation) occurred between the particles for powders calcined at 700°C. It was noticed that the particle size and shape of powders are very uniform at all calcination temperatures. The powder morphology of the commercial powders looks similar to that of the powder calcined at 600°C, while some larger agglomerates appear to be present in commercial powders.

Selected samples (powders calcined at 400°C and 700°C as well as commercial powders) were sintered at 900°C, 950°C and 1000°C. The sintering of the samples was carried out in oxygen atmosphere to prevent the formation of oxygen vacancies which could significantly affect the dielectric properties of TiO_2. Figure 3 shows the relationship between relative density and sintering temperature of the samples. The firing density of TiO_2 prepared in this work is significantly higher than that of the samples prepared using commercial powders. After sintering at 1000°C, the density of the samples from precipitated powders is near 98%, whereas the density of the samples from commercial powder is about 92%. This may be attributed to the difference in the crystalline phase of these powders as 400°C calcined powders are pure anatase; powders calcined at 700°C have 91% of anatase phase, while commercial powders have only 49% anatase phase. It was found that the densification process of TiO_2 can be assisted by the anatase to rutile phase transition [3]. Therefore, powders with higher fraction of anatase phase sintered better at lower temperatures.

SEM images of the as-fired surfaces of the TiO_2 ceramics sintered at different temperatures are shown in Fig. 4-6. It was observed that as the sintering density gradually increases from 900°C to 1000°C, there is no significant grain growth within this temperature range. In addition, there is no obvious difference in grain size of the samples prepared from powders calcined at 400°C and 700°C. It should be mentioned that the radial shrinkage of the sample made of 400°C calcined powder is 8.5% larger than that of the sample prepared from 700°C calcined powders due to the differences in their green densities

4. Conclusions

High purity TiO_2 nanopowders were synthesized by precipitation method using Ti(IV)-isopropoxide as starting compound. Well-crystallized powders with a crystallite size of 10nm were obtained by calcination at temperatures as low as 400°C. The anatase to rutile phase transition temperature was lowered to about 700°C, due to very small particle size of powders. The sinterability of the powders with higher amount of anatase phase than rutile was improved in that the densification process may have been assisted by the anatase to rutile phase transition.

References

[1] Q. Shi, D. Yang, Z. Jiang and J. Li, Visible-light Photocatalytic Regeneration of NADH Using P-doped TiO_2 Nanoparticles, *J. Mol. Cata. B: Enzymatic* **43**, 44-48 (2006).

[2] B. O. Regan and M. Graetzel, A Low-Cost, High-Efficiency Solar Cell Based on Dye-Sensitized Colloidal TiO_2 Films, *Nature (London)*, **353,** 737-40 (1991).

[3] L. R. Skubal , N. K. Meshkov and M. C. Vogt, Detection and Identification of Gaseous Organics Using a TiO_2 Sensor. *J. Photochem. Photobiol. A: Chem.*, **148**, 103-108 (2002).

Figures

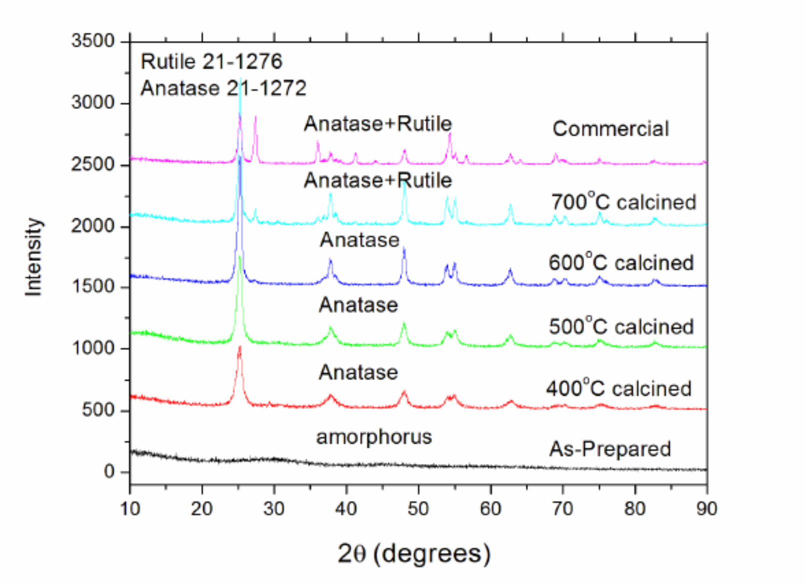

Figure 1. XRD pattern of the TiO_2 powders.

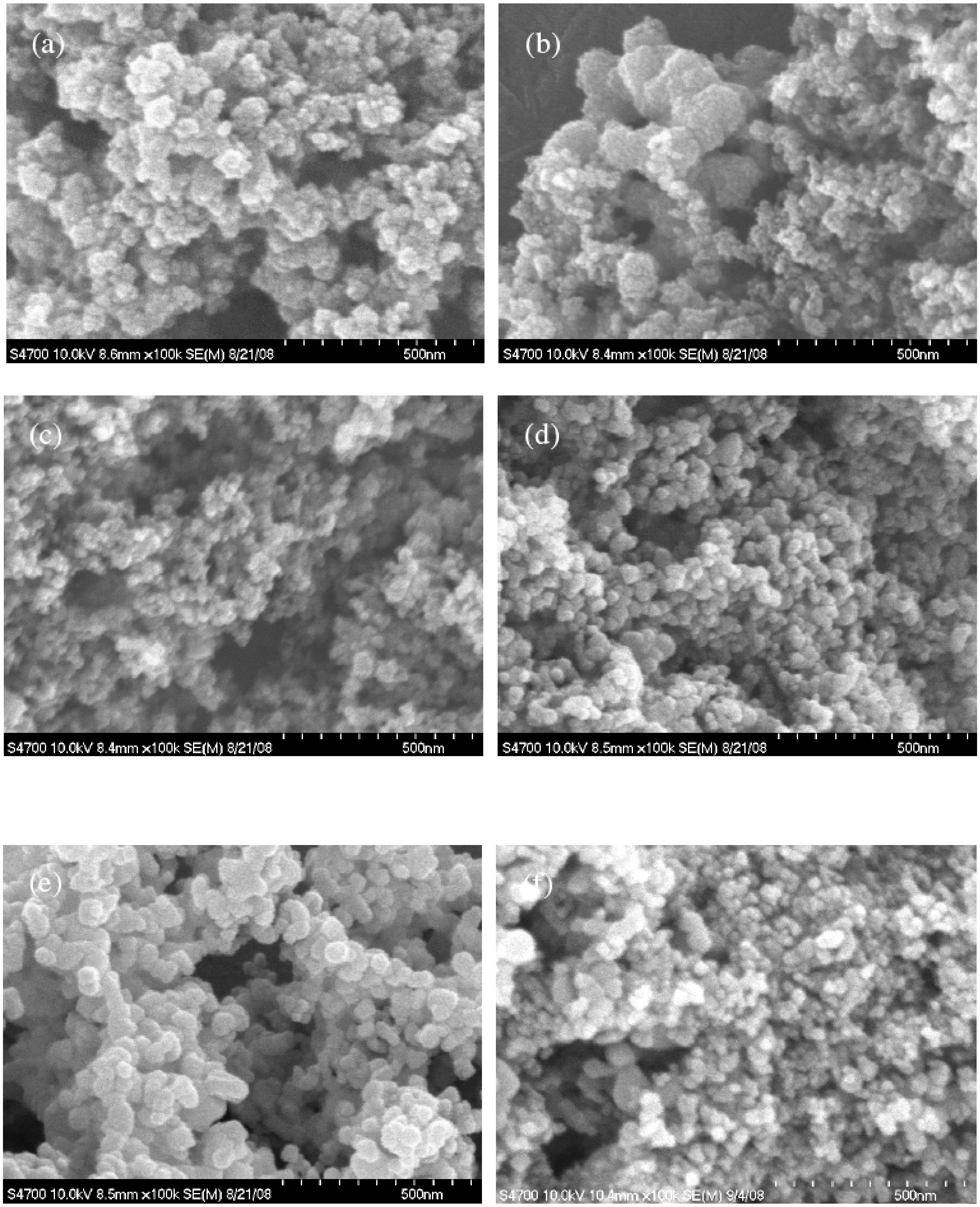

Figure 2. SEM images of the TiO_2 powders (a) as-dried; (b) calcined at 400°C; (c) calcined at 500°C; (d) calcined at 600°C; (e) calcined at 700°C; (f) commercial powder (bar scale:500nm).

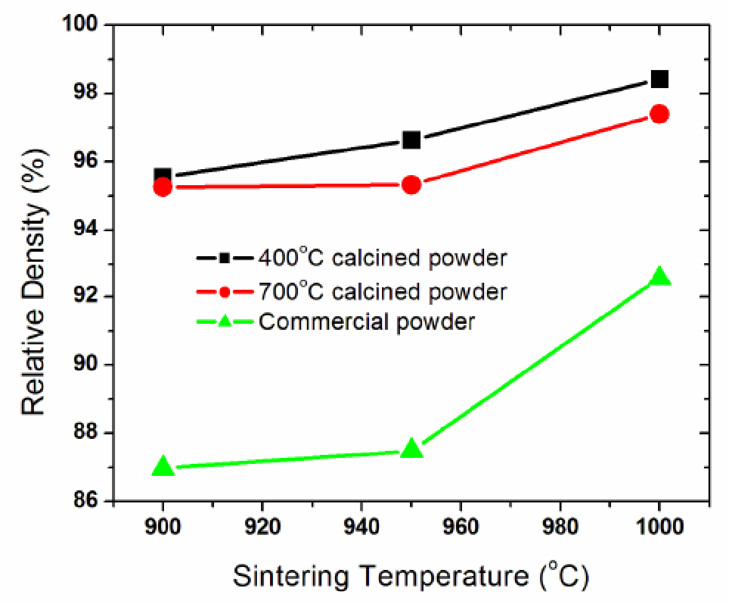

Figure 3. Relative density vs. sintering temperature of TiO_2 ceramics.

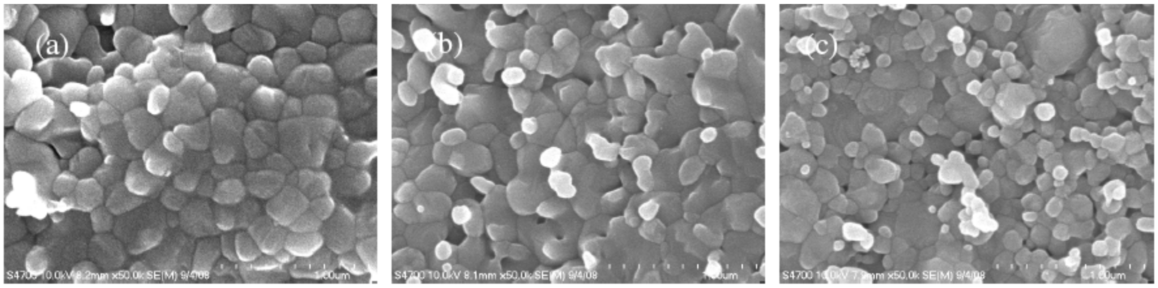

Figure 4. SEM images of the surfaces of TiO_2 ceramics sintered at 900°C for 2hrs (a) 400°C calcined powders; (b) 700°C calcined powders; (c) commercial powders (scale bar: 1μm).

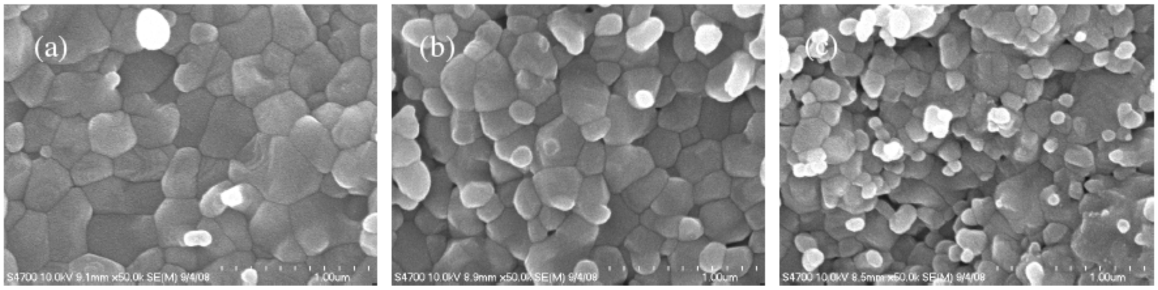

Figure 5. SEM images of the surfaces of TiO_2 ceramics sintered at 950^oC for 2hrs (a) 400^oC calcined powders; (b) 700^oC calcined powders; (c) commercial powders (scale bar: 1μm).

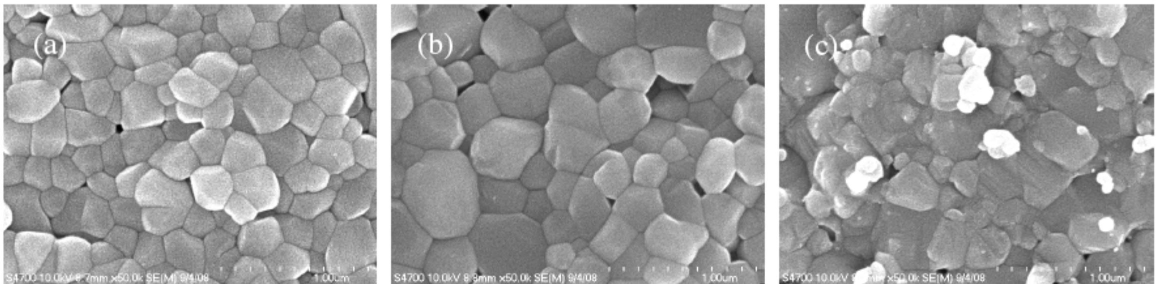

Figure 6. SEM images of the surfaces of TiO_2 ceramics sintered at 1000^oC for 2hrs (a) 400^oC calcined powders; (b) 700^oC calcined powders; (c) commercial powders (scale bar: 1μm).

Tables

Table 1. Crystalline phases and the crystallite size of TiO_2 powders determined by XRD

Calcination Temperature	Phase	Crystalline size (nm)
400^{o}C	Anatase	9.7±3
500^{o}C	Anatase	11.8±5
600^{o}C	Anatase	15.7±4
700^{o}C	Anatase:Rutile (91:9)	21.3±5
Commercial powders	Anatase:Rutile (49:51)	17.5±5 (A), 26.9±9 (R)

SECTION

3. FUTURE WORK

Based on the research discussed in the present work, further investigation in the following areas may lead to better understanding and improved energy storage capability of ceramic dielectrics.

1. High resolution transmission electron microscopy (HRTEM) study and chemical analysis of the microstructure of TiO_2 ceramics. Detailed observation and analysis of the defect structure and grain boundaries are of great importance to understand different dielectric response of TiO_2 ceramics processed under various conditions and with various impurities and/or dopants.
2. Study of linear dielectrics with high temperature stability and dielectrics with high dielectric constant. In the present study, dielectric properties of TiO_2 ceramics were investigated up to $200^{o}C$. However, due to greatly enhanced electrical conductivity, TiO_2 ceramics may not be suitable for applications at temperatures higher than $200^{o}C$. Other linear dielectrics such as $CaZrO_3$ may be suitable for high temperature applications. A systematic study of such linear dielectrics may lead t development of high energy density capacitors with excellent temperature stability and reliability in harsh environments. High energy density achieved in linear dielectrics is mainly depends on high electric fields applied. Due to catastrophic failure mode of ceramic dielectrics in practical applications, the operating field has to be very conservative, which would lead to much lower

energy densities than that of maximum achievable. For dielectrics with high dielectric constant, their energy density has lower dependence on electric field so that high energy density can be achieved at relatively lower electric field. Thus, energy storage capability of ferroelectrics, antiferroelectrics and relaxors is worth of further investigations.

3. Dielectric breakdown mechanism. Fundamental understanding of the mechanisms of dielectric breakdown is of great importance to improve breakdown strength of dielectrics. Most theoretical studies on dielectric breakdown phenomenon were conducted in the 1950's and 1960's, however, mechanisms of dielectric breakdown in ceramics is still not fully understood. The design of dielectric materials with much improved breakdown strength would rely on the fundamental understanding of the breakdown phenomenon.
4. Design of capacitor configurations: It is well known that dielectric breakdown normally occurs at the edge of dielectric/electrode material interface due to field enhancement. This problem severely limit the operating voltage of the capacitors, resulting in much lower energy density than the dielectric material itself may have. Since the intensity of field enhancement is related to the electrode material as well as the geometric configuration of the dielectric/electrode interface, improved energy density could be achieved through design of capacitors.

VITA

Sheng Chao was born on September 15, 1979 in Suzhou, Jiangsu Province, China. He received his pre-college education at Suzhou No. 16 middle school and Suzhou No. 10 high school. In September 1998, he started his undergraduate education in School of Materials Science and Engineering at Hefei University of Technology (Hefei, China). In 2002, he graduated with honor with B.S. degree. Sheng continued his graduate study in Hefei University of Technology and received his Master's degree in Materials Science in 2005.

Followed by his dream of studying abroad, Sheng started his Ph.D. study in 2005 under the supervision of Dr. Fatih Dogan at University of Missouri-Rolla (former name of Missouri University of Science and Technology). His doctoral work was focused on the development of ceramic dielectrics for high energy density capacitor application.